

Copyright

by

Brian Jeffrey Gereke

2018

The Dissertation Committee for Brian Jeffrey Gereke
Certifies that this is the approved version of the following dissertation:

Experience-dependent trends in hippocampal rhythms

APPROVED BY
SUPERVISING COMMITTEE:

Laura Lee Colgin, Supervisor

Boris Zemelman, Co-Supervisor

Michael Drew

Alex Huk

Daniel Johnston

Nicholas Priebe

Experience-dependent trends in hippocampal rhythms

by

Brian Jeffrey Gereke

Dissertation

Presented to the Faculty of the Graduate School of

The University of Texas at Austin

in Partial Fulfillment

of the Requirements

for the Degree of

Doctor of Philosophy

The University of Texas at Austin

August 2018

Acknowledgements

I begin by thanking my advisors: Dr. Laura Lee Colgin and Dr. Boris Zemelman. Their constant availability, unwavering support and encouragement was more than any mentee could ask for. Secondly, I thank the members of my committee: Drs. Michael Drew, Alex Huk, Daniel Johnston and Nicholas Priebe. Their feedback and willingness to sacrifice time on behalf has been a great asset. I would also like to thank my colleagues in the Colgin Lab and Zemelman Lab for all of their help and friendship throughout the years. Special acknowledgements should be given to Katelyn Bobbitt for dedicating painstaking effort into developing the microdrives used in all of the research presented in this dissertation, and to Alexandra Mably without whom Chapters 2 and 3 of this dissertation would not have been possible. I also want to acknowledge the staff of the Center for Learning and Memory and Institute for Neuroscience, particularly Krystal Phu, Chris Weatherly, Jason Goltz, Cindy Thompson, and Susan Cushman, for all they do to make the graduate program run so smoothly. Lastly, I thank my parents, family, and friends. They are the foundation for everything I do in my life.

Abstract

Experience-dependent trends in hippocampal rhythms

Brian Jeffrey Gereke, Ph.D.

The University of Texas at Austin, 2018

Supervisor: Laura Lee Colgin, Co-Supervisor: Boris Zemelman

The principal neurons of the hippocampus, “place cells”, are neurons with spatial receptive fields. In hippocampal subfield CA1, place cells have been shown to predict future locations. This anticipatory firing emerges with experience, across exposures to an environment, and is thought to be mediated by Hebbian plasticity in the CA3-CA1 network. Theta, slow gamma, and fast gamma rhythms are thought to route spatial information in the hippocampal formation and to coordinate place cell ensembles. Yet, it is unknown whether these rhythms exhibit experience-dependent changes that are concurrent with those observed in place cells. In this dissertation, I used extracellular tetrode recordings from mouse CA1 to show that experience-dependent changes in theta and slow gamma amplitude follow a similar time course as anticipatory place cell firing, with theta being elevated prior to, and slow gamma elevated alongside, the emergence of anticipatory anticipatory firing. I show that cross-frequency interactions between these rhythms, and their modulation by running speed, vary over time in similar experience-dependent ways. These results are in line with the view that theta rhythms promote acquisition of anticipatory firing, while slow gamma rhythms signal the growing efficacy

of CA3 input to CA1 with experience. Other recent work from our lab showed that coordination of CA1 place cells by theta and slow gamma rhythms was disrupted in a triple transgenic (3xTg) mouse model of Alzheimer's disease. As these mice typically display behavioral deficits in long term memory retrieval, I hypothesized that anticipatory place cell firing might be disrupted following long intervals (~24 hrs) between exposures to the environment. Experience-dependent trends in 3xTg place cell firing were at least as strong as those observed in control mice, and also were accompanied by trends in theta and slow gamma amplitude that were similar to controls. However, baseline theta amplitude, cross-frequency theta phase-gamma amplitude correlations, and theta amplitude-running speed correlations were abnormal in 3xTg mice. Abnormal hippocampal theta dynamics may, therefore, represent a biomarker for the early stages of Alzheimer's disease. To obtain these findings, I applied the generalized additive model to the analysis of local field potential data, which to my knowledge has not been done previously. I therefore provide a practical introduction to the framework and its application to time-frequency analysis of local field potential recordings, and discuss extensions to point process models, which are suggested to be an important area for future development.

Table of Contents

List of Tables	x
List of Figures	xi
Chapter 1: Introduction	1
1.1 - Hippocampus	2
1.1.1 Anatomy	4
1.1.2 Foundational work on hippocampal theta	10
1.1.3 Foundational work on hippocampal gamma	12
1.2 - Experience-dependent trends in place cells	17
1.3 - Experience-dependent trends in hippocampal rhythms	20
1.4 - Overview of dissertation	23
Chapter 2: Experience-dependent trends in CA1 theta and slow gamma rhythms in freely behaving mice	25
2.1 - Abstract	25
2.2 - Introduction	26
2.3 - Materials and methods	28
2.3.1 Subjects and testing procedures	28
2.3.2 Microdrive preparation, surgery, and tetrode placement	29
2.3.3 Histology	30
2.3.4 Data acquisition	30
2.3.5 Place cell analyses	31
2.3.6 Signal processing	33
2.3.7 Statistical analyses	34

2.3.8 Confidence intervals and test statistics	36
2.3.9 Cross-validation analyses	37
2.4 - Results	38
2.4.1 Theta and gamma power and phase-amplitude correlations increased with running speed	42
2.4.2 Experience-dependent changes in theta and slow gamma	47
2.4.3 Experience-dependent trends in the influence of running speed on theta and gamma rhythms	50
2.4.4 Experience-dependent trends in theta-gamma phase-amplitude correlations	54
2.4.5 Cross-validation	56
2.5 - Discussion	58
Chapter 3: Experience-dependent trends in 3xTg mouse CA1 theta and slow gamma rhythms	63
3.1 - Introduction	63
3.2 - Materials and methods	66
3.2.1 Subjects and testing procedures	66
3.2.2 Microdrive preparation, surgery, and tetrode placement	67
3.2.3 Histology	68
3.2.4 Data acquisition	68
3.2.5 Place cell analyses	69
3.2.6 Signal processing	69
3.2.8 Statistical analyses	70
3.3 - Results	71
3.3.1 3xTg mice show reduced place cell stability and modulation of spikes by theta and slow gamma phase	72

3.3.2 Experience-dependent trends in 3xTg place cells and rhythms	75
3.4 - Discussion	83
Chapter 4: Time-frequency analysis of brain rhythms using generalized additive models	87
4.1 - Introduction	87
4.2 - Time-frequency analysis	88
4.3 - The generalized additive model framework	99
4.4 - Application to brain rhythms	107
4.5 - Towards spectro-temporal point processes	119
4.6 - Discussion	127
Chapter 5: Conclusion	132
5.1 - Summary	132
5.2 - Discussion	134
5.3 - Final thoughts	139
References	140

List of Tables

Table 2.1: Statistical summary of <i>time-by-session</i> curves from Figure 2.1C	40
Table 2.2: Statistical summary of <i>time-by-session</i> difference curves from Figure 2.1D.....	41

List of Figures

Figure 1.1: Basic hippocampal anatomy	5
Figure 2.1: CA1 place field properties vary with experience.....	39
Figure 2.2: AR1 correction of residuals in base model	44
Figure 2.3: Dependence between running speed, theta/gamma amplitude, and theta phase-gamma amplitude correlations	45
Figure 2.4: Experience-dependent trends in theta and gamma power.....	49
Figure 2.5: Experience-dependent trends in the speed modulation of theta/gamma amplitude.....	51
Figure 2.6: Across-session differences in experience-dependent trends in the speed dependence of theta/gamma amplitude.....	52
Figure 2.7: Experience-dependent trends in theta phase-gamma amplitude correlations.....	55
Figure 2.8: Model comparisons.....	57
Figure 3.1: Place cell stability across sessions and laps	73
Figure 3.2: Place cell phase-locking to rhythms	74
Figure 3.3: 3xTg place cell firing varies with experience	76
Figure 3.4: Pre-registration of amplitude spectra	77
Figure 3.5: Theta amplitude is smaller in 3xTg mice.....	78
Figure 3.6: Dependence of theta and gamma amplitude on running speed and theta phase	80
Figure 3.7: 3xTg mice display weaker temporal trends in theta and slow gamma amplitude.....	82
Figure 4.1: Illustration of the continuous Morlet wavelet transform	94

Figure 4.2: Artifacts of the continuous Morlet wavelet transform.....	97
Figure 4.3: CMWT of mouse CA1 field potential	109
Figure 4.4: Comparison of response distributions and handling of autocorrelation	114
Figure 4.5: Functional anova cross-frequency phase-amplitude model.....	118
Figure 4.6: Wavelet transform modulus maxima lines	122
Figure 4.7: The conditional Tweedie GAM	125

Chapter 1: Introduction

Memory is at the core of who we are as human beings. It might be regarded as a kind of superpower that allows us to search through imperfectly stored copies of the past for answers about our future. Storing and accessing information about what, when, and where we experience things depends crucially on a system of brain regions called the hippocampal formation. Neuronal circuits in the hippocampus have been found to undergo a host of changes in response to experience. These include many forms of synaptic and intrinsic plasticity mechanisms. How these various types of experience-dependent plasticity combine to support well organized, cooperative dynamics between different brain regions remains poorly understood. In fact, the daunting nature of this problem might make one question the identifiability of such a combination.

The existence of mesoscopic patterns readily observed in the extracellularly recorded local field potential (LFP) provides a source of optimism. LFPs exhibit many types of organized rhythmic and arrhythmic patterns that are reliably observed over multiple spatio-temporal scales. Almost 150 years of exciting research has elucidated the many ways in which these patterns are related to perceptual, cognitive, and behavioral functions, as well as the implications these different patterns have with respect to neuronal circuit function. In the hippocampal formation, theta (~4-12 Hz) and gamma (~25-100 Hz) rhythms are the dominant patterns observed during active waking experience. The main goal of this dissertation will be to identify the ways in which these rhythms change during experience alongside concomitant effects observed at the level of single neurons in both healthy and diseased brains.

In working towards this goal, it is important to recognize that much has already been learned about hippocampal rhythms, and there are many variables which govern their dynamics. Thus, it has become evident that new phenomenological models are needed that can be fit directly to the types of data that are currently collected, and which capture the rich complexity that is identifiable from LFPs. A second goal of this dissertation will therefore be to discuss the generalized additive model framework, particularly its relevance and application to the study of brain rhythms. The steps I take toward addressing these goals in the following chapters are strongly grounded in foundations built by previous research. I therefore begin with a brief review of hippocampal research with a focus on the rodent anatomy, place cell, theta and gamma rhythm literatures.

1.1 – Hippocampus

The hippocampus has always been one of the most captivating areas of the brain for neuroscientists to study. From the beginning, anatomists were drawn to its “seahorse-like” appearance, choosing to name it after the aquatic creature. The first investigations of its microscopic structure by Ramón y Cajal resulted in drawings that might now be considered popular art. It was in the mid-20th century however, that the hippocampus became what some have subsequently called the “neural Rosetta Stone” (Andersen 2007).

There were at least three major discoveries. The first came from studies in human patients with medial temporal lobe damage (Scoville and Milner 1957; Milner et al. 1968). The most famous of these was an epilepsy patient named H.M. who received bilateral removal of the major parts of his medial temporal lobes including most of the hippocampus, entorhinal cortex and amygdala, and was studied longitudinally for 50 years (Corkin et al. 1997). The procedure resulted in severe but specific memory deficits. While he could remember information presented at short delays, or learn new implicit

motor skills, he was unable to store and recall long term memories of events, facts, or experiences. This enabled the clear distinction of many types of memories and demonstrated the close ties the hippocampal formation has to episodic memory.

The second major discovery came in 1966 with the demonstration of long-term potentiation (LTP) (Bliss and Lømo 1973; Lømo 2003). Prior to this discovery, the concept of synaptic plasticity as a mechanism for learning and memory had already been proposed (Cajal 1894; Hebb 1949). However, demonstrated forms of plasticity were either too short-lasting or required unrealistically long patterns of stimulation to serve as viable candidates for long term memory. LTP was the first demonstration of a long-lasting activity-dependent change in synaptic strength, and provided support for the theory of Hebbian learning (Hebb 1949).

Around this same time, extracellular recordings of single hippocampal neurons in awake behaving animals became practical. The earliest such recordings found habituating responses to a large variety of temporally repeated sensory stimuli, suggesting a role for the hippocampus in multimodal novelty detection (Vinogradova 2001). Motivated by behavioral work on spatial learning deficits in rats with hippocampal lesions (Douglas, 1967; Kimble, 1968), as well as work demonstrating a link between hippocampal theta rhythms and volitional motor behavior (Vanderwolf 1969), O'Keefe and Dostrovsky then recorded from rats moving freely in a spatial environment. This led to the third major discovery: place cells (O'Keefe and Dostrovsky 1971). These are cells with spatial receptive fields corresponding to an animal's location in its environment. In this initial report, the authors sketched out a theory that the hippocampus acts as a spatial reference map for the brain. They discussed how, when combined with a signal conveying the intention to move in a certain direction, such a map could be used to make predictions and anticipate future sensory experience. This theory, which was expanded in follow-up

studies and a book (O’Keefe 1976; O’Keefe and Nadel 1978), provided a basis for decades of future study.

Clearly there were many more than “three main discoveries”, and this presents a rather limiting view of hippocampal research. However, evidence for the hippocampus’ role in human episodic memory, combined with a plausible mechanism for long-term memory at the level of synapses and a theory of cognitive function motivated by a specialized cell type, has been a great driving force in attracting new scientists and advancing our knowledge of the hippocampus. Since these discoveries, the hippocampus has continued to be studied at every level of detail and from every conceivable angle. In the remainder of this chapter, I will introduce a rather small subset of the results with a focus on the basic rodent hippocampal anatomy, theta, gamma, and place cell literatures. A reasonable representation of any of these subsets is beyond the scope of this chapter; so where appropriate, I direct readers to relevant reviews on each of the topics.

1.1.1 – Anatomy

The hippocampal formation consists of the hippocampus proper (HP), dentate gyrus (DG), subiculum (Sub), presubiculum (PrS), parasubiculum (PaS), and entorhinal cortex (EC). Each of these areas can be further divided into subareas, each of which consist of a number of layers and sublayers. The connections within and between the areas are both subarea, layer, and cell type specific. I will focus on HP, DG, and EC with special attention allocated to subarea CA1 of dorsal HP as it is the most relevant area for this dissertation. Most of what is known about these circuits has been learned from rats; however, some mouse-specific details will be included where appropriate. A more comprehensive overview, and standard reference for this material, is provided by (Cappaert et al. 2015).

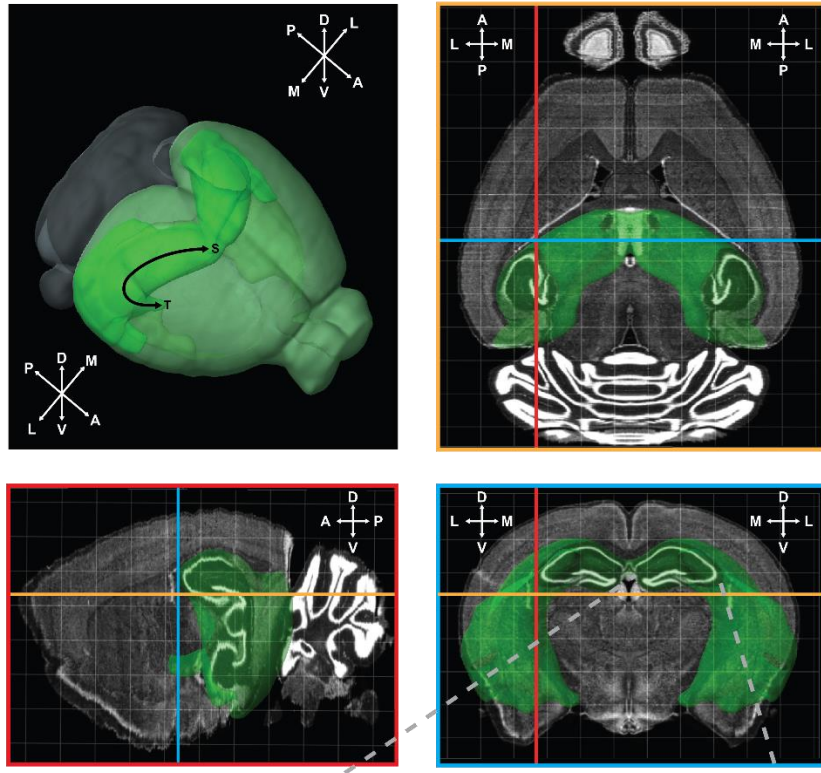
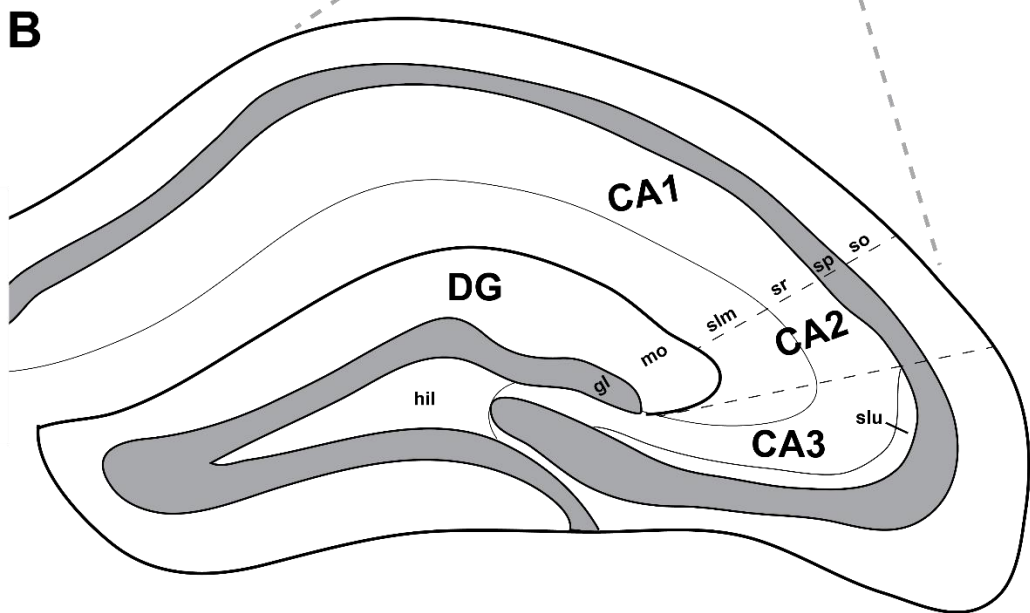
A**B**

Figure 1.1. Basic hippocampal anatomy. **A)** 3D and orthographic views of the mouse hippocampal formation. The top left panel shows a 3D representation of the mouse brain with cerebellar cortex in gray, cerebral cortex in light green, and the hippocampal formation highlighted in bright green. The black arrows denote the septo-temporal axis of the right hippocampus. The top right panel shows a top-down view of a horizontal section with the hippocampal formation highlighted in green. Note, the highlighted area should be interpreted as extending out from the plane into the third dimension. The bottom left/right panels show equivalent views for sagittal/coronal sections, respectively. In all panels, orange/red/blue lines denote the horizontal/sagittal/coronal sections, respectively, displayed in the other panels. Axis abbreviations: septal (S), temporal (T), dorsal (D), ventral (V), lateral (L), medial (M), anterior (A), posterior (P). **B)** Zoomed in illustration of a transverse section of the dorsal hippocampus. Subarea abbreviations: dentate gyrus (DG), Cornu Ammonis 1-3 (CA1-3). Sublayer abbreviations: hilus (hil), granule layer (gl), molecular layer (ml), stratum lacunosum-moleculare (slm), stratum radiatum (sr), stratum lucidum (slu), stratum pyramidale (sp), stratum oriens (so). All images were created and/or modified from open access resources made available by the Allen Institute for Brain Science:

- © 2015 Allen Institute for Brain Science. Brain Explorer 2. Available from: <http://mouse.brain-map.org/static/brainexplorer>
- © 2015 Allen Institute for Brain Science. Allen Brain Atlas API. Available from: brain-map.org/api/index.html
- © 2004 Allen Institute for Brain Science. Allen Mouse Brain Atlas. Available from: <http://connectivity.brain-map.org>

EC occupies the most posterior and ventro-lateral portions of the brain and is typically distinguished by its lateral (LEC) and medial (MEC) areas. The hippocampus, consisting of both HP and DG, is located anterior to EC and has a banana-like shape (Figure 1.1A). The bottom of the banana is ventral, the top dorsal, and the interior is oriented in the posterolateral-to-anteromedial direction. The long axis of the hippocampus is often interchangeably referred to as the dorsoventral or septotemporal axis. A slice orthogonal to this axis is the transverse axis. In the transverse axis, HP and DG look like two interlocking U shapes. HP is further divided into subareas CA3, CA2, and CA1. The medial portion of CA3 occupies the interior part of the DG “U”, and the distance away from DG in the CA3-to-CA1 direction is called the proximodistal axis. The half of DG closest to CA1 is called the enclosed blade, while the other half is known as the free blade.

Each of these areas is made up of a number of layers. LEC and MEC both have six layers numbered in the superficial-to-deep direction. DG has three layers (Figure 1.1B). Moving from the outer-to-inner part of the U, the first layer is mostly dendritic and called the molecular layer. The second is a cell layer called the granule layer. The third and interior-most layer called the hilus. Like cortex, the layers of HP are referenced with respect to their deep-vs-superficial position. Since HP is a continuous folding in of the cortex, it should be made clear that “deep” in HP corresponds to the outer part of the U in the transverse axis. Thus, in the superficial-to-deep direction, CA3 has five sublayers: stratum lacunosum-moleculare, stratum radiatum, stratum lucidum, stratum pyramidale, and stratum oriens (Figure 1.1B). CA2 and CA1 are both similar, with stratum lucidum notably absent.

EC receives input from a large number of cortical and subcortical areas, and represents one of the main sources of cortical input to the hippocampus. The superficial

layers of EC project to all areas of the hippocampus with layer II projecting to DG, CA3, and CA2, and layer III projecting to CA1. These projections arrive via a number of pathways, the primary of which is called the perforant path because it passes through PaS/Prs and punctures (i.e., perforates) through the posterior hippocampus. The LEC layer II component terminates in the outer third of the DG molecular layer and superficial s. lacunosum-moleculare of CA3/2. Conversely, the MEC layer II component terminates in the middle third of the DG molecular layer and deep s. lacunosum-moleculare of CA3/2. For CA1, MEC/LEC layer III projections terminate in s. lacunosum-moleculare of proximal/distal CA1, respectively. These projections appear to be primarily excitatory synapses onto excitatory cells (e.g., DG granule and CA pyramidal cells), although a smaller fraction does either terminate onto local inhibitory interneurons (Kiss et al. 1996; Melzer et al. 2012) or originates from long-range projecting inhibitory interneurons (Melzer et al. 2012).

Within HP, CA3 receives a projection from DG called the mossy fiber pathway that terminates in s. lucidum. These synapses are typically large and excitatory onto pyramidal cells. It also receives a strong recurrent projection from itself that terminates in either s. radiatum or s. oriens depending on the proximodistal location within CA3 of the soma of the originating cells. A significant number of cells in proximal CA3 project back to DG, but its largest projection, called the Schaffer collateral/commissural pathway, terminates in s. oriens and s. radiatum of CA1. Most of the CA3 inputs to CA1 s. oriens/s. radiatum come from the contra/ipsilateral CA3 respectively. A smaller portion of the projection arrives in CA2, which also sends back projections to DG and CA3, and forward projections to CA1 s. oriens/s. radiatum as well as to EC layer II.

CA1 is considered the primary output area of HP. Its axons exit via a large tract deep from s. oriens called the alveus. A portion of this projection is inhibitory feedback

to CA3 and DG, but the largest outputs are both excitatory and inhibitory projections to Sub and EC layer V. One of the important aspects of the latter projection is that proximal/distal CA1 projects more to MEC/LEC respectively, thereby reciprocating the EC-to-CA1 projection. It is also connected to a large number of other cortical and subcortical areas.

A set of the subcortical connections to hippocampus that deserves special mention are those involving the septal nuclei due to their involvement in theta rhythm generation. The medial septum and diagonal band of Broca (MS-DBB) send GABAergic, cholinergic, and glutamatergic projections to all areas of the hippocampus. These projections are most dense in DG and tend to target interneurons in all of the hippocampal areas. In the return direction, CA3 projects to the lateral septum, while CA1 projects to both the lateral septum and MS-DBB. Each of these projections contains a long-range GABAergic component.

1.1.2 – Foundational work on hippocampal theta

The earliest electrical recordings from live animal brains can be traced back to Richard Caton (Finger 2001). In a series of studies (1874-1891), he recorded from the surface of rabbit, monkey, and dog cortices. He demonstrated that animal brains clearly generate spontaneous electrical currents, and that these currents varied with recording location, behavior, and external stimuli like head movement or shining light into the eyes. His results were consistent with, and provided supplementary evidence for, previous functional localization studies of David Ferrier and others who used electrical stimulation methods. Despite its importance, Caton's work fell into relative obscurity until it was cited many years later by Hans Berger who is famous for developing a technique he called the “brain mirror” or electroencephalogram (EEG) (Berger 1929). Among Berger's most important observations were a ~10 Hz oscillation that he called the alpha wave and

a smaller ~30 Hz oscillation that he called the beta wave. He suggested the larger alpha wave was the carrier of mental energy, while the faster beta wave likely corresponded to metabolic activity in the cortex. Nowadays, brain rhythms (<100 Hz) measured in the extracellular field are thought to reflect the summation of temporally and spatially aligned transmembrane currents that are generated by synapses, as well as other slow active currents such as calcium spikes, voltage-gated resonance currents, and afterhyperpolarizations (Buzsáki et al. 2012).

The ~4-12 Hz theta rhythm, which has been called the “alpha wave” of the hippocampus, was first reported in rabbits not long after Berger’s seminal work on human EEG (Jung and Kornmüller 1938). Its study became more popular after 1954 when Green and Arduini, recording spontaneous theta in rabbits, cats, and monkeys, demonstrated that it could be blocked by lesioning the septal projection to the hippocampus (Green and Arduini 1954). During this time, theta was viewed as a singular uniform property of the hippocampus, and some hypotheses regarding its behavioral correlates included arousal (Green and Arduini 1954), conditioned and orienting reflexes (Grastyán et al. 1959), as well as general types of motivation and approach behaviors (Grastyán et al. 1966). The first study to quantifiably compare the presence of theta with recorded behavior identified voluntary locomotor activity as the primary correlate in rats, and it was suggested that this correlation might explain some of the previous results (Vanderwolf 1969). Theta amplitude and frequency were subsequently shown to correlate with animals’ overall running speed (McFarland et al. 1975).

Disagreements about theta’s behavioral correlates, particularly regarding its presence during immobility, were fueled by apparent species differences (Winson 1972), and it eventually became clear that multiple types of theta might coexist within the hippocampus. Theta pacemaker cells had been discovered in the medial septum and a

MS-DBB pacemaker theory for hippocampal theta generation was proposed (Petsche et al. 1962). Two types of theta were then distinguished pharmacologically (Kramis et al. 1975). The first was higher in frequency (~7-12 Hz), resistant to the cholinergic antagonist atropine, and related to movement. The second was lower in frequency (~4-12 Hz), blocked by atropine, and occurred during immobility. The atropine-resistant theta was subsequently shown to depend on the integrity of the EC (Buzsáki et al. 1983).

Others demonstrated theta's contribution to behavioral performance on a variety of memory tasks, as well as indirect connections to synaptic plasticity. For example, manipulations that eliminate theta, such as lesioning or inactivation of the medial septum, were shown to produce deficits in spatial memory (Winson 1978; Mitchell et al. 1982; Chrobak et al. 1989; Mizumori et al. 1990). Theta-timed stimulation was found to effectively induce LTP (Larson et al. 1986; Staubli and Lynch 1987; Greenstein et al. 1988), and the strength of LTP was shown to depend on the theta phase of stimulation in DG (Pavlides et al. 1988). Evidence highlighting the importance of the relative timing between inputs within a theta period then began to accumulate (Levy and Steward 1983; Larson and Lynch 1989; Stanton and Sejnowski 1989). Although place cells were known to fire at specific phases of the theta cycle (Buzsáki et al. 1983), it was unclear whether sequential inputs at the sub-theta time scale were relevant in the behaving animal. The relevance of the sub-theta time scale became more clear with the discovery of theta phase precession, an effect whereby individual place cells fire at progressively earlier phases of the theta cycle as an animal moves through the cells' place fields (O'Keefe and Recce 1993). Thus, the theta phase at which a cell spikes is predictive of the animal's location within the cell's place field. By consequence, proper coordination of phase precession between cells ensures that place cells fire in the same sequence within a theta cycle as their place fields are ordered in physical space. This could provide a mechanism by

which associations between locations are learned by taking advantage of the relative timing between place cells on a sub-theta timescale.

All of this foundational work on theta has continued to guide modern efforts to understand the mechanisms for different types of theta, their correlations with mobile behaviors, and their relevance for learning and memory. It is now understood that theta generation is modulated by a large number of brain regions and many types of interneurons, as well as neurotransmitters, receptors, and active channels that endow circuits of neurons with resonant properties at theta frequencies. A number of excellent reviews on these topics are available (Vertes and Kocsis 1997; Buzsáki 2002; Vertes et al. 2004; Colgin 2013; Korotkova et al. 2018).

1.1.3 – Foundational work on hippocampal gamma

In the same way that theta was called the “alpha of the hippocampus”, gamma (~25-100 Hz) has been called the “beta of the hippocampus”. Compared to theta, however, the study of gamma in the hippocampus began much later. Among the reasons for this was the lower amplitude of gamma, its mixing with nonlocal noise sources, and frequency limitations of the older recording systems appear most prominent (Bressler and Freeman 1980). Buzsaki et al. 1983 provided one of the earliest characterizations of rat hippocampal gamma and they reported a number of important findings (Buzsáki et al. 1983). Gamma was observed in all behavioral states, with higher amplitude during mobility. Amplitude was also largest around the DG cell/hilar layers and DG hilar gamma was coherent across hemispheres, implying long-range synchrony. Interneurons were phase-locked to both theta and gamma, and gamma amplitude was largest close to the interneuron-preferred phase of theta. Furthermore, the amplitude distributions were similar in animals with septal lesions, suggesting different mechanisms for the generation

of theta and gamma rhythms. From these observations it was concluded that gamma was generated by interneurons targeting principal cell soma.

Even after this landmark work, study of hippocampal gamma *in vivo* remained relatively sparse up through the mid 1990s. The importance of local inhibition was expounded upon by intracellular recordings of CA1/3 pyramidal cells in anaesthetized rats (Soltesz and Deschenes 1993). These experiments demonstrated that theta-modulated gamma amplitude could be controlled by varying intracellular chloride concentration and highlighted the role of fast GABA_A-mediated currents in locally generating these rhythms.

The importance of extra-hippocampal inputs for gamma generation was then studied using extracellular recordings in EC-lesioned anaesthetized rats (Bragin et al. 1995). Prior to lesioning, gamma amplitude in these animals was largest in the DG hilus and gamma frequency peaked at ~90 Hz. After lesioning, the peak gamma frequency dropped to ~40 Hz, and gamma amplitude was largest in CA1 s. radiatum. Since CA1 s. radiatum receives the majority of its input from CA3, it was hypothesized that CA3 acted as a separate gamma generator internal to the hippocampus, with EC driving DG gamma. This hypothesis was later supported by 96-site recordings of DG/CA3/CA1 in awake mobile rats, which demonstrated higher CA1-CA3 vs CA1-DG gamma coherence (Csicsvari et al. 2003). However, this study reported that the CA1-CA3 and DG gamma generators exhibited the same frequencies. Supplemented by single unit spike-field and spike-spike cross-correlation analyses between the areas, a model was proposed in which CA1 gamma is driven mostly by a combination of feedforward inhibition and excitation from CA3. However, it was recognized that, due to a growing body of theoretical and *in vitro* results, a large number of mechanisms are likely

involved. I refer readers to reviews on these parts of the literature (Mann and Paulsen 2005; Cutsuridis et al. 2010; Buzsáki and Wang 2012).

As with theta, it became clear that multiple gamma generators likely exist even within the subareas of the hippocampus. This could be motivated by the results discussed above, as well as anatomical arguments based on the layered specificity of the projections to each of the regions. Consequently, it was demonstrated via simultaneous tetrode recordings in CA1, CA3 and MEC that two subtypes of gamma exist in CA1: a slower ~25-50 Hz CA3-CA1 coherent gamma, and a faster ~55-100 Hz MEC-CA1 gamma (Colgin et al. 2009). Subsequent work then demonstrated that these slow/fast gammas were largest in CA1 s. radiatum/s. lacunosum-moleculare, respectively, in correspondence with expectations from the anatomy (Belluscio et al. 2012; Schomburg et al. 2014).

While much effort has been directed toward understanding the mechanisms of gamma rhythm generation, there was a long period in which no behavioral correlates had been identified, and its function remains largely unresolved to this day. The first studies to quantify the relationship between hippocampal gamma and running speed in rats found a positive correlation between gamma frequency and running speed (Ahmed and Mehta 2012; Kemere et al. 2013; Zheng et al. 2015). However, it is worth pointing out that every result discussed up to this point was demonstrated in the rat. The first characterization of hippocampal gamma in the behaving mouse (Buzsáki et al. 2003) came much later than reports in rats. Mouse hippocampal gamma was found to be similar to that observed in rats. Its amplitude was theta-modulated, largest in DG hilus, and coherent across hemispheres. Compared to rats, however, it was noted that gamma in mice is larger in relation to the theta cycle, and it was suggested that this may be due to the higher density of neurons in the smaller mouse brain. Mouse CA1 gamma also has a

different relationship with running speed, with the amplitudes of both slow and fast gammas subtypes increasing monotonically with running speed (Chen et al. 2011). Whatever the explanation, these recent characterizations, along with the apparent existence of species differences, appear reminiscent of the work on hippocampal theta from the 1970s.

The paucity of behavioral correlations for hippocampal gamma stands in contrast to sensorimotor areas of the brain where gamma rhythms could be easily induced by experimenter-controlled stimuli. Thus, early conceptual models of gamma function in the hippocampus derived mainly from work in these areas. Probably the most influential models have been those based around the ideas of synchronization and temporal binding of cell assemblies (Von Der Malsburg 1985; Singer 1993). In these hypotheses, a cell assembly is defined as a distributed set of cells that co-activate at millisecond precision. The cells making up an assembly may have different response properties with respect to the dimensions of a set of stimuli, or other potentially unobserved variables. According to the hypothesis, cells are identified as belonging to the same instantaneous computational unit according to their synchronous activation and integration onto a common target. In this scenario, gamma oscillations are regarded as a specific implementation of temporal synchrony in which distinct cell assemblies are segregated into separate cycles. Thus, the role of gamma oscillations is to bring about the patterns of inhibition and excitation necessary to enforce the temporal synchrony and segregation of cell assemblies.

Furthermore, because synchronous neurons are hypothesized to better drive their targets, and band-limited oscillations imply predictability between the timing of cell assemblies, an additional function of gamma would be to promote activity-dependent plasticity. An important aspect of this hypothesis is that the unique combination of cells making up an assembly must be functionally determined (i.e., by stimuli, behavior,

cognitive function, etc.). This implies that gamma should not be trivially driven by a spatiotemporally stationary pacemaker. Rather, it should be dynamic and develop in a use-dependent fashion. The plasticity mechanisms relevant to gamma in the hippocampus have been studied *in vitro*, and some of these have been reviewed (Traub et al. 1998).

A hippocampus-specific proposal built off the early temporal synchrony hypotheses by suggesting that theta-nested gamma cycles correspond to single items in a multi-item short term memory (Lisman and Idiart 1995). During spatial navigation, for example, there could be an assembly for each place in the environment. The frequency of gamma would then determine the number of discrete places represented by a sequence of place cell assemblies during a theta cycle. It would also determine the amount of time the network is inhibited between cell assemblies. Based on this consideration, it was proposed that the time constant needed for excitatory transmission between assemblies should be longer than a gamma cycle and might possibly be mediated by slow NMDA channels (Jensen and Lisman 1996a, 1996b). In contrast, fast AMPA-mediated transmission should occur within an assembly before the onset of inhibition at the end of the gamma cycle. Thus, in this framework, the frequency of gamma is viewed in relation to constraints on the mechanisms that support communication both within and between cell assemblies.

While the temporal synchrony-based hypotheses have been influential in the study of hippocampal gamma rhythms, it should also be pointed out that they are far from universally accepted. In particular, it is not commonly agreed that the brain is organized to properly recognize and treat synchronous spikes as belonging to the same computational unit. Even if we assume cell assemblies are meaningful, it is not completely clear what computational elements they represent in the context of a given algorithm. Thus, the relevance of such a code to the perceptual binding problem, where

neuronal synchrony has been proposed to bind information across different perceptual modalities into what the brain judges to be a single perceptual object, is even more controversial. Detailed critiques of these ideas have been put forth (Shadlen and Movshon 1999).

1.2 – Experience-dependent trends in place cells

Anticipation of future experience based on prior experience requires the successful encoding, retrieval, and utilization of memory. One of the major goals of hippocampal research has therefore been to identify different types of anticipatory activity and to study how these types of activity are acquired. Much of the evidence for anticipatory activity in the hippocampus has been identified by studying place cells, and the acquisition of such anticipatory activity is typically thought to depend on Hebbian-like synaptic plasticity mechanisms. Although these mechanisms are thought to be promoted by theta and gamma rhythms, the relationship of theta and gamma to anticipatory place cell activity remains unclear. Having presented some of the foundational work on theta and gamma, I now discuss the evidence for anticipatory place cell activity and its acquisition.

Early evidence for anticipatory coding in place cells came from analyses demonstrating that place fields are more spatially localized on average when spikes are mapped to locations 100-200ms ahead of the animal (Muller and Kubie 1989). Similarly, during bi-directional exploration of a cue-rich circular track, place cells tend to fire more during cue approach (Battaglia et al. 2004). Theta phase precession has also been viewed as an anticipatory effect, because cells firing at late theta phases effectively predict the

animal's upcoming locations on future theta cycles (Jensen and Lisman 1996a; Skaggs et al. 1996; Tsodyks et al. 1996). More recent evidence for anticipatory place cell coding has stressed its importance in decision-making. On spatial mazes with choice points, sequences of place cells representing locations ahead of the animal fire preferentially at the choice points (Johnson and Redish 2007). Place cell sequences have subsequently been shown to predict the path an animal will take to reach a goal (Pfeiffer and Foster 2013; Wikenheiser and Redish 2015).

Modeling work suggests anticipatory place cell sequences could result from a cued chaining mechanism whereby a cued cell initiates a sequence from a learned set of asymmetric weights (Blum and Abbott 1996; Jensen and Lisman 1996a; Tsodyks et al. 1996). Within a theta cycle, for example, cells firing at earlier theta phases could activate cells at later theta phases and thereby selectively strengthen connections in the early-to-late direction. A common prediction of these models was that place fields should shift backward across repeated exposures to a spatial trajectory as the asymmetric connections between the cells in the sequence strengthen. Evidence in favor of this prediction has now been demonstrated many times by separate laboratories in both rats (Mehta et al. 1997, 2000; Lee et al. 2004; Roth et al. 2012; Feng et al. 2015) and mice (Cabral et al. 2014a; Gereke et al. 2018). The backward shifting of place fields has also been shown to disappear with age (Shen et al. 1997) and to depend on the proper functioning of NMDA receptors (Ekstrom et al. 2001; Cabral et al. 2014a).

Other types of experience-dependent trends in place cell activity have also been reported. One such trend is a reduction in the amount of spike amplitude attenuation with

exposure to a familiar environment (Quirk et al. 2001). Hippocampal pyramidal cells display an activity-dependent attenuation of spike amplitude within a burst which can be recorded extracellularly (Ranck 1973; Quirk and Wilson 1999), and is a signature of effective spike backpropagation (Buzsaki et al. 1996). Because spike backpropagation can promote LTP (Magee and Johnston 1997), the experience-dependent reduction in spike amplitude attenuation may serve as a marker for plasticity. Spike amplitude attenuation is also reduced in the early part of the place field (Quirk and Wilson 1999; Quirk et al. 2001). Thus, early parts of the place field may be more prone to potentiation, providing a potential mechanism for the acquisition of anticipatory place cell coding. As with the backward shifting of place fields, the reduction in spike amplitude attenuation with experience also requires functioning NMDA receptors (Quirk et al. 2001).

Spike backpropagation can also be reduced by inhibitory potentials (Buzsaki et al. 1996; Tsubokawa and Ross 1996). An alternative explanation for the results above could be a decrease in inhibition with experience. Quirk et al. provided evidence against this hypothesis. They found that a reduction of interneuron firing rates could not explain the amount of spike amplitude attenuation; instead, increases in low latency (i.e. ~2-3ms) pyramidal-to-interneuron spike time cross-correlations were observed. Thus, the relative spike times between pyramidal cells and interneurons became more precise with experience.

Others have also investigated trends in the relative timing of place cells via changes in the fidelity of theta phase precession and place cell sequences. A prediction of the place cell sequence models discussed above is that phase precession should be learned

and therefore be absent on early laps in novel environments. Although present, phase precession has been found to be less robust during early exposure to both novel and familiar environments (Mehta et al. 2002; Cheng and Frank 2008). Another study found that while many place cells do have strong phase precession on the first lap in novel environments, the fidelity of place cell sequences is much less robust during early exposure and emerges with experience (Feng et al. 2015). Thus, individual cells may show strong phase precession, but the coordination of phase precession between cells requires experience with the environment.

1.3 – Experience-dependent trends in hippocampal rhythms

It is evident from the discussion above that many types of experience-dependent trends in place cell activity have been identified. Surprisingly though, the corresponding trends in theta and gamma rhythms have not been studied directly. In this section, I discuss alternative hypotheses for the role these rhythms might play in anticipatory place cell coding, and existing evidence for these hypotheses.

The first prediction for how hippocampal gamma should change with experience comes from the model discussed at the end of section 1.1.3 (Jensen and Lisman 1996a). In that model, NMDA-mediated excitation between place cell assemblies is strengthened with experience, allowing cells to overcome inhibition from gamma more quickly. However, the cells also recruit feedback inhibition more quickly such that the net effect is an increase in gamma frequency with experience. Such a mechanism may also underlie

the increase in gamma frequency observed at higher running speeds in rats (Ahmed and Mehta 2012). However, this correlation is less evident in mice (Cheng and Frank 2008).

The model above was originally proposed to explain how theta and gamma may be used for sequence learning in CA3. However, most of the place cell effects discussed in section 1.2 were characterized in CA1. As CA1 has two anatomically-defined gammas (i.e., CA3/MEC-associated slow/fast gammas), predictions for the experience-dependencies of the different gamma subtypes may be motivated by the hypothesized functions of their anatomically-associated afferents. Typically, sequence encoding in the hippocampus is thought to depend on sensory information arriving via its primary extra-hippocampal input from the entorhinal cortex, while sequence storage and retrieval is thought to be supported by the auto-associative recurrent connectivity residing in CA3 (Blum and Abbott 1996; Jensen and Lisman 1996a; Tsodyks et al. 1996). A conceptual model that assumes anticipatory place cell activity and CA1 slow gamma both depend on the efficacy of the CA3 input to CA1 would then predict that CA1 slow gamma should develop with experience.

In support of this second prediction, slow gamma in rats has been shown to increase in amplitude during single traversals through a place field when cells fire earlier in their fields (Bieri et al. 2014). It was argued that slow/fast gamma correspond to distinct modes of operation that the network switches between on a ~1-3 sec timescale to perform memory retrieval/encoding operations, respectively. Some have suggested that this idea may not be so straightforward by demonstrating that slow and fast gamma often co-occur and are both able to affect place cell spiking during the same field traversal (Lasztóczki

and Klausberger 2016a). Importantly, however, this study was performed in head-fixed mice exploring a virtual environment, and the mouse gamma-running speed correlation may well explain the increased co-occurrence of slow and fast gamma that was observed, as both gamma subtypes have been found to increase in amplitude with running speed (Chen et al. 2011). Lasztóczki and Klausberger also showed an increase in fast gamma amplitude at the end of the place field, and it was suggested that MEC input during fast gamma may provide a cue early in the theta cycle, which initiates an internally generated sequence coordinated by slow gamma late in the theta cycle.

The finding that mouse slow and fast gamma amplitude are both positively correlated with running speed raises a third possibility. Slow and fast gamma amplitude may also be similarly correlated with sequence encoding and retrieval processes and display similar experience-dependent trends by consequence. If gamma amplitude correlations with running speed are important for anchoring theta phase precession to position, then such correlations may become more stable alongside the experience-dependent stabilization of place cell theta sequences. However, in rats, slow and fast gamma correlations with running speed both become weaker across many days of exposure to an initially novel environment (Kemere et al. 2013).

A complication to the above scenarios is that relevant changes may not be expressed by gamma amplitude per se. Rather, the modulation of gamma amplitude by theta phase may be the relevant variable. For instance, theta phase modulation of CA3 slow gamma amplitude has been shown to increase as rats learn to associate items to a spatial context (Tort et al. 2009). Importantly, no such changes were seen in overall gamma amplitude.

In the mouse, slow/fast gamma amplitude and their modulation by theta phase are both amplified by running speed (Chen et al. 2011). Thus, the effects are clearly not mutually exclusive and higher order interactions between running speed, theta phase, gamma amplitude and experience become reasonable possibilities.

1.4 – Overview of dissertation

While progress has been made in recent years toward understanding the functional significance of gamma rhythms in relation to anticipatory place cell coding, as well as memory encoding and retrieval, it should be clear that many of the findings remain controversial. Many have pointed out that, even within a given frequency band, multiple functionally distinct rhythms driven by different underlying mechanisms may exist (Whittington et al. 2011; Buzsáki and Wang 2012). Furthermore, as additional behavioral and functional correlates are identified, the number of factors influencing the probability of observing a gamma event at any given time increases. Thus, new analysis methods are needed to handle the added complexity and to encourage reproducibility of results.

This dissertation has two primary goals. The first is to test the prediction that hippocampal theta and gamma rhythm dynamics display consistent reproducible trends that depend on an animal’s experience with its environment. This prediction is most directly tested in Chapter 2, in which I demonstrate that theta and slow gamma amplitude vary over a similar time course to anticipatory place cell firing in mice exploring a familiar circular environment. I show that cross-frequency interactions between these

rhythms, and their modulation by running speed, also vary over time in similar experience-dependent ways.

In Chapter 3, the existence of experience-dependent trends in theta and gamma rhythms are addressed using a triple-transgenic mouse model of Alzheimer's disease. Place fields in these animals were shown to be less stable and less modulated by theta and slow gamma (Mably et al. 2017). Thus, here I study whether the acquisition of anticipatory place cell firing is disrupted in these animals, and whether acquisition of anticipatory firing is associated with similar trends in theta and slow gamma that were described in Chapter 2.

The second goal of the dissertation is to identify novel data analysis methods capable of handling some of the growing complexities involved with studying experience-dependent and behaviorally modulated effects on field potential data. In Chapter 4, I discuss the generalized additive model framework and its application to time-frequency analysis. The chapter partially serves as a tutorial for the statistical models used in Chapters 2-3. I go on to discuss relevant variants of these models and some of the ways in which they may be extended.

In Chapter 5, I summarize and discuss the overall significance of the findings presented in this dissertation. I offer alternative interpretations of the data and identify directions and open questions for future study.

Chapter 2: Experience-dependent trends in CA1 theta and slow gamma rhythms in freely behaving mice

The following chapter is adapted from: Gereke BJ, Mably AJ, and Colgin LL. Experience-dependent trends in CA1 theta and slow gamma rhythms in freely behaving mice. *J Neurophysiol.* 119:476-489, 2018. Gereke BJ designed the experiment, collected a portion of the data, performed the analyses, and wrote the manuscript. Mably AJ collected a portion of the data. Colgin LL supervised the work and contributed to the writing of the paper.

2.1 – Abstract

CA1 place cells become more anticipatory with experience, an effect thought to be caused by NMDA receptor-dependent plasticity in the CA3-CA1 network. Theta (~5-12 Hz), slow gamma (~25-50 Hz), and fast gamma (~50-100 Hz) rhythms are thought to route spatial information in the hippocampal formation and to coordinate place cell ensembles. Yet, it is unknown whether these rhythms exhibit experience-dependent changes concurrent with those observed in place cells. Slow gamma rhythms are thought to indicate inputs from CA3 to CA1, and such inputs are thought to be strengthened with experience. Thus, we hypothesized that slow gamma rhythms would become more evident with experience. We tested this hypothesis using mice freely traversing a familiar circular track for three ten-minute sessions per day. We found that slow gamma amplitude was reduced in the early minutes of the first session of each day, even though both theta and fast gamma amplitudes were elevated during this same period. However,

in the first minutes of the second and third sessions of each day, all three rhythms were elevated. Interestingly, theta was elevated to a greater degree in the first minutes of the first session than in the first minutes of later sessions. Additionally, all three rhythms were strongly influenced by running speed in dynamic ways, with the influence of running speed on theta and slow gamma changing over time within and across sessions. These results raise the possibility that experience-dependent changes in hippocampal rhythms relate to changes in place cell activity that emerge with experience.

2.2 – Introduction

Rodent hippocampal place cells fire at specific spatial locations known as “place fields” as an animal moves through an environment (O’Keefe and Dostrovsky 1971). Place fields are plastic, expanding in the direction opposite of an animal’s motion across repeated passes through the field and thus becoming more anticipatory with experience (Mehta et al. 1997, 2000). The emergence of anticipatory firing differs across the hippocampal subregions. In CA3, it emerges the first time an animal experiences a novel environment and then persists across days (Lee et al. 2004; Roth et al. 2012). In CA1, anticipatory firing is reacquired each day an animal is exposed to a familiar environment (Lee et al. 2004; Roth et al. 2012) but persists across multiple exposures within a day (Yu et al. 2006). As CA1 lacks recurrent excitation, anticipatory firing in CA1 is thought to depend on NMDA receptor-mediated Hebbian synaptic plasticity in feed-forward projections from CA3 to CA1 (Mehta et al. 2000; Mehta 2015). In support of this view,

manipulations that suppress NMDA receptor dependent synaptic plasticity in CA1 have been shown to prevent anticipatory firing (Ekstrom et al. 2001; Cabral et al. 2014a).

Both *in vitro* (Larson et al. 1986; Staubli and Lynch 1987) and *in vivo* (Hölscher et al. 1997; Hyman et al. 2003) evidence has suggested that theta rhythms (~5-12 Hz) promote synaptic plasticity in Schaffer collateral synapses between CA3 and CA1 neurons. Considering that such plasticity is thought to underlie anticipatory firing in CA1 place cells, as described above, theta may also promote the acquisition of anticipatory firing in CA1 place cells. If so, then one would expect theta rhythms to be maximal during the period when anticipatory firing develops, namely the first few minutes of exposure to an environment.

Additionally, CA1 slow gamma rhythms (~25-50 Hz), as opposed to fast gamma rhythms (~50-100 Hz), are thought to reflect times when CA1 responds preferentially to input from CA3. Specifically, slow gamma is coherent between CA1 and CA3 (Colgin et al. 2009; Kemere et al. 2013) and coincides with current sources/sinks in stratum radiatum where CA3 projections terminate (Belluscio et al. 2012; Schomburg et al. 2014). Therefore, it is possible that slow gamma in CA1 emerges with experience, in parallel with experience-dependent anticipatory firing in place cells, as synaptic connections between CA3 and CA1 are modified. Consistent with this possibility, CA1 slow gamma power has been shown to increase during times of anticipatory place cell firing in rats (Bieri et al. 2014).

In the present study, we assessed experience-dependent changes in theta, slow gamma, and fast gamma rhythms in CA1 in freely moving mice. We found that CA1

theta rhythms were strongest during the initial period of exposure to a familiar environment, while CA1 slow gamma rhythms developed with experience, as did anticipatory place cell firing in CA1. In contrast, fast gamma rhythms were not strongly affected by experience across sessions.

2.3 – Materials and Methods

2.3.1 – Subjects and testing procedures

Data were obtained from 3 C57BL/6 and 3 C57BL/6 x 129 hybrid 8-9 month old mice during the dark phase of a reverse light/dark cycle (lights off 9 a.m. to 9 p.m.). We conducted this study using mice because a more complete understanding of how anticipatory firing in CA1 relates to slow gamma, and inputs from CA3, will require anatomically and temporally precise manipulations of slow gamma-generating circuits, and such manipulations are more amenable in mice. Recordings from the C57BL/6 x 129 hybrid mice were included in a previous study (Mably et al. 2017). Mice were housed in groups initially and then housed individually following surgery. After surgery, mice recovered for at least one week prior to the start of behavioral training and data acquisition. During training, mice were food deprived to ~90% of their free-feeding weight and trained to run unidirectionally around a circular track (100 cm diameter, 9 cm width) for three 10-minute sessions per day interleaved with 10-minute rest sessions. During the rest sessions, mice sat in an elevated flowerpot placed near the track. Small amounts of cookie cream were delivered as food rewards at a single location on the track. The reward location was fixed within each day but changed pseudo-randomly between

days to prevent accumulation of place fields at particular reward sites (Hollup et al. 2001; Dupret et al. 2010; Zaremba et al. 2017). To ensure familiarity of the track and recording room, all mice were trained for at least 3 consecutive days prior to the first day of data collection. A total of 35 days of data, consisting of 5-7 days/mouse, were collected. All experiments were conducted according to the guidelines of the NIH Guide for the Care and Use of Laboratory Animals under a protocol approved by the UT Austin Institutional Animal Care and Use Committee (Protocol #AUP-2015-00107).

2.3.2 – Microdrive preparation, surgery, and tetrode placement

Microdrives were custom-built using a modified version of a previously published design (Voigts et al. 2013). Drives contained 2 bundles spaced 4 mm apart. Each bundle contained 8 independently moveable tetrodes. Tetrodes were constructed from 17 μm polyimide-coated platinum-iridium wire (California Fine Wire). Electrode tips were plated with platinum to reduce single channel impedances to \sim 150-300 $\text{k}\Omega$ at 1 kHz.

Microdrives were surgically implanted bilaterally in CA1 with coordinates: 2.0 mm AP, \pm 2.0 mm ML, and 0.5 mm DV. In order to anchor microdrives to the skull, 6-7 jewelers screws were placed in the skull, with the two most anterior used as electrical grounds. The microdrives were then secured to the skull with dental acrylic. Tetrodes were lowered \sim 40-100 $\mu\text{m}/\text{day}$, reaching their target location in or near the CA1 cell body layer at \sim 2 weeks after drive implantation. Tetrodes were not moved more than 40 $\mu\text{m}/\text{day}$ on days preceding data acquisition. One tetrode in each bundle was used as a differential recording reference and was placed in a relatively quiet, spike-free area of the overlying cortex. This was confirmed by recording reference tetrodes continuously

against ground. CA1 stratum pyramidale was identified by its electrophysiological signatures (e.g., robust theta rhythms, sharp wave ripple polarity, etc.), as well as the presence of place cell spikes.

2.3.3 – Histology

All recording locations were histologically verified after experiments were completed. First, mice were placed under isoflurane gas anesthesia and given a lethal dose of sodium pentobarbital (i.p. injection). This was followed by transcardial perfusion, first with physiological saline to remove blood from the brain and then with 4% formaldehyde solution to fix the brain. The brain was left to fix for approximately 1 hour following perfusion to allow shrinkage of brain tissue away from tetrodes, thereby ensuring that tetrode tracks would be visible in histological sections (e.g., tracks of two separate tetrodes within the same bundle can be seen in Figure 1A). For verification of tetrode locations, brains were cut coronally (3 mice) or sagittally (3 mice) at 30 μ m and stained with cresyl violet. Each section through the relevant part of the hippocampus was collected. All tetrode locations were identified, and the tip of each tetrode was localized by comparison across adjacent sections.

2.3.4 – Data acquisition

The data acquisition setup consisted of a Digital Lynx 4SX acquisition system, a 64 channel PSR slip-ring commutator, and two HS-36 analog headstages with lightweight fine wire tethers (Neuralynx, Bozeman, MT). For spike detection, signals were digitally bandpass filtered between 600-6000 Hz, and filtered signals that exceeded a threshold (30-60 μ V) set by the experimenter were sampled at 32 kHz. Spike sorting was then

performed offline using an open source cluster cutting package in Matlab (MClust; A.D. Redish, University of Minnesota, Minneapolis). Clustering was performed manually on two-dimensional projections of the spike waveform features (i.e., Energy, Peak, and PeakValleyDiff). Autocorrelation functions were also used to identify well-isolated single units (i.e., units included in the study were required to exhibit a refractory period containing no spikes). For field potential recordings, signals were digitally bandpass filtered between 0.1-500 Hz and sampled at 2 kHz. For position and running speed estimation, position was tracked at a video frame rate of 30 Hz via colored LEDs on the headstages. Position samples were then smoothed using a 2nd order loess filter from the R package *stats* with a span of 6 seconds. Running speed was then estimated as the time derivative of the smoothed position samples. Where noted, running speed was normalized within each day to between 0 and 1 (as in Chen et al. 2011).

2.3.5 – Place cell analyses

1-D circular place maps were computed by binning the spikes into 1 cm bins and dividing the number of spikes in each bin by the amount of time spent in each bin. Place fields were detected by finding the maximal firing rate location across the three sessions. Place field boundaries were set at locations where the firing dropped below 10% of the peak firing rate for 10 consecutive cm on either side of the maximal firing location. Center-of mass (COM) estimates for single laps were computed from single lap place maps, discarding spikes occurring outside the place field boundaries. Field peak was defined as the location of maximal firing rate on each pass. First spike and last spike were defined as the locations of the first and last spikes occurring within the field boundaries

on each pass, respectively. Field size was defined as the integral of the firing rate map with respect to space within the field boundaries for each pass; it was then normalized by dividing by the mean field size across all passes independently for each cell. The within field firing rate was defined as the number of spikes divided by the time spent inside the place field boundaries for each pass; it was then normalized by dividing by the mean within field firing rate across all passes independently for each cell. Field width was defined as the distance between the first and last spike occurring within the field boundaries on each pass. Field width was normalized by dividing by the mean field width across all passes independently for each cell. Skewness was defined as the ratio of the third moment divided by the cube of the standard deviation of the firing rate map within the field boundaries on each pass. The firing rate asymmetry index (FRAI) was defined as in Mehta et al. 2000. Briefly, F1 was the firing rate during the first 50% of spikes, and F2 was the firing rate during the second 50% of spikes occurring on each pass, with $FRAI = (F1 - F2)/(F1 + F2)$. For place cells with multiple fields (138/377), only the field with the highest peak rate was considered. Fields within 15 cm of the reward location were excluded to avoid contamination by spikes occurring during sharp wave-ripples, considering that sharp wave-ripples occur during reward consumption (Buzsáki 1986) and place cells often fire outside of their fields during sharp wave-ripples (Foster and Wilson 2006). As in Lee et al. 2004, cells that fired < 50 spikes/session within their field boundaries, were also excluded. Passes with a mean running speed of <5 cm/sec in either half of the field or less than three spikes were also discarded. A total of 286/377 place fields and 8,758/14,847 passes met these inclusion criteria.

Changes in place field properties over time across the three sessions were quantified by an additive model (see *Statistical analyses* below):

$$y_i \sim session_i + s_{session}(time_i) + \varepsilon_i, \varepsilon \in N(0, \sigma)$$

The response y could be any of the place field properties listed in Tables 1-2 and described above. Separate smooth functions $s_{session}(\cdot)$ were estimated for each session.

2.3.6 – Signal processing

All signal processing was performed using custom Matlab scripts. Time-resolved power was estimated using a complex Morlet wavelet transform with a width parameter of seven periods, evaluated at 50 frequencies logarithmically spaced between 2-100 Hz, and applied to a single channel from a tetrode in the cell body layer of CA1. A tetrode was classified as being in the cell layer if it had a place cell and was later histologically verified to be in or close to the CA1 cell body layer. Amongst these tetrodes, the channel with the largest theta amplitude was selected to be included in the analysis. Theta phase was then estimated using the Hilbert transform of the theta (6-12 Hz) bandpass filtered signal.

To reduce computational burden for statistical analyses, power estimates were down-sampled to the video frame rate of 30 Hz, and all samples within 15 cm of the reward location were discarded. Power was normalized separately for each frequency and day. Normalization was performed by taking a kernel density estimate of the cumulative distribution function (cdf) of the log power using the kcde function from the ks package in R (Duong 2007, 2016). The cdfs were then mapped to z-scores so that the power

distribution for each frequency became normally distributed with mean zero and unit variance, as verified by Q-Q plots.

2.3.7 – Statistical analyses

All statistical analyses were performed using an additive mixed model (AMM) framework. AMMs do not assume a particular form for the estimated effects (i.e., linear, monotonic, etc.) and can help control for variance unique to a specific experiment. They have the general form:

$$y_i \sim \mathbf{A}_i \boldsymbol{\alpha} + \sum_j \omega_{ij} s_j(x_{ij}) + \mathbf{Z}_i \mathbf{b} + \varepsilon_i, \varepsilon \in N(0, \sigma^2 \boldsymbol{\Lambda})$$

Here, y_i is the i^{th} observation. \mathbf{A} is a design matrix for parametric terms with associated parameter vector $\boldsymbol{\alpha}$. The $s_j(\cdot)$ are “smooth” functions over the covariates x_j (i.e., running speed, theta phase, or time within a session) with dummy variables ω_{ij} that allow the functions to vary with respect to another variable (e.g., session). \mathbf{Z} is a design matrix for random effects terms with associated parameter vector \mathbf{b} . ε is the usual error term and is assumed to be normally distributed with variance σ^2 and correlation matrix $\boldsymbol{\Lambda}$, allowing for correlations between the errors to be modeled.

AMMs of this form were fit using the `bam` function for large data from the `mgcv` package (Wood 2004; Wood et al. 2015, 2017) in R (R Core Team 2016). In `mgcv`, the $s_j(\cdot)$ are represented by penalized spline bases (Wood et al. 2015). For efficiency purposes, we used natural cubic splines for all covariates, except theta phase for which cyclic natural cubic splines were used. Functional interactions were fit using tensor

product interaction bases with corresponding natural cubic and/or cyclic natural cubic marginal bases.

Each covariate had an associated smoothness parameter λ_j , which controls the degrees of freedom (df) allocated to the term. A large value of λ_j results in a linear estimate for the term, while a small λ_j allocates some maximum df that was chosen *a priori*. This maximum was set to 10 df for all univariate terms, and 5 df for each dimension of the interaction terms. To ensure an interpretable surface, the maximal df for the running speed-by-time interaction was set to 3 df for both dimensions as the higher running speeds were more sparsely sampled. The values of the λ_j were selected during model fitting with regard to some criterion, allowing the data to determine how strongly each term is penalized. For this criterion, we used restricted maximum likelihood estimation (REML) as it has good numerical convergence properties and offers robustness against misspecification of the error correlation structure (Krivobokova and Kauermann 2007; Wood 2011).

For the random effects terms, the mgcv package implements random factor smooths (Baayen et al. 2018). These terms help control for repeated measurements and are used to estimate deviations from the population mean function at different levels of a grouping factor. This is accomplished by incorporating additional lower order penalties on the linear parts of the functions so that they shrink to constants. Thus, small penalties estimate smooth random functions while large penalties result in random intercepts for each level of the grouping factor. Mice were run on a single experiment per day; therefore, we included random factor smooths for each univariate predictor with *day* as

the grouping factor. This was done to ensure that the variation related to each covariate that was unique to a particular day was taken into account.

To control for correlations between temporally adjacent samples, mgcv allows a first order autoregressive (AR1) correlation structure to be assumed for the errors (Baayen et al. 2018). This term has a parameter, ρ , which describes the expected correlation between adjacent errors. For efficiency purposes, this parameter was estimated by the Yule-Walker method on the residuals of the corresponding model fit without the AR1 term, using the “ar” function from the base stats package in R. Including the AR1 correlation produced similar mean estimates, but more conservative covariance estimates, of the model coefficients.

2.3.8 – Confidence intervals and test statistics

Due to the large size of the local field potential data, AMMs were fit independently for each frequency. To control for multiple comparisons, approximate 95% simultaneous confidence intervals were estimated over all model terms and frequencies jointly using a simulation-based approach (Ruppert et al. 2003). Briefly, the model coefficient estimates were distributed multivariate normal with mean vector $\hat{\beta}$ and covariance matrix Ω . Simulations may be made by multiplying a sample from this distribution with the linear predictor matrix defined on a dense grid of the predictor values. We simulated all the model terms simultaneously 1,500 times for each frequency. The absolute values of the pointwise deviations of the simulations were then standardized, and the maximum standardized deviation across all terms for each simulation was identified. A critical value $m_{1-\alpha}$ was defined as the 95% quantile of the

maximum deviations. For the ‘full’ model, $m_{1-\alpha}$ was ~ 4.8 which resulted in intervals ~ 2.5 times wider than the critical value of 1.96 used for pointwise intervals, and a corresponding pointwise level $\alpha \approx 1.59 \cdot 10^{-6}$. Similar intervals were produced for the place field properties analyses for which models were sampled 10,000 times, which was computationally manageable due to the smaller size of the models.

All test statistics reported in Tables 1-2 (e.g., F-ratios, p-values, etc.) are the default values reported by mgcv and test against the null hypothesis that all coefficients making up a smooth term are identically equal to 0. These values should be regarded as approximations as they are conditional upon the smoothing parameters (i.e., λ_j) selected by the REML estimation. See Wood 2013 and Wood 2017 (sec 6.12) for further details.

2.3.9 – Cross-validation analyses

To compare the predictive strength of *running speed*, *time-within-session* (also referred to as *time*), *theta phase*, and *session* with regard to our observed oscillatory power measurements, we performed leave-one-mouse-out cross-validation analyses on a series of six models:

base:

$$power_f \sim session + s(speed) + s(phase) + ti(speed, phase) + fs(speed|day) + fs(phase|day)$$

$$+ \varepsilon, \varepsilon \in N(0, AR1)$$

$$+ \text{time: } power_f \sim RHS_{base} + s(time) + fs(time|day)$$

$$+ \text{time-by-session: } power_f \sim RHS_{base} + s_{session}(time) + fs(time|day)$$

$$+ \text{speed-by-time-by-session: } power_f \sim RHS_{base} + s_{session}(time) + ti_{session}(speed, time) + fs(time|day)$$

$$+ \text{phase-by-time-by-session: } power_f \sim RHS_{base} + s_{session}(time) + ti_{session}(phase, time) + fs(time|day)$$

$$\text{full: } power_f \sim RHS_{base} + s_{session}(time) + ti_{session}(phase, time) + ti_{session}(speed, time) + fs(time|day)$$

In all equations, observation indices are implicit, f indexes frequency, RHS_{base} is the right hand side of the base model, the $s_{session}(\cdot)$ denote separate smooth functions for each session, the $ti_{session}(\cdot)$ are separate tensor product interactions for each session, and the $fs(\cdot | day)$ are random factor smooth functions with day as the grouping factor. Each model was fit using the data from all but one mouse. The data from the withheld mouse were then used to test predictions from the fitted model. Estimates corresponding to the random factor smooth functions were excluded from the predictions. This procedure was repeated for all six mice, and the combined prediction errors were used to calculate r-squared values for each frequency. The cross-validation folds were fit in parallel using the HPC resources at the Texas Advanced Computing Center (TACC) at the University of Texas at Austin.

2.4 – Results

CA1 place cells become more anticipatory with experience in familiar environments, as evidenced by a backward shift of their place fields over time in both rats (Mehta et al. 1997, 2000; Lee et al. 2004), and mice (Cabral et al. 2014a). We attempted to replicate this effect by performing multi-site tetrode recordings (Figure 2.1A) in mice ($n = 6$) running unidirectionally around a familiar circular track for three 10-minute sessions per day. Figure 2.1B shows an example recording from a place cell in this task. The cell fired fewer spikes during the first two laps of the first session, after which its place field expanded backward, remaining stable throughout the following two sessions. To characterize how place fields change on average over time, we considered a number

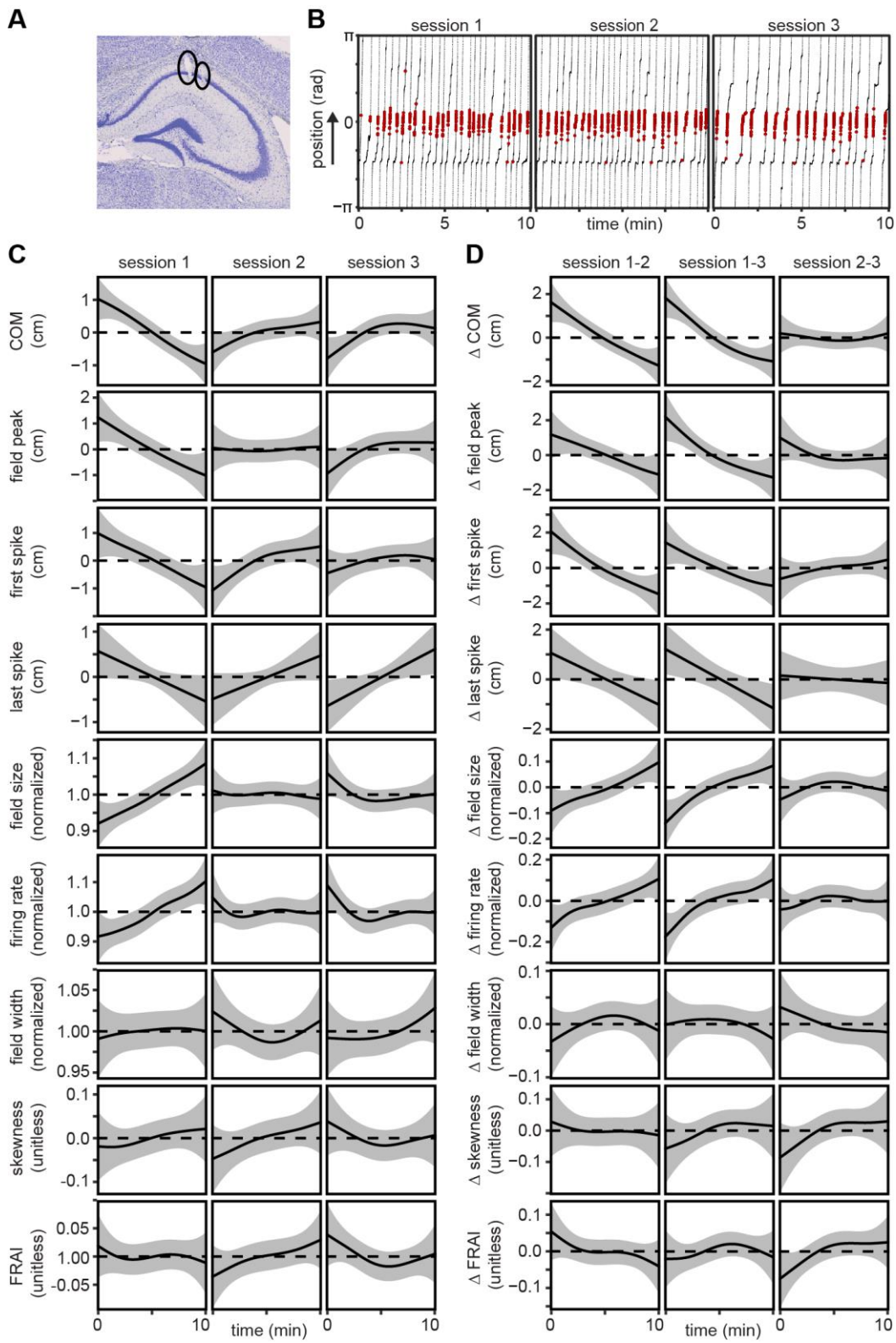


Figure 2.2. CA1 place field properties vary with experience. **A)** Histological section showing example tetrode sites in CA1 cell body layer. Tracks of two individual tetrodes can be seen and are circled in black. **B)** Example spike raster for a single place cell showing the locations of spikes (red dots) across multiple laps around a circular track in sessions 1-3. Fewer spikes were emitted on the first two laps of session one after which the firing rate increased while the place field expanded backwards. No such effect is evident in sessions 2-3. The arrow next to the y-axis denotes the direction of movement. **C)** Experiential changes in place field properties (top-to-bottom: center of mass (COM), field peak, first spike, last spike, normalized field size, normalized firing rate, normalized field width, skewness, firing rate asymmetry index (FRAI)) across time for sessions 1-3 (left to right) for all included place cells. **D)** Differences between the curves shown in C. Left column shows the session 2 curves subtracted from the session one curves, while the middle and right columns show the session three curves subtracted from the session one and two curves, respectively. Gray shaded areas denote 95% simultaneous confidence bands. Corresponding pointwise level $\alpha < 0.01$ for all bands.

Table 2.1. Statistical summary of *time-by-session* curves from Figure 2.1C

Response variable	Ssession1(<i>time</i>)			Ssession2(<i>time</i>)			Ssession3(<i>time</i>)		
	Ref. df	F	p-val	Ref. df	F	p-val	Ref. df	F	p-val
COM	2.49	19.18	$< 10^{-9}$	2.54	3.84	0.02	2.54	6.25	$< 10^{-3}$
Field peak	2.10	10.13	$< 10^{-4}$	2.15	0.14	0.91	2.14	3.99	0.02
First spike	2.14	8.49	$< 10^{-3}$	2.19	6.63	< 0.01	2.18	1.15	0.29
Last spike	1.02	5.50	0.02	1.02	4.53	0.03	1.02	7.71	< 0.01
Field size	2.69	12.68	$< 10^{-6}$	2.75	0.18	0.87	2.75	3.25	0.07
Firing rate	3.87	9.76	$< 10^{-6}$	3.95	1.38	0.30	3.96	4.32	< 0.01
Field width	2.25	0.13	0.89	2.29	1.73	0.15	2.29	1.50	0.20
Skewness	2.10	0.74	0.48	2.15	2.06	0.13	2.15	1.39	0.28
FRAI	2.63	0.61	0.62	2.68	2.31	0.09	2.68	2.31	0.08

Ref. df is the reference degrees of freedom used for approximate F-ratio and p-value computation and is also a measure of curve nonlinearity. Ref. df closer to 1 is more linear. See Wood 2013 and Wood 2017 (sec 6.12) for further details. n = 2701, 2990, and 3067 laps for sessions 1-3 respectively.

Table 2.2. Statistical summary of time-by-session difference curves from Figure 2.1D

Response variable	Ssession1-2(<i>time</i>)			Ssession1-3(<i>time</i>)			Ssession2-3(<i>time</i>)		
	Ref. df	F	p-val	Ref. df	F	p-val	Ref. df	F	p-val
COM	2.15	23.12	<10 ⁻¹⁰	2.14	24.56	<10 ⁻¹¹	2.18	0.02	0.97
Field peak	1.70	6.70	<0.01	1.01	23.47	<10 ⁻⁵	1.01	2.02	0.15
First spike	1.62	17.96	<10 ⁻⁶	1.71	8.84	<10 ⁻³	1.74	1.21	0.21
Last spike	1.01	10.11	<0.01	1.01	13.23	<10 ⁻³	1.01	0.22	0.64
Field size	2.66	7.85	<10 ⁻⁴	2.86	9.83	<10 ⁻⁵	2.91	0.84	0.44
Firing rate	3.25	7.59	<10 ⁻⁴	3.48	10.69	<10 ⁻⁶	3.54	0.79	0.54
Field width	1.73	0.34	0.57	1.88	0.76	0.54	1.91	1.41	0.18
Skewness	1.45	0.19	0.78	1.01	1.85	0.17	1.01	3.68	0.05
FRAI	1.85	2.14	0.13	1.29	0.32	0.62	1.31	5.25	0.01

n = 2701, 2990, and 3067 laps for sessions 1-3 respectively.

of single-pass place field properties that have previously been demonstrated to change in experience-dependent ways (Mehta et al. 1997, 2000; Lee et al. 2004; Cabral et al. 2014a). Figure 2.1C visualizes each of these effects while Table 2.1 provides an associated summary of test statistics. Place field center-of-mass (COM), as well as the locations of peak firing and of the first and last spikes within the field, all shifted backward by ~1-2 cm during the first session (Figure 2.1C; Table 2.1; top 4 rows). This contrasts with sessions two and three where these measures had either negligible or smaller shifts in the forward direction. Place fields also became more robust during the first session as evidenced by an increase in field size and within-field firing rate (Figure 2.1C; Table 2.1; rows 5-6). Again, trends in these measures were either negligible or in the opposite direction during the subsequent sessions. Field size was measured as the integral of the spatial firing rate map within the field boundaries on each pass. Thus, it is influenced by changes in within-field firing rate and place field width. No significant trends were discernable for place field width during any of the sessions (Figure 2.1C;

Table 2.1; row 7), so changes in place field size likely reflected firing rate changes. We found no significant trends in measures of place field asymmetry (skewness and firing rate asymmetry index; Figure 2.1C; Table 2.1; bottom 2 rows). Our results are therefore in line with prior suggestions that location-based measures (e.g., COM) may be more reliable indicators of place field plasticity (Lee et al. 2004; Cabral et al. 2014a).

Figure 2.1D displays between-session comparisons in the form of difference curves for the place field measures described above and shown in Figure 2.1C. These difference curves demonstrate that for all measures containing strong trends in the first session, significant differences are evident between the first and subsequent sessions but not between sessions two and three (Figure 2.1D; Table 2.2). Thus, the experience-dependent, backward shifting of place fields that has previously been reported was replicated in the present data set.

2.4.1 – Theta and gamma power and phase-amplitude correlations increased with running speed

We next wanted to test for the presence of similar experience-dependent trends in CA1 theta and gamma rhythms. In mice, the amplitudes of slow and fast gamma, as well as theta-gamma phase-amplitude correlations, have been reported to increase with increasing running speed (Chen et al. 2011). Moreover, the influence of running speed on theta and gamma in rats has been shown to decrease across repeated exposures to an initially novel environment (Kemere et al. 2013). Thus, we reasoned that the relationships between running speed, theta, and gamma would change over time both within and between sessions in an experience-dependent fashion.

In a setting such as this, with many potential effects (e.g., *running speed*, *time-within-session*, etc.), accounting for the simultaneous influence of the many variables involved can be difficult to accomplish using univariate methods. Multiple regression methods allow for the estimation of the additional contribution each variable makes after being adjusted for the presence of the other variables (e.g., effect of *time-within-session* adjusted for *running speed*). We therefore chose to study the joint effects of *running speed*, *time-within-session*, *theta phase*, and *session number* using an additive mixed model framework (see *Statistical analyses* section in Materials and Methods). This allowed us to estimate the additive contributions of each variable while controlling for the others, as well as for variation in the estimates that may be unique to each experiment (e.g., a particular day of recording). In order to identify the extent to which the effects of each of these predictors changed continuously with frequency in an unbiased way, separate models were fit for 50 frequencies logarithmically spaced between 2-100 Hz. The statistical assumptions of the model were better met by including a first order autoregressive process (AR1) for the residuals to control for the presence of autocorrelation, which was stronger for the lower frequency rhythms (Figure 2.2). Including this term did not strongly alter any of the estimated effects we report ($\rho_{AR1-, AR1+} > 0.99$ for all predictors) but reduced the total amount of autocorrelation, resulting in more conservative confidence estimates.

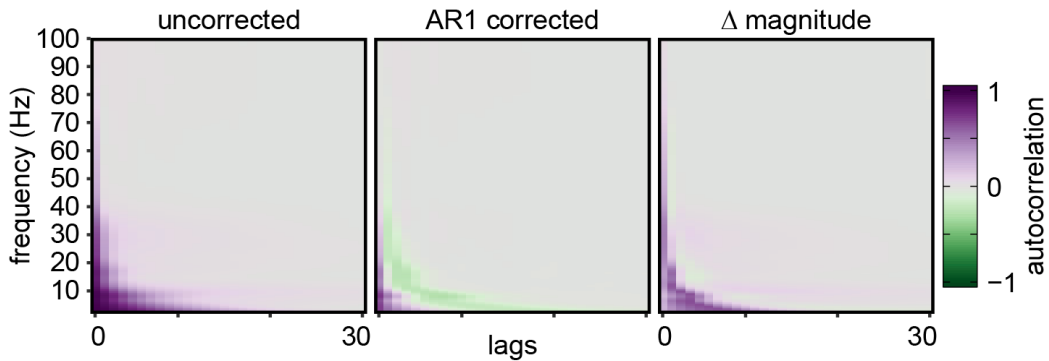


Figure 2.2. AR1 correction of residuals in *base* model. Left panel shows the autocorrelation functions of the residuals for each frequency fit under the *base* model (see text). Middle panel shows the corrected residuals for the same model assuming an AR1 error process. Right panel shows the difference in the magnitude of autocorrelation between the two models, where purple corresponds to less autocorrelation in the AR1 corrected model. One lag is ~ 33 ms, such that the x-axes range from $\sim 0\text{-}990$ ms.

Figure 2.3A (upper panel) shows a one second example local field potential (LFP) recording and associated running speed estimates to illustrate the relationship between running speed and gamma reported by Chen et al. (2011). The amplitudes of theta and slow gamma oscillations can be seen to increase as the animal runs faster. Figure 2.3A (lower panel) shows a similar example in which the amplitude of fast gamma increases with running speed. To quantify these effects on grouped data, we began by fitting a *base* model which included *running speed*, *theta phase*, and a *running speed-by-theta phase* functional interaction as predictors for oscillation amplitude (i.e., power). Figures 2.3B-D display the resulting additive contributions of each of these terms to the overall fit of the model (i.e., the overall prediction of oscillation amplitude made by adding the separate contributions together).

Figure 2.3B shows that power in the delta to low theta range (2-8 Hz) decreased with running speed, while power in the upper theta range ($\sim 9\text{-}10$ Hz) increased with

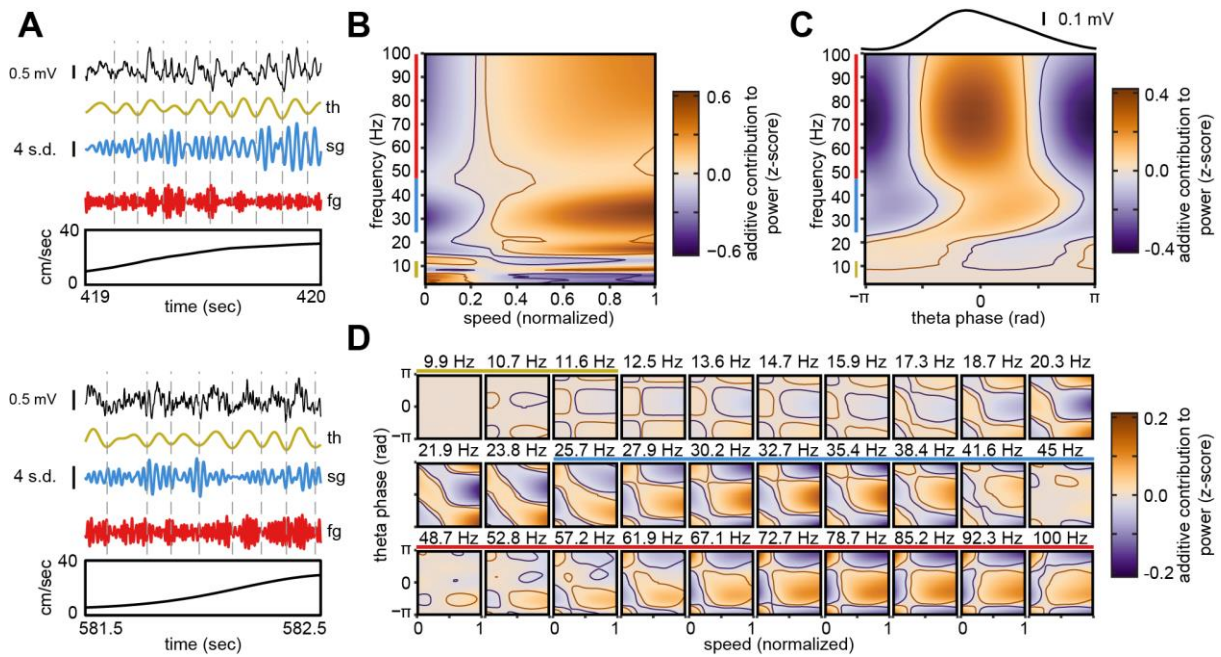


Figure 2.3. Dependence between running speed, theta/gamma amplitude, and theta phase-gamma amplitude correlations. **A)** Example LFP recordings, with bandpass filtered versions for theta (th), slow gamma (sg), and fast gamma (fg) frequencies during periods of increasing running speed. In both the raw and filtered traces of the upper panel, slow gamma amplitude increases with running speed. The lower panel shows a similar example in which fast gamma amplitude increases with running speed. The vertical dashed lines denote theta troughs. **B-D)** Each panel corresponds to a single term in the *base* model (see text). Yellow, blue and red lines on frequency axes denote approximate theta, slow gamma and fast gamma bands, respectively. **B)** Additive contribution of running speed to power at each frequency. **C)** Additive contribution of theta phase to power at each frequency. Black curve above is the mean broadband (i.e., 0.1-500 Hz) LFP at each phase of theta with scale bar for reference. Notice the asymmetry of the theta waveform. **D)** Additive contribution of the *running speed-by-theta phase* interaction to power at each frequency. Each subpanel is the additive effect for a separate frequency, denoted by the labels above the subpanels. Frequencies <9.9 Hz are omitted to conserve space as no significant effects were observed at these frequencies. Only every other subpanel axis is labeled for visual purposes. Orange and purple lines denote 0 level contours of the lower and upper 95% simultaneous confidence bands (corresponding pointwise level $\alpha < 10^{-6}$), respectively.

running speed. These lower and higher frequency theta rhythms may correspond to the atropine-sensitive/resistant theta rhythms that occur during immobility/active movements, respectively (Kramis et al. 1975). We will refer to these as “slow” and “fast” theta for the remainder of the paper. Additionally, theta in rats is known to become less sinusoidal with increasing running speed (Sheremet et al. 2016). That is, the theta cycle often has a faster rise and/or sharper troughs than a pure sinusoid (Figure 2.3A, C). Accordingly, separate putative harmonics, one slow (~11-16 Hz) and one fast (~17-20 Hz), can be seen to decrease and increase, respectively, with running speed (Figure 2.3B).

Consistent with the findings of Chen et al. (2011), power in the slow gamma (~25-50 Hz) and fast gamma (~50-100 Hz) ranges both increased with running speed (Figure 2.3B). This effect differs from what is typically found in rats (Ahmed and Mehta 2012; Zheng et al. 2015), and others have suggested that this increase in slow gamma amplitude with running speed observed in mice may be attributable to a theta harmonic (Kemere et al. 2013). However, example LFP recordings show discernible slow gamma oscillations that increase with increasing running speed (Figure 2.3A), suggesting that this may not be a full explanation.

Figure 2.3C shows the additive contribution of *theta phase* to power at each frequency. As in Chen et al. (2011), slow and fast gamma power were higher around the peak of theta (~0 radians), with slow gamma centered more on the descending phase (Figure 2.3C). We will refer to the theta phases associated with maximal slow and fast gamma power as the “preferred” theta phases of slow and fast gamma. Figure 2.3D shows the additive contribution of the *running speed-by-theta phase* interaction and

conveys how the relationship between theta phase and gamma power changed across different running speeds. Slow and fast gamma power both increased at their preferred theta phases (i.e., ~ 0 - π rad for slow gamma, ~ 0 rad for fast gamma) with faster running speeds (Figure 2.3D), demonstrating that theta-gamma phase-amplitude correlations become stronger at higher running speeds as reported in Chen et al. (2011). Chen et al. (2011) also reported a theta phase shift of slow gamma, but not fast gamma, power with respect to running speed. Here, we observed a shift in the running speed-theta phase interactions across the putative harmonic and slow gamma frequencies (~ 18 - 45 Hz). In the lower part of this range (~ 18 - 24 Hz), high running speed power was increased around the trough and rising phase of theta ($\pm\pi$). Beginning around 25 Hz, a transition occurred as high running speed power became increasingly associated with the preferred phase of slow gamma (i.e., ~ 0 - π ; Figure 2.3D). A theta phase shift of slow gamma power with respect to running speed is also evident. This effect is weakly evident in the lower frequencies of fast gamma (~ 57 - 72 Hz) as well, but is mostly absent throughout the majority of the fast gamma range (>72 Hz). The interpretation of these effects is complicated by coincident changes in the theta waveform shape, which can obscure theta phase estimates, and associated theta harmonics, which can obscure gamma power estimates. However, our findings are generally in line with those of Chen et al. (2011) and demonstrate the strength of the additive model approach taken here.

2.4.2 – Experience-dependent changes in theta and slow gamma

To assess the influence of experience on theta and gamma rhythms, we fit a sequence of five additional models by incorporating *time-within-session* (also referred to

as *time*, *session number*, and their corresponding interactions as predictors. We compared the predictive performances of these models using a leave-one-mouse-out cross-validation approach. Figures 2.4, 2.5, and 2.7 show the additive contributions of each of these terms in the *full* model (see Materials and Methods) that were not included in the *base* model discussed above. These include the *time-by-session*, *running speed-by-time-by-session*, and *theta phase-by-time-by-session* interactions. Incorporating these additional predictors did not alter the estimated effects for the terms in the *base* model ($\rho_{base, full} > 0.99$ for *running speed*, *theta phase*, and *running speed-by-theta phase*). Figure 2.4A shows the additive contribution of *time* for each of the three sessions, while Figure 2.4B displays the corresponding between-session comparisons of these contributions in the form of difference surfaces. Fast theta, slow gamma, and fast gamma power displayed significant trends over time in all three sessions (Figure 2.4A). Power for fast theta (~10 Hz) and its putative harmonic (~20 Hz) decreased over time in all three sessions (Figure 2.4A), and the elevated power at the beginning of the sessions for these frequencies was significantly greater in session one compared to sessions two and three (Figure 2.4B). Conversely, slow theta power was significantly reduced in the initial portion of session one but not sessions two and three (Figure 2.4A). A different pattern was observed for slow gamma power. Like fast theta, slow gamma power decreased over time in sessions two and three (Figure 2.4A). However, this effect was absent in session one in which slow gamma was transiently diminished early in the session (Figure 2.4A, left). Accordingly, there was a significant difference between slow gamma power in the initial period of the first, relative to the second and third sessions, and slow gamma power

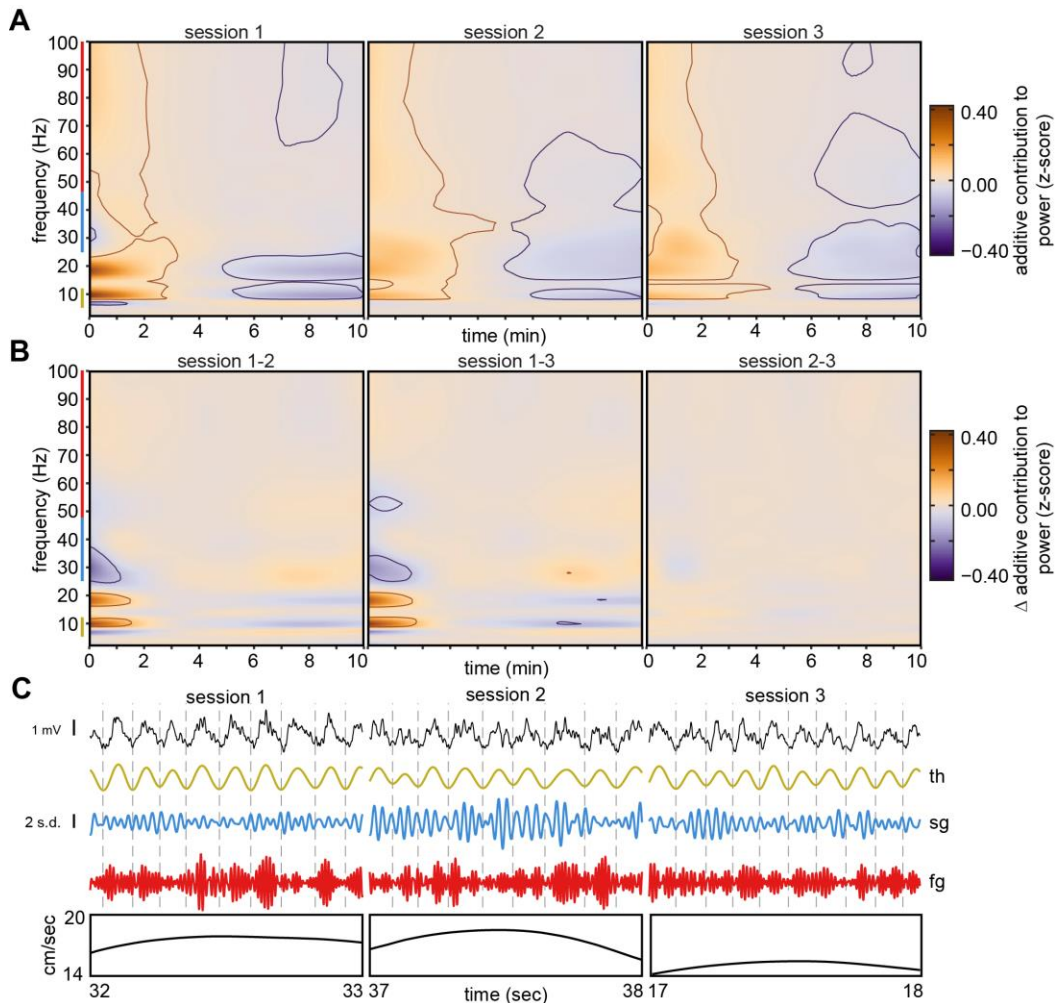


Figure 2.4. Experience-dependent trends in theta and gamma power. **A)** Additive contribution of time-by-session to power at each frequency fit under the full model (see text). **B)** Differences between the surfaces shown in **A**. The left subpanel shows the session two surface subtracted from the session one surface, while the middle and right subpanels show the session three surface subtracted from the session one and session two surfaces, respectively. For both **A** and **B**, the axes on the middle subpanels are not labeled for visual purposes. Orange and purple lines denote 0 level contours of the lower and upper 95% simultaneous confidence bands (corresponding pointwise level $\alpha < 10^{-6}$), respectively. Yellow, blue and red lines on frequency axes denote approximate theta, slow gamma and fast gamma bands, respectively. **C)** Example LFP recordings (top row) from a representative electrode, and bandpass filtered versions for theta (th), slow gamma (sg), and fast gamma (fg) frequencies, during one second intervals within the first minute of sessions 1-3 for which animals ran at similar speeds (bottom row). The vertical dashed lines denote theta troughs. Note how theta amplitude is largest in session 1, whereas slow gamma amplitude is lowest in session 1.

at the start of the second and third sessions were not significantly different (Figure 2.4B).

Fast gamma power significantly decreased across time in all three sessions (Figure 2.4A), and no significant differences in fast gamma power were seen between any of the sessions (Figure 2.4B). Overall, no differences were observed at any time or frequency between sessions two and three (Figure 2.4B, right). Figure 2.4C shows an example LFP recording during a representative one-second period with similar running speed profiles, occurring early in sessions 1-3. Consistent with the results above, theta appears larger in session one, whereas slow gamma appears larger in sessions two and three. These results raise the possibility that increased fast theta power during the period of initial exposure to a familiar environment within each day may play a role in the acquisition of anticipatory firing that also occurs during this time period. Moreover, the recovery of slow gamma power that occurs after each day's initial exposure to a familiar environment may reflect an increase in the effective CA3 input to CA1 that develops with experience.

2.4.3 – Experience-dependent trends in the influence of running speed on theta and gamma rhythms

Figure 2.5 shows the additive contributions of the *running speed-by-time* interaction to the power of each frequency during each session. To interpret this figure, it is important to remember that each of the contributions here are additive with respect to the corresponding contributions from the main effects of running speed for each frequency (see Figure 2.3B). Thus, it communicates how the strength of the running speed modulation of power at each frequency changes slowly over time in each of the three sessions. For example, Figure 2.3B shows that power in the fast theta (~9-10 Hz)

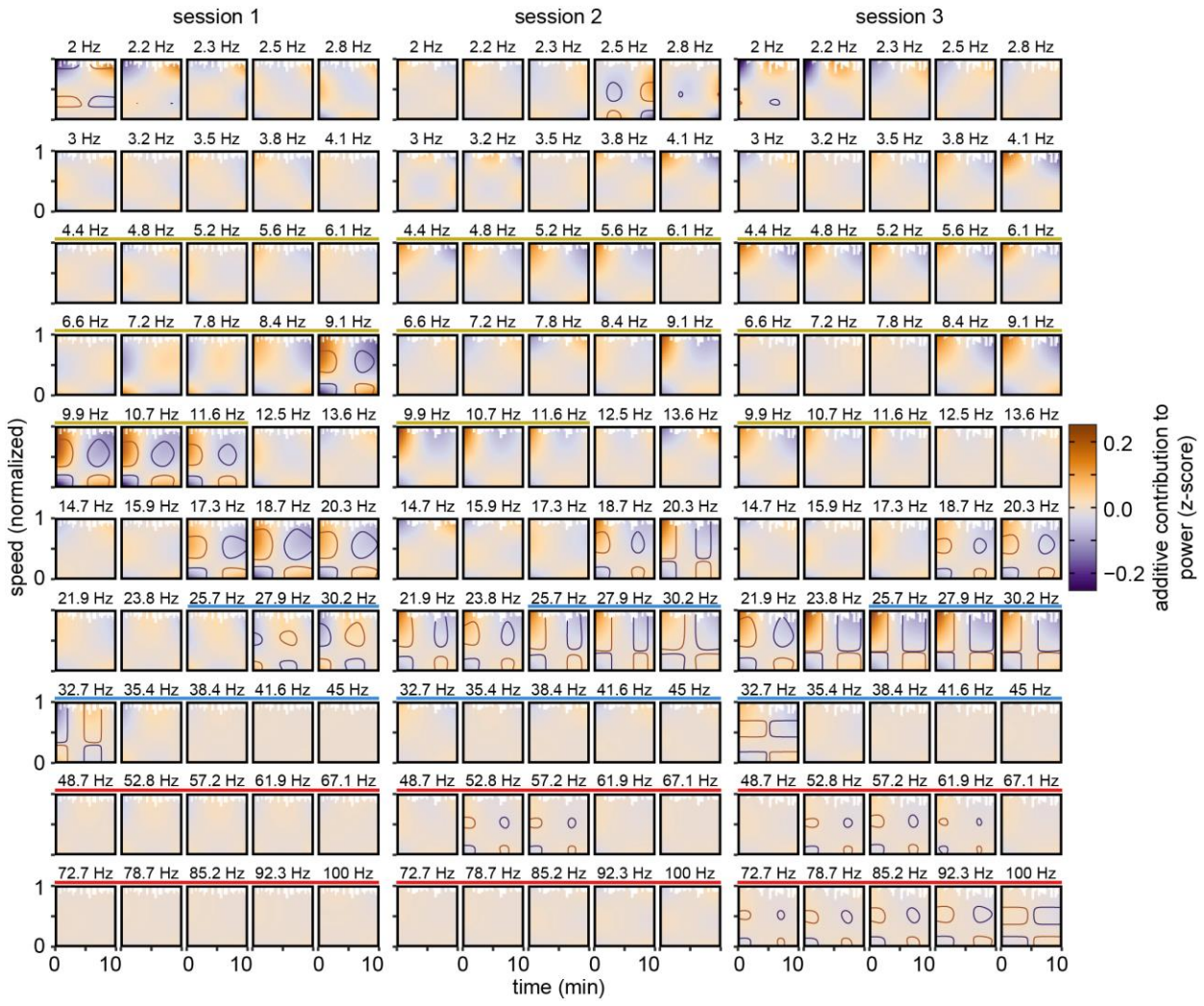


Figure 2.5. Experience-dependent trends in the speed modulation of theta/gamma amplitude. Additive contribution of the running speed-by-time interaction to power for each frequency and session fit under the full model. The left, middle, and right panels correspond to sessions 1-3, respectively. Each subpanel corresponds to a separate frequency, denoted by the labels above the subpanels, logarithmically spaced between 2-100 Hz. Only every other subpanel axis is labeled for visual purposes. Unvisited pixels are colored white. Orange and purple lines denote 0 level contours of the lower and upper 95% simultaneous confidence bands (corresponding pointwise level $\alpha < 10^{-6}$), respectively. Yellow, blue and red lines above individual subpanels denote frequencies within the theta, slow gamma and fast gamma bands, respectively.

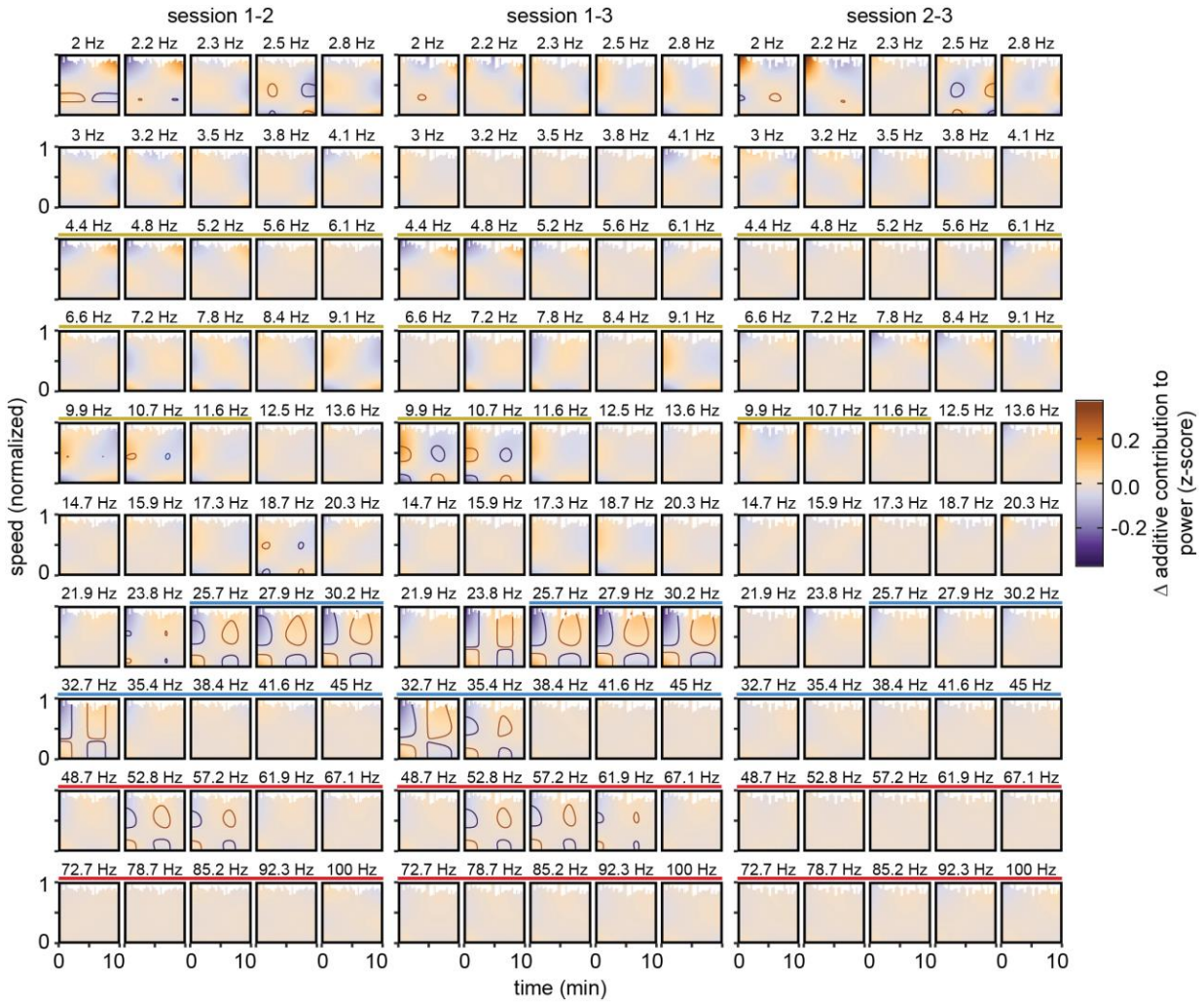


Figure 2.6. Across-session differences in experience-dependent trends in the speed dependence of theta/gamma amplitude. Between-session differences for the surfaces shown in Figure 5. The left panel shows the session two surfaces subtracted from the session one surfaces, while the middle and right panels show the session three surfaces subtracted from the session one and session two surfaces, respectively. As in Figure 5, each subpanel corresponds to a separate frequency, denoted by the labels on top. Pixels not visited in both sessions are colored white. Orange and purple lines denote 0 level contours of the lower and upper 95% simultaneous confidence bands (corresponding pointwise level $\alpha < 10^{-6}$), respectively. Yellow, blue and red lines above subpanels indicate frequencies within the theta, slow gamma, and fast gamma ranges, respectively.

range, and in the range of its putative harmonic (~17-20 Hz), increased with running speed, so Figure 2.5 shows that this increase was significantly greater in the earlier part of session one and became significantly weaker at later times in the session. As the color-coded z-score range in Figure 2.3B is larger than that in Figure 2.5 (~-0.6-0.6 in Figure 2.3B, ~-0.25-0.25 in Figure 2.5), it is not the case that total predicted power for fast theta is decreased at high running speeds in the latter half of session one, but rather that the gain of the effect observed in Figure 2.3B is mitigated. Similar tendencies were observed in sessions two and three, but the decrease in the running speed modulation of fast theta was not identified as significant in these later sessions according to our criteria.

As was the case for the simple effects of *time-by-session* (Figure 2.4), a different pattern of *running speed-by-time* interaction effects was observed for slow gamma. Figure 2.3B shows that slow gamma power increased with running speed. Unlike with theta, however, the magnitude of this power increase for slow gamma was significantly reduced early in session one and became significantly greater over time within the session (Figure 2.5). Conversely, in sessions two and three, the running speed modulation of slow gamma power was greater in the early parts of the sessions and became significantly reduced over time (Figure 2.5). A different pattern of results was observed for fast gamma. While fast gamma power increased with running speed, as was shown in Figure 2.3B, no significant trends in the magnitude of this increase were observed over time within session one (Figure 2.5). In sessions two and three, however, small but significantly negative trends in the magnitude of running speed modulation of fast gamma power were observed (Figure 2.5).

Figure 2.6 shows between-session comparisons of the *running speed-by-time* interactions in the form of difference surfaces for each frequency. Again, no significant differences at theta or gamma frequencies were observed between sessions two and three, and differences between the first session and subsequent sessions were most prominent in the slow gamma range (Figure 2.6). These results suggest that the running speed modulation of slow gamma power changed with experience both within and between sessions. Some small, but significant, differences were observed between all three sessions at low frequencies (<3 Hz), but these effects did not generalize to withheld data (Figure 2.8) and may be explained by the stronger residual autocorrelation at these frequencies which was not fully reduced by the AR1 process (Figure 2.2).

2.4.4 – Experience-dependent trends in theta-gamma phase-amplitude correlations

Figure 2.7A shows the additive contribution to power from the *theta phase-by-time* interactions for each frequency and session, while Figure 2.7B displays the associated between-session difference surfaces for these effects. Both slow and fast gamma power were significantly higher at the rising phase of theta in the early parts of all three sessions (Figure 2.7A). Again, these effects are additive with those reported earlier (i.e., in Figure 2.3C), and the effect sizes are different (~-0.4-0.4 in Figure 2.3C vs. ~-0.15-0.15 in Figure 2.7A). Thus, Figure 2.7A demonstrates that slow gamma power was reduced at its preferred theta phase early in the sessions, resulting in slightly weaker phase-amplitude correlations during these times. This effect was significantly larger in session one compared to sessions two and three (Figure 2.7B). The interpretation for fast gamma is subtler and is consistent with a slight shift from the peak to the rising phase of

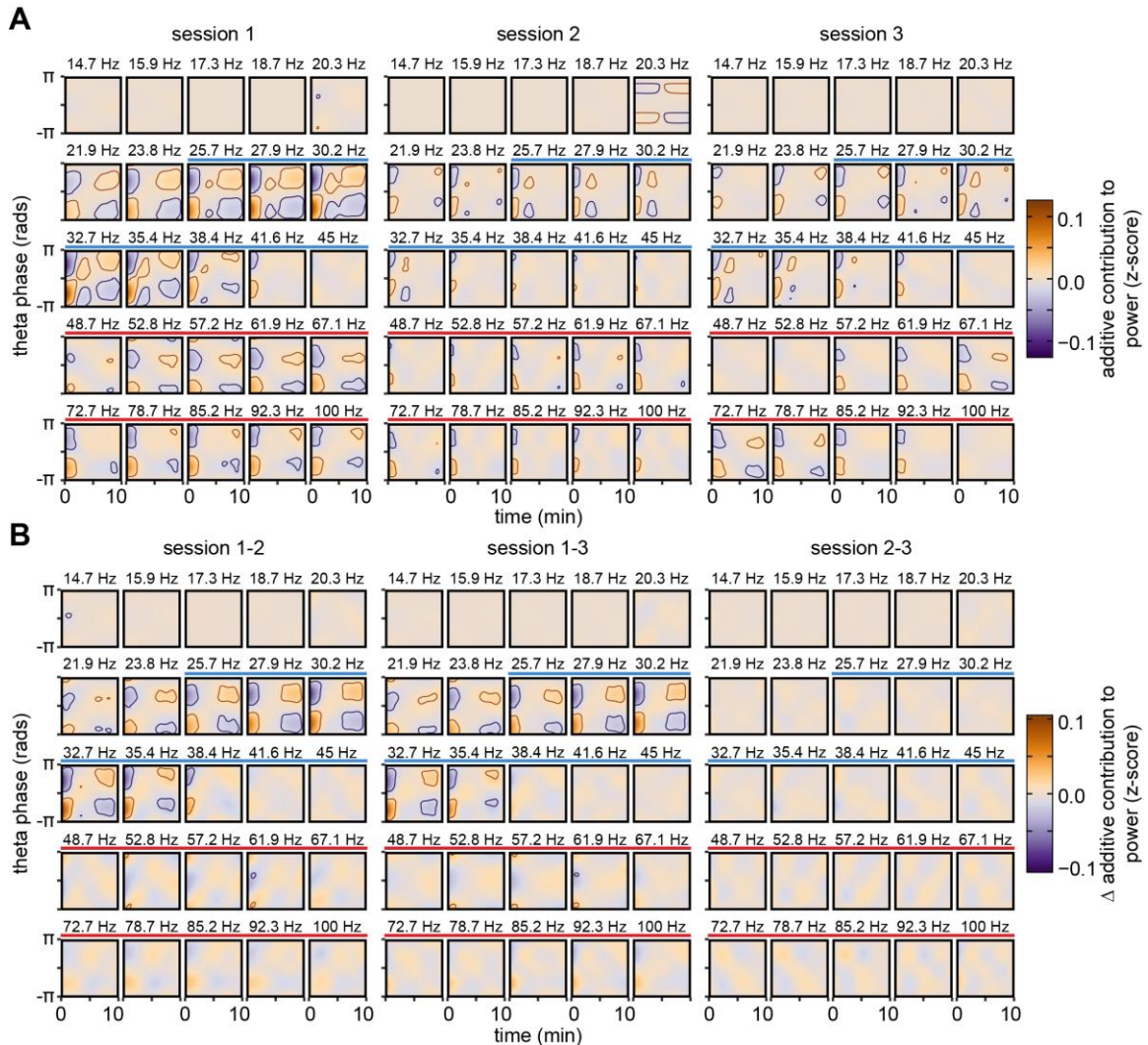


Figure 2.7. Experience-dependent trends in theta phase-gamma amplitude correlations. **A)** The additive contribution of the *theta phase-by-time* interaction to power for each frequency and session fit under the *full* model. The left, middle, and right panels correspond to sessions 1-3 respectively. Each subpanel shows the additive effect for a separate frequency, denoted by the labels above the subpanels. **B)** Difference surfaces for the fits shown in A. The left panel shows the session two surfaces subtracted from the session one surfaces, while the middle and right panels show the session three surfaces subtracted from the session one and session two surfaces, respectively. Only every other subpanel axis is labeled for visual purposes. Orange and purple lines denote 0 level contours of the lower and upper 95% simultaneous confidence bands (corresponding pointwise level $\alpha < 10^{-6}$), respectively. Blue and red lines above subpanels indicate frequencies within the slow gamma and fast gamma bands, respectively. Frequencies < 14.7 Hz are omitted, as no significant effects were observed at these frequencies.

theta early in the sessions. No between session differences were detected for fast gamma, and there were no differences between sessions two and three at any frequency (Figure 2.7B). As with Figure 2.3D, the interpretation of these effects is complicated by potential influences from changes in the shape of the theta waveform and associated harmonics. However, as with the *time-by-session* and *running speed-by-time-by-session* results reported in the previous sections, experience-dependent trends in *theta phase* correlations were confined to the slow gamma range. It is possible that additional trends exist with regard to running speed modulation of theta phase correlations over time, considering the running speed results shown in Figure 2.5. However, we did not explore this effect as it requires estimation of a complicated four-way interaction.

2.4.5 – Cross-validation

We next compared the predictive performance of the different variables on out-of-sample data using a leave-one-mouse-out cross-validation approach (see *Cross-validation analyses* section in Materials and Methods). Six models of varying levels of complexity, ranging from the *base* to the *full* models discussed previously, were compared. For all models, cross-validated R^2 values were typically low (<0.08 ; Figure 2.8). This can be partially attributed to the noisiness of LFPs, and to inter-animal variability; however, it also highlights a need for additional research into the statistical modeling of these signals. Despite the small R^2 values, clear peaks in predictive performance are evident at slow theta (~5-7 Hz), fast theta (~9-10 Hz), and their putative harmonics at ~12-13 Hz and ~17-20 Hz. In addition, large and separate slow gamma (~25-50 Hz) and fast gamma (~60-100 Hz) peaks in predictive performance are also apparent. Figure 2.8B shows the

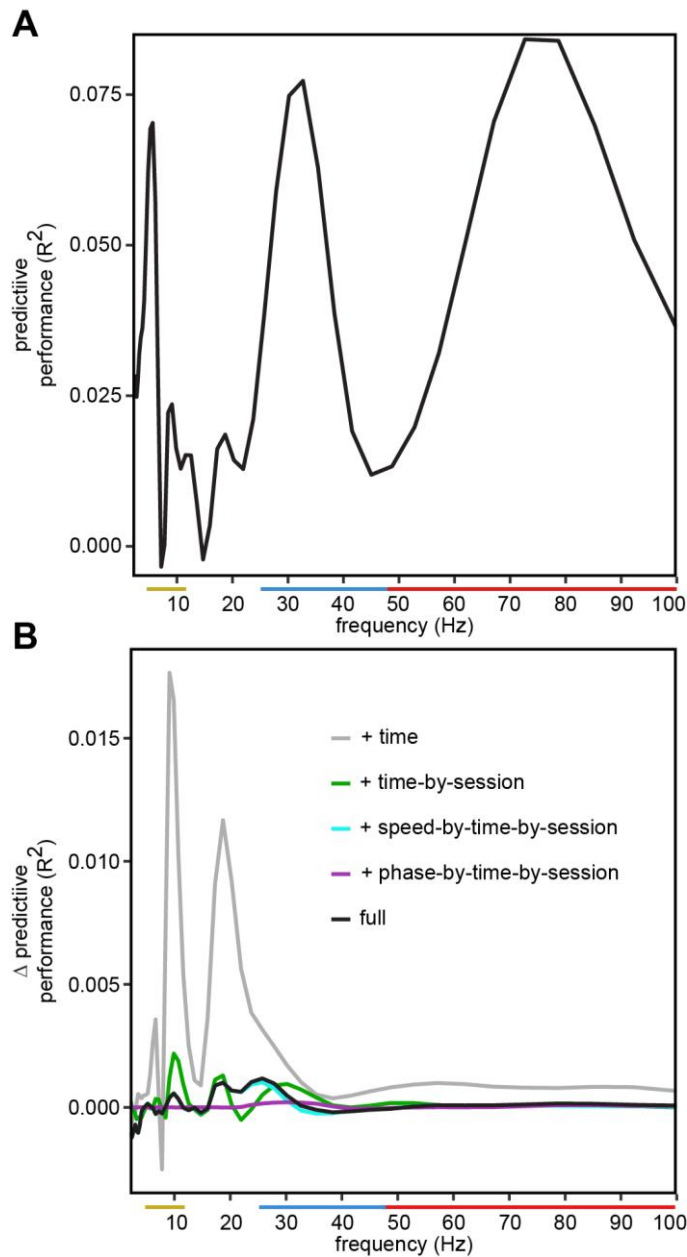


Figure 2.8. Model comparisons. **A)** Overall leave-one-mouse-out cross-validated R^2 for the *full* model at each frequency. **B)** Improvement in R^2 due to including an additional variable. + *time* indicates improvement beyond the *base* model after adding *time*. + *time-by-session* indicates improvement beyond the + *time* model after including *time-by-session*. + *speed/phase-by-time-by-session* indicates improvement beyond the + *time-by-session* model after including *speed/phase-by-time-by-session*, respectively. Similarly, *full* indicates improvement beyond the + *time-by-session* model after including both *speed-by-time-by-session* and *phase-by-time-by-session* simultaneously. Yellow, blue and red lines on x-axes denote approximate theta, slow gamma and fast gamma frequency bands, respectively.

improvement in R^2 gained by including each additional variable. For example, “+ *time*” indicates the improvement beyond the *base* model when the *time* variable is included, “+ *time-by-session*” indicates the improvement beyond the “+ *time*” model when the *time-by-session* variable is included, etc. None of the models had positive improvement at frequencies <3 Hz and ~8 Hz (Figure 2.8B), suggesting that the predictors not included in the *base* model did not generalize well to withheld data at these frequencies. Adding *time* as a predictor improved performance at all remaining frequencies, while incorporating *time-by-session* (i.e., a separate *time* effect for each *session*) offered further improvements in the fast theta, putative fast theta harmonic, and slow gamma ranges (Figure 2.8B). The *full* model also performed best in the fast theta, putative fast theta harmonic, and slow gamma ranges, but incorporating the *speed-by-time-by-session* interaction resulted in larger improvements compared to the *theta phase-by-time-by-session* interaction (Figure 2.8B). Overall, the model comparison conclusions here are in line with the results reported above, which suggest that experience-dependent changes are most prominent at fast theta and slow gamma frequencies.

2.5 – Discussion

The acquisition of anticipatory firing in CA1 with experience in familiar environments is a robust phenomenon that has been replicated in numerous studies in both rats and mice (Mehta et al. 1997, 2000; Ekstrom et al. 2001; Lee et al. 2004; Roth et al. 2012; Cabral et al. 2014a). Somewhat surprisingly however, concomitant trends in the hippocampal LFP have not been studied in detail. Here, we report that such trends are

frequency-specific and can be observed as changes over time in baseline power, as well as changes over time in the dependencies between power, running speed, and theta phase. Specifically, we found that experience-dependent changes in oscillatory power were concentrated in the frequency ranges associated with previously reported hippocampal oscillations (i.e., slow theta, fast theta, slow gamma, fast gamma). Moreover, experience-dependent changes in oscillatory power were strongest at theta and slow gamma frequencies. Baseline power was transiently enhanced for running-related fast theta, and transiently diminished for slow gamma, in the first minutes of exposure to a familiar environment each day. This is the same period during which anticipatory firing is acquired in CA1 place cells. Similarly, the influence of running speed on oscillatory power was transiently enhanced for theta, and diminished for slow gamma, during this same time period. In addition, the influence of theta phase on slow gamma power was also transiently altered. In contrast, fast gamma displayed trends across time within a session that were nearly identical across repeated sessions within a day. Therefore, fast gamma appears to be less influenced by experience than slow gamma or fast theta.

It is possible that experience-dependent trends in oscillatory patterns may provide insights about the emergence of anticipatory firing in CA1 place cells. Our results showed a selective enhancement of oscillatory power in the fast theta range during the initial period of each day's first testing session (Figure 2.4), a time period during which synaptic plasticity that is thought to underlie anticipatory firing (Mehta et al. 2000) presumably emerges. It is possible that strong theta activity in CA1 during this time promotes synaptic plasticity in CA1 synapses (Larson et al. 1986; Staubli and Lynch

1987). Once expressed, such plastic changes could allow place cells to fire in response to lower levels of excitatory input, thereby allowing place cells to fire earlier in their place fields. Others have suggested higher theta frequencies may act as a mechanism to increase the sampling rate of sensory information during locomotion (Fuhrmann et al. 2015). Such a mechanism could also be utilized during periods of elevated attention or general arousal, which may be increased during early exposures to an environment.

Experience-dependent increases in slow gamma power may result from plasticity in CA3-CA1 synapses, signaling an increase in the effective influence of CA3 over CA1. On the other hand, a lack of slow gamma may prevent anticipatory firing in CA1 place cells. We observed a selective suppression of slow gamma during the first moments of the first session of each day that was not observed in later sessions (Figure 2.4). Anticipatory firing is often interpreted as a kind of memory retrieval process at the single cell level, with CA1 place cells retrieving the stored memory of a spatial location from CA3 slightly before the location is actually reached (De Almeida et al. 2012; Bieri et al. 2014). Considering that slow gamma is thought to facilitate transmission of information from CA3 to CA1 in both mice (Chen et al. 2011; Lasztóczki and Klausberger 2014, 2016a; Yamamoto et al. 2014) and rats (Colgin et al. 2009; Belluscio et al. 2012; Kemere et al. 2013; Schomburg et al. 2014), the reduction of slow gamma at the beginning of the first session of each day may reduce transmission of information from CA3 to CA1 and thereby prevent anticipatory firing in CA1.

This viewpoint and the present results are broadly consistent with those of Bieri et al. (2014), who reported a link between place cell anticipatory firing and slow gamma

power in rats. The present results provide evidence that such a link between anticipatory firing and slow gamma rhythms is also present in mice. However, given the differences between gamma in mice and rats (Buzsáki et al. 2003; Chen et al. 2011; Ahmed and Mehta 2012), it remains to be determined if all or any of the experience-dependent effects discussed here also pertain to rats. A recent study in rats reported weaker slow gamma and stronger fast gamma modulation of CA1 place cell spiking during early trials on a familiar linear track (Fernández-Ruiz et al. 2017), which is generally in line with the present results in mice. These effects were interpreted as support for a stronger entorhinal drive to CA1 during early exposures to an environment. Expanding upon this interpretation, our results suggest that this increased entorhinal drive becomes better matched by a stronger CA3 drive upon repeated exposures within a day.

Overall, these results motivate a number of predictions. First, if fast theta-mediated synaptic plasticity underlies the acquisition of anticipatory firing, then disruption of fast theta-generating circuits during the initial part of an experience should prevent or delay the acquisition of anticipatory coding in CA1. Similarly, if slow gamma is enhanced by fast theta-mediated plasticity, then disruption of fast theta during the initial part of an experience should prevent or delay the emergence of slow gamma. On the other hand, disruption of fast theta at later points in an experience should reduce slow gamma power to a lesser extent, or slow gamma power should recover more quickly after a transient reduction. Additionally, if the emergence of slow gamma promotes anticipatory firing, then disruption of slow gamma-generating circuits at any time during an experience should prevent anticipatory firing. Although precise control over the slow

gamma rhythm remains elusive, Blumberg and colleagues (2016) have recently shown that 30 Hz stimulation of the medial septum produces 30 Hz oscillations in the hippocampus. Moreover, efforts to entrain CA1 theta in mice, via optogenetic manipulation of septo-hippocampal circuits, have been fruitful (Bender et al. 2015; Fuhrmann et al. 2015). Thus, these predictions may be testable and offer promising directions for future study.

Chapter 3: Experience-dependent trends in 3xTg mouse CA1 theta and slow gamma rhythms

Figures 3.1 and 3.2 of this chapter were adapted with permission from: Mably AJ, Gereke BJ, Jones DT, and Colgin LL. Impairments in spatial representations and rhythmic coordination of place cells in the 3xTg mouse model of Alzheimer's disease. *Hippocampus*. 27:378-392, 2017. Colgin LL conceived of and supervised the experiments, and contributed to the writing of the published manuscript. Mably AJ designed the experiments, collected and analyzed the data, and wrote the published manuscript. Jones DT collected a portion of the data included in the published manuscript. Gereke BJ designed and performed the initial pilot experiments for this project (not included in manuscript and not shown in this chapter), contributed to the microdrive design for recording neurophysiological signals from freely behaving mice, and helped collect a portion of the data included in the manuscript. Analyses and figures not included in the manuscript (e.g., Figures 3.3-3.7) were done by Gereke BJ.

3.1 – Introduction

Alzheimer's disease (AD) is a progressive neurodegenerative disease representing the most common form of age-related dementia worldwide (Ferri et al. 2005). Early cognitive symptoms are characterized by mild episodic memory impairments, which may be initially confused with normal aging. Episodic memory depends crucially on the hippocampal formation which is among the first set of areas to experience the degenerative effects of the disease (Braak and Braak 1995; Squire et al. 2004). Common

effects include aggregation of amyloid-beta protein (A β), neurofibrillary tangles (NFT) formed by hyperphosphorylated tau protein, as well as synaptic and neuronal loss (Karran et al. 2011). Neuroimaging studies have shown that carriers of familial AD-related gene mutations display abnormal activity in the hippocampal formation many years before onset of clinical symptoms (Mondadori et al. 2006; Filippini et al. 2009; Bateman et al. 2012; Reiman et al. 2012). Thus, hippocampal network dysfunction may represent an early biomarker for the progression of AD.

Although no mouse model of AD fully recapitulates the progressive pathology of the disease, a number of transgenic mouse lines have been created which have provided invaluable insight into aspects less easily studied in humans. Most of these models mimic the accumulation of A β plaques, NFTs, and memory impairments by incorporating human transgenes for mutated amyloid precursor protein (APP), presenilin-1 (PS1), and/or tau (Ashe and Zahs 2010). Several of these lines produce abnormal place cell activity (Cacucci et al. 2008; Cheng and Ji 2013; Zhao Rong et al. 2014; Cayzac et al. 2015; Booth et al. 2016), as well as disturbances in theta and/or gamma rhythms (Rubio et al. 2012; Cheng and Ji 2013; Ittner et al. 2014; Schneider et al. 2014; Cayzac et al. 2015; Ciupek et al. 2015; Iaccarino et al. 2016).

A recent study from our group investigated the disruption of theta and slow/fast gamma coordination of place cells in a widely used 3xTg mouse model (Mably et al. 2017). The 3xTg mouse model includes three AD-linked variants of the above mentioned mutations: APP_{Swe}, PS1_{M146V}, and tau_{P301L} (Oddo 2003; Oddo et al. 2003). By six months of age, these mice show intraneuronal A β in CA1 pyramidal cells accompanied by

deficits in synaptic transmission and LTP, followed by extracellular plaque and tangle formation at later ages (Oddo 2003; Oddo et al. 2003). Behaviorally, 3xTg mice show impairments on hippocampus-dependent spatial reference memory and contextual fear memory tasks as early as 4 months of age (Billings et al. 2005; Giménez-Llort et al. 2007; Sterniczuk et al. 2010; Roy et al. 2016). Specifically, the mice are able to learn normally across trials within a day, but show retention deficits between days of training such that performance on the early trials of each day is degraded relative to the late trials of the previous day (Billings et al. 2005).

In normal rodents, CA1 place fields display a qualitatively similar type of between-day retention effect. During approximately the first minute of exposure to an environment, place cells tend to fire only late in their place fields and then firing shifts backward (opposite the direction of motion), such that place cells become more anticipatory as an animal spends more time in a particular environment (Mehta et al. 1997). Importantly, this effect can be observed at the start of each day's behavioral testing, even in highly familiar environments, suggesting that the spatial representation in CA1 is not fully retained from day-to-day (Lee et al. 2004). The backward shifting of place cells was initially discovered in rats (Mehta et al. 1997) and then subsequently demonstrated in mice (Cabral et al. 2014a; Gereke et al. 2018).

Acquisition of anticipatory place cell firing in CA1 is thought to depend on plasticity in CA3-CA1 synapses (Mehta et al. 2000; Mehta 2015). Furthermore, slow gamma (~25-50 Hz) in CA1 is thought to depend on the efficacy of the CA3 input to CA1, and to correspond to a memory retrieval mode of the hippocampal network (Bieri

2015; Colgin 2015). In rats, slow gamma amplitude is correlated with anticipatory place cell firing (Bieri et al. 2014); and in mice, temporal trends in slow gamma amplitude follow a similar time course to the acquisition of anticipatory place cell firing (Chapter 2 of this dissertation; Gereke et al. 2018).

In this chapter, I address the hypothesis that anticipatory firing in CA1 place cells in 3xTg mice is less retained from day-to-day compared to control mice. As 3xTg mice have been shown to learn normally within a day (Billings et al. 2005), their place fields might be expected to shift backward normally. However, the day-to-day behavioral deficits in memory retention observed in 3xTg mice suggest that 3xTg place cells might display less anticipatory firing during early exposure to an environment each day compared to control mice. We further hypothesized that this effect would be accompanied by a larger decrease in slow gamma amplitude during the same time period as that observed in control mice. Such results would be consistent with the conclusions of Chapter 2 and would be a significant step towards relating memory retention deficits observed in 3xTg mice to known hippocampal network dynamics and single neuron properties. In what follows, I begin by reviewing a subset of the findings from Mably et al. 2017, and then test the hypotheses discussed above.

3.2 – Materials and Methods

The methods are either reported in Mably et al. 2017 and/or are similar to those outlined in Chapter 2 of this dissertation. I include a briefer description here for convenience.

3.2.1 – Subjects and testing procedures

Data were obtained from three B6;129-Psen1^{tm1Mpm}Tg (APP_{Swe}, tauP301L) (3xTg) and three B6;129 hybrid (Wt) 8-9 month old mice during the dark phase of a 12 hr reverse light-dark cycle. Mice were initially housed in groups of their respective genotype. After surgery, mice were individually housed and recovered for at least one week before the start of training and data acquisition. Mice were trained to run unidirectionally around a circular track for small food rewards for three consecutive 10-min active behavioral sessions separated by 10-min rest sessions. Food was delivered at a single track location each day which was moved pseudo-randomly between days to prevent place field accumulation at the reward location (Hollup et al. 2001). Recordings began when LFP signatures indicated that recording tetrodes were in the CA1 cell body layer and when sparse spikes were detected with amplitudes that exceeded a threshold set by the experimenter (see below). During training and data collection, mice were maintained at ~90% of their free-feeding body weight. All experiments were conducted according to the guidelines of the NIH Guide for the Care and Use of Laboratory Animals under a protocol approved by the University of Texas Austin Institutional Animal Care and Use Committee.

3.2.2 – Microdrive preparation, surgery, and tetrode placement

Microdrives constructed using a modified version of an open source design (Voigts et al. 2013). Microdrives contained two bundles, each housing 8 independently moveable recording tetrodes. Tetrodes were platinum-plated to bring single channel impedances to ~150-300 kΩ at 1 kHz. Drives were surgically anchored to the skull using 6-7 small screws and dental acrylic. Tetrode bundles were implanted into the brain

bilaterally using the following coordinates: 2.0 mm AP, \pm 2.0 mm ML, and 0.5 mm DV. Tetrodes were then lowered slowly into CA1 over the course of \sim 2 weeks following surgery. One tetrode from each bundle was kept in a relatively quiet area of the overlying cortex for use as a differential recording reference.

3.2.3 – Histology

All tetrodes and recording locations were verified histologically after completion of the experiments. Coronal (1 mouse) or sagittal (5 mice) 30 μ m slices were stained with cresyl violet. Tetrode tips were identified by comparing tetrode-associated lesions across adjacent sections of the hippocampus.

3.2.4 – Data acquisition

The data acquisition setup consisted of a Digital Lynx 4Sx, a 64-channel PSR commutator, and two HS-36 headstages connected to lightweight, fine wire tethers (Neuralynx, Bozeman, MT). Spikes waveforms were sampled at 32 kHz, and spikes were detected by applying a \sim 50 μ V threshold to bandpass filtered signals (600-6000 Hz). Manual spike sorting was performed offline using an open source Matlab package (MClust; A.D Redish, University of Minnesota, Minneapolis), and was based on spike waveform features (i.e., Energy, Peak, PeakValleyDiff). Putative pyramidal cells were identified based on their firing rates, autocorrelation functions, and spike widths (Fox and Ranck 1981; Harris et al. 2000; Henze et al. 2000). LFPs were sampled at 2 kHz from bandpass filtered signals (0.1-500 Hz). Position was estimated using colored LEDs attached to one of the headstages, and sampled at a video frame rate of 30 Hz. Running

speed was estimated as the time derivative of position samples smoothed using a 2nd order loess filter from the R package stats (6 sec span).

3.2.5 – Place cell analyses

As in Chapter 2, one-dimensional rate maps were computed by binning the animals' circular position into 1 cm bins and dividing the spike count in each bin by the amount of time spent in each bin. Place fields were then detected by finding the maximal firing location across the three sessions, and boundaries were defined as the locations where firing fell below 10% of max for 10 consecutive bins on either side of the maximal firing location. COM was defined as the center-of-mass of the within-field rate map evaluated for each pass. Cells firing <50 spikes/session or with fields <15 cm from the reward location were discarded. Passes with mean running speed <5 cm/sec in either half of the place field, or with <3 spikes, were also discarded. For 3xTg mice, a total of 102/196 place fields and 3,176/5,608 passes met these criteria. For Wt mice, a total of 156/253 fields and 5,666/8,287 passes met the criteria.

3.2.6 – Signal processing

For each day of experiments, the channel with largest theta amplitude among the tetrodes with recorded place cells was selected for inclusion in further analyses of continuous LFP recordings. Time-frequency representations of the LFP for each of these channels were constructed using the continuous wavelet transform with a complex Morlet wavelet (width 7 periods), and evaluated at 50 frequencies logarithmically spaced between 2 and 100 Hz. Wavelets were scaled to unit area (see Chapter 4), and amplitude was taken as the magnitude of the complex-valued transform. Transforms were then

temporally downsampled to the video frame rate of 30 Hz, and samples within 15 cm of the reward location were discarded. Theta phase was estimated by the Hilbert transform method applied to the bandpass filtered signal using the Matlab function fir2 with a Hamming window and stop/pass bands at 4/6 Hz and 10/12 Hz, respectively.

3.2.7 – Statistical analyses

All statistical analyses were performed using the generalized additive mixed model (GAMM) framework (see Chapter 4) and fit using the bam function from the open source R package mgcv. Changes in place field *COM* over time across sessions were estimated by the following additive model:

$$\mu_i = GenSes_i + s_{GenSes}(time_i), COM_i \sim N(\mu_i, \sigma^2)$$

where μ_i is the expected *COM* for the i^{th} observation, and *GenSes* is a six level factor formed by the interaction between *genotype* and *session*. Thus, $s_{GenSes}(time)$ represents a separate smooth function of time for each combination of *genotype* and *session*.

Similarly, for each frequency component of the LFP, *Amplitude* changes across *running speed*, *theta phase*, *time*, *session*, and *genotype* were estimated by the following generalized additive mixed model:

$$\begin{aligned} \text{Log}(\mu) = & GenSess + s_{Gen}(speed) + s_{Gen}(phase) + s_{GenSes}(time) + fs(speed|day) + \\ & fs(phase|day), Amplitude \sim \text{Gamma}\{\mu, \phi(AR1)\} \end{aligned}$$

Here, observation indices are implicit, μ is the expected *Amplitude* at each frequency, $fs(\cdot | day)$ is a random factor smooth for each day, and ϕ is the dispersion (i.e., inverse shape) parameter. An autoregressive term (AR1) was included to control for serial correlations between the measurements.

For the maximum absolute contribution (MAC) of theta phase analysis, a separate MAC value was estimated for each *day* by fitting the following model to the data from each day:

$$\text{Log}(\mu) = \text{Day} + s_{\text{Day}}(\text{phase}), \text{Amplitude} \sim \text{Gamma}\{\mu, \phi(\text{AR1})\}$$

$s_{\text{Day}}(\text{phase})$ was always, by definition, a smooth periodic function of theta phase, centered on one, and representing the multiplicative contribution of each phase of theta to the mean *Amplitude*, μ , for each frequency. Following Kramer et al. 2013, the MAC index for each day and frequency was defined as:

$$MAC_{\text{Day}} = \max\{|1 - s_{\text{Day}}(\text{phase})|\}$$

The MAC index therefore represents the largest proportional change in *Amplitude* occurring at any phase of theta.

Prior to all model fitting, the amplitude spectra from each day were aligned using the function *multiple_align_functions* from the R package *fdasrvf* (Srivastava et al. 2011; Tucker et al. 2013). In all analyses, natural cubic spline, or cyclic cubic spline, bases with 10 degrees of freedom were used for all smooth terms. Smoothness penalty parameters were selected using REML. Unless noted, all confidence intervals are 95% simultaneous intervals estimated using the simulation-based approach with 10,000 and 3,000 draws for the place cell and LFP analyses respectively.

3.3 – Results

Mably et al. 2017 hypothesized that aberrant slow gamma place cell coordination may contribute to the deficits in spatial recall observed in 3xTg mice. This question was

studied by performing multisite tetrode recordings in 8-9 month-old 3xTg ($n = 3$) and Wt ($n = 3$) mice running uni-directionally around a familiar circular track for three consecutive 10-min session per day, separated by 10-min rest periods. Although intraneuronal/extracellular A β deposits were not detected in the 3xTg mice used in this study, they had enlarged ventricles compared to Wt mice, and intraneuronal A β deposits were detected in a separate group of older 11-12 month-old 3xTg mice (Mably et al. 2017). Thus, the experiments were likely performed at a pre-A β stage of pathology.

3.3.1 – 3xTg mice show reduced place cell stability and modulation of spikes by theta and slow gamma phase

Mably et al. 2017 found that the firing locations and firing rates of 3xTg place cells were less stable across sessions compared to Wt. Figure 3.1 shows an unaltered reproduction of Figure 3 from Mably et al. 2017. For each pair of session comparisons, firing locations/rates were less similar in 3xTg mice than in Wt mice (Figure 3.1A, B). Similarities were also found to depend on the sessions being compared (i.e., sessions 1-2 vs. sessions 1-3 vs. sessions 2-3). Interestingly, firing locations/rates appear most similar between sessions two and three in both 3xTg and Wt mice. This may be indicative of experience-dependent effects unique to the first session as described in Chapter 2 (Figure 2.1C, D).

Mably et al. 2017 also found that 3xTg place cell firing locations/rates were less similar across laps within a session compared to Wt place cells. Figures 3.1C, D show example lap-by-lap spike rasters from single Wt and 3xTg place cells, respectively. In these examples, the 3xTg place cell firing appears more dispersed and less regular across

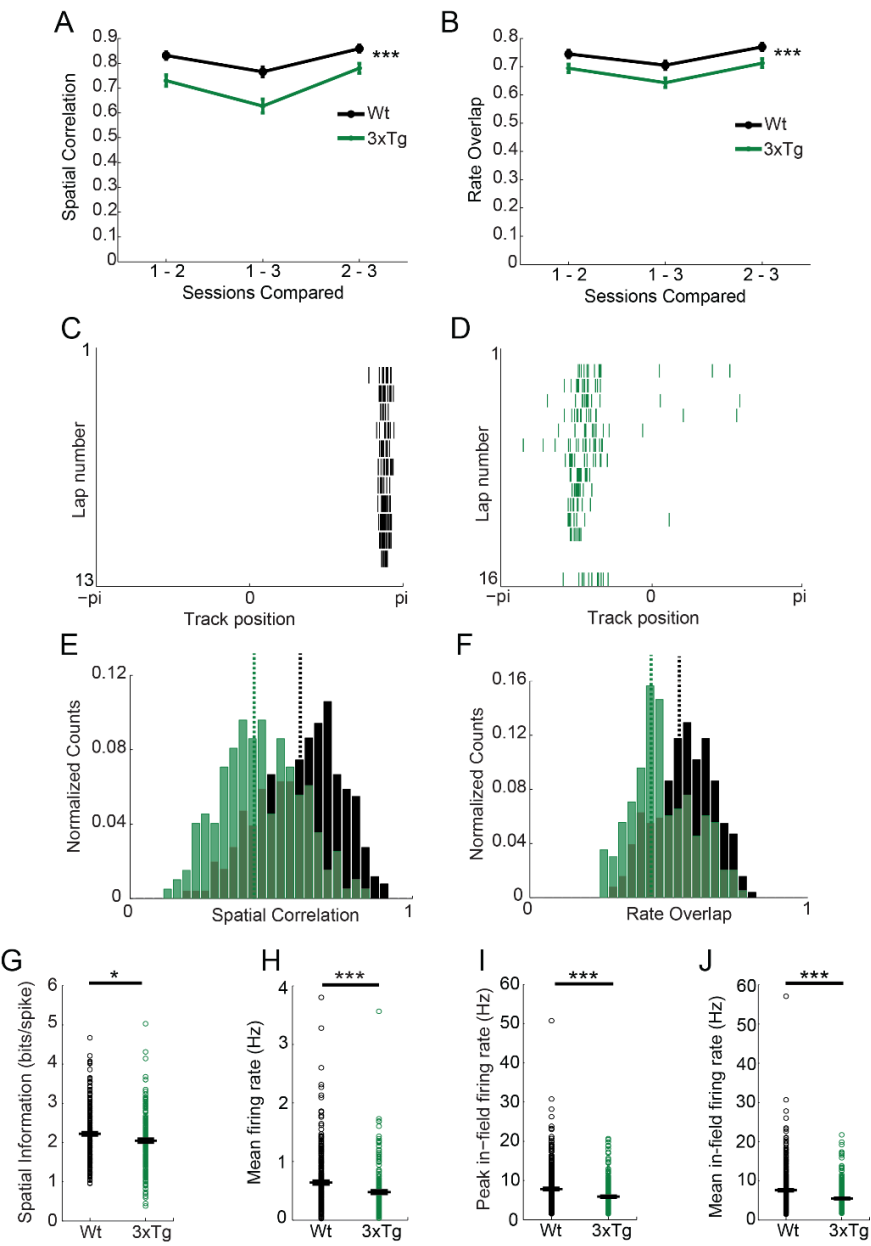


Figure 3.1. Place cell stability across sessions and laps. **A)** Place cell spatial rate map correlations (i.e., “spatial correlation”) between all sessions. **B)** Ratios of place cell mean firing rates (i.e., “rate overlap”) between all sessions. **C)** Example lap-by-lap raster plot for a Wt place cell. **D)** Same for 3xTg. **E)** Distributions of lap-to-lap spatial correlations for Wt and 3xTg place cells. **F)** Same as E but for the rate overlap measure. **G-J)** Place cell spatial information, mean firing rates, peak in-field firing rates, and mean in-field firing rates for 3xTg vs Wt place cells. Reproduced with permission from Mably et al. 2017 (Fig. 3).

laps compared to the Wt place cell. Figures 3.1E, F show that a greater proportion of 3xTg place cells displayed lower lap-to-lap similarity in firing locations and rates, respectively, compared to Wt. Figures 3.1 G-J show that, overall, 3xTg place cells also displayed lower spatial information and firing rates compared to Wt. Thus, 3xTg place cells are abnormal according to many standard place cell measures. As place field sizes were found to be similar between genotypes (Mably et al., 2017), it is unlikely that these abnormalities can be fully explained by differences in place field size. Interestingly, the example 3xTg place cell (Figure 3.1D) seems to shift its firing location consistently across laps, an effect which is not evident in the Wt place cell (Figure 3.1C). This may indicate that a portion of the increased lap-to-lap variability observed (Figures 3.1E, F) may be explainable by consistent trends in firing location across laps within the sessions. Mably et al. 2017 suggested that the 3xTg place cell instabilities described above may be partially related to improper spike time coordination by theta and gamma rhythms. This was assessed by measuring phase-locking of place cells to theta (~6-10 Hz), slow gamma (~25-55 Hz), and fast gamma (~65-100 Hz). It was found that a smaller proportion of 3xTg place cells

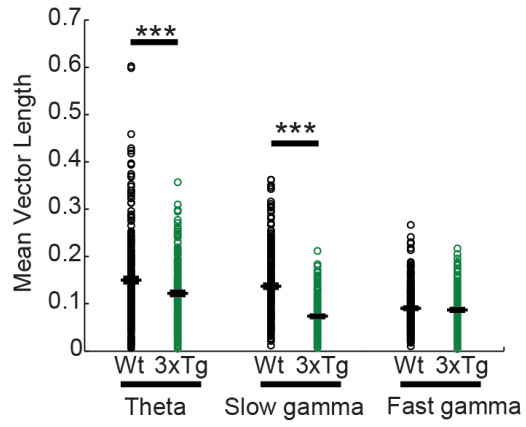


Figure 3.2. Place cell phase-locking to rhythms. Among significantly phase-locked cells, phase-locking to theta and slow gamma was weaker for 3xTg place cells compared to Wt. No differences were observed for fast gamma. Reproduced with permission from Mably et al. 2017 (Fig. 4).

were significantly phase-locked to either theta or slow gamma but that similar proportions of 3xTg and Wt place cells were significantly phase-locked to fast gamma. Figure 3.2 shows an unaltered reproduction of Figure 4B from Mably et al. 2017. Among significantly phase-locked cells, the magnitude of phase-locking to theta and slow gamma was decreased in 3xTg mice, whereas the magnitude of phase-locking to fast gamma was similar between genotypes (Figure 3.2). The specificity of these effects to theta and slow gamma is, again, reminiscent of the specificity of experience-dependent trends to theta and slow gamma amplitude in Wt mice (described in Chapter 2).

3.3.2 – Experience-dependent trends in 3xTg place cells and rhythms

The results from Mably et al. 2017 described above, combined with the retention deficits observed in 3xTg mice (Billings et al. 2005; Giménez-Llort et al. 2007; Sterniczuk et al. 2010; Roy et al. 2016), motivate the prospect of abnormal experience-dependent trends in 3xTG place cell firing, theta, and slow gamma rhythms. We, therefore, decided to test the extent to which lap-to-lap 3xTg place cell variability relates to consistent trends in firing locations across laps. Figure 3.3 displays the average center-of-mass (COM) of 3xTg and Wt place cell firing across time for each of the three sessions. For both genotypes, place cell firing shifted backwards, becoming more anticipatory, across time in the first session. Conversely, trends in the opposite direction were observed in the subsequent sessions. Consistent with the spatial recall deficit hypothesis, 3xTg place cells had a tendency to fire slightly later in their fields early in the first session compared to Wt; however, direct genotype comparisons (Figure 3.3 bottom row) show that no significant differences were observed in any of the sessions. A larger

data sample would increase the likelihood of observing significant differences between genotypes. In any event, these results clearly demonstrate that 3xTg place cells display significant experience-dependent trends in firing location. This is consistent with the normal within-day learning observed in these mice (Billings et al. 2005; Giménez-Llort et al. 2007; Sterniczuk et al. 2010).

We next considered whether deficits in theta and slow gamma amplitude accompany the place cell phase-locking deficits observed by Mably et al. 2017. To consider the simultaneous influences of *running speed, theta phase, time, session, and genotype*, generalized additive mixed models were fit to each frequency (see section 3.2.7). A Gamma response distribution, with a log link function, was chosen in order to make comparisons on the response scale (i.e., amplitude in μV), since amplitude is a continuous and strictly positive measure. Thus, each covariate contributed to the overall fits in a multiplicative fashion.

Variability between days and genotypes was observed in the peak frequencies of theta, slow gamma, and fast gamma (Figure 3.4. To control for a portion of this

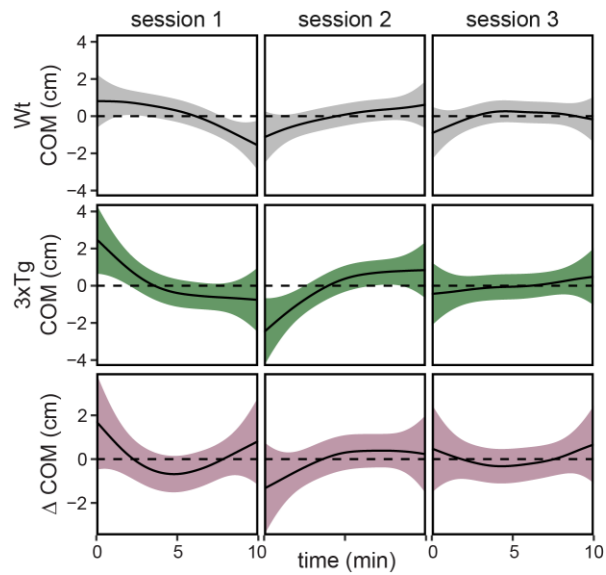


Figure 3.3. 3xTg place cell firing varies with experience. The top/middle rows show the center-of-mass (COM) of place cell firing across the three sessions for Wt and 3xTg mice, respectively. The bottom row shows differences between the curves in the top two rows (i.e., $\text{COM}_{3xTg} - \text{COM}_{Wt}$).

variability, spectra from each day of experiments were aligned, prior to model fitting, using a curve registration algorithm (Srivastava et al. 2011; Tucker et al. 2013). Figure 3.4 shows the mean amplitude spectra for each day

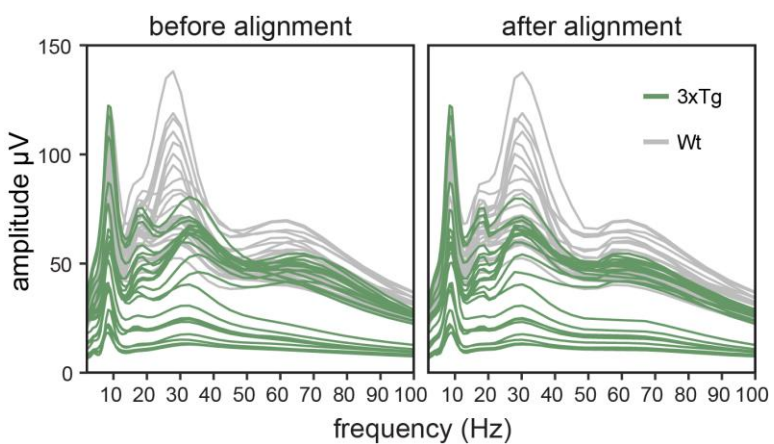


Figure 3.4. Pre-registration of amplitude spectra. **Left)** Mean amplitude spectrum from each day of recording before the frequency registration procedure. Most of the 3xTg (green) slow gamma peaks are at higher frequencies compared to Wt (gray). **Right)** The same data after frequency registration.

before and after the alignment procedure. The frequency peaks were more consistent across days, mice, and genotypes after alignment. Figure 3.5 shows the overall mean amplitude spectra for each genotype in each of the three sessions (i.e., *GenSess* section 3.2.7). 3xTg mice had lower amplitude at every frequency; however, differences were only significant at lower frequencies corresponding to theta (~6-10 Hz) and its putative harmonic (~15-20 Hz). Amplitude spectra were similar across sessions for both genotypes.

Proper coordination of place cell firing presumably depends on proper integration of velocity information. Mouse hippocampal theta and gamma are known to depend strongly on running speed (Chen et al. 2011; Gereke et al. 2018). Thus, an aberrant relationship between running speed, theta, and gamma could help to explain the disorganized place cell firing observed in 3xTg mice. Figure 3.6A shows the

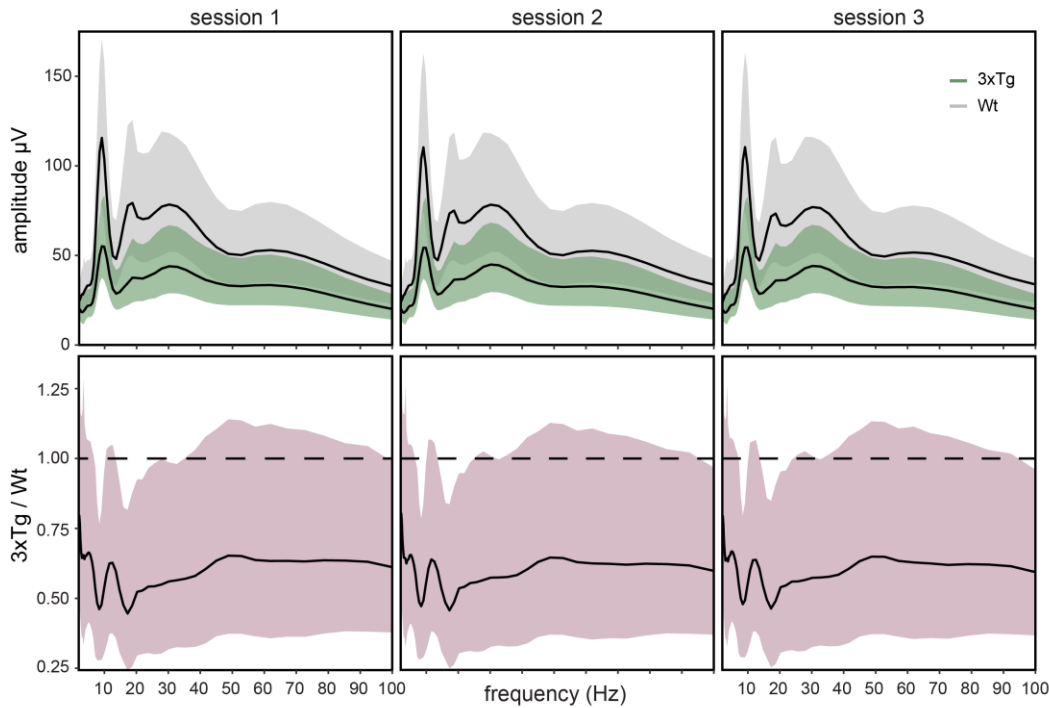


Figure 3.5. Theta amplitude is smaller in 3xTg mice. **Top row)** Mean amplitude spectra for 3xTg (green) and Wt (gray) mice for each of the three sessions. **Bottom row)** Ratios of the 3xTg-to-Wt amplitude spectra. A value of one corresponds to equal amplitude whereas less than one corresponds to a lower amplitude for 3xTg mice. The confidence bands are simultaneous 95% intervals (corresponding pointwise $\alpha \approx 10^{-5}$).

multiplicative contribution of running speed to theta, slow gamma, and fast gamma amplitude. The “multiplicative contribution” describes the amount by which the mean amplitude spectra (Figure 3.5) should be multiplied, given the mouse’s instantaneous running speed, to predict the instantaneous amplitude of each frequency. For both genotypes, the frequencies of theta, and its putative harmonic, increased with running speed. Similarly, the frequencies and amplitudes of both slow gamma (~25-50 Hz) and fast gamma (~50-100 Hz) increased with running speed. The right panel of Figure 3.6A shows the 3xTg-toWt ratio of the running speed contributions. It suggests that the increase in the amplitude of the putative theta harmonic (~15-20 Hz) with running speed

was significantly less pronounced in 3xTg mice. There was also a larger increase in amplitude with running speed at frequencies between slow and fast gamma (~50-60 Hz) in 3xTg mice compared to Wt mice. While the theta harmonic effect may be genuine, considering the other 3xTg deficits observed at theta frequencies, both of these differences may be explained, at least in part, by insufficient frequency registration. For example, many of the smaller 3xTg amplitude spectra (Figure 3.4) have less distinguishable peaks which could promote greater registration errors, and therefore explain why slow and fast gamma appear less distinguishable at high running speeds in 3xTg mice (Figure 3.6A). A single registration of the daily mean spectra is also likely insufficient, and separate frequency alignments at different running speeds may enable more precise inferences.

The theta phase of gamma is thought to influence the theta phase of place cell spiking (Jensen and Lisman 1996a; Fernández-Ruiz et al. 2017). Thus, aberrant phase-locking of 3xTg place cell spiking to both theta and gamma may be indicative of correspondingly aberrant cross-frequency correlations between theta phase and gamma amplitude. Figure 3.6B shows the multiplicative contributions of theta phase to amplitude at each frequency for 3xTg and Wt mice. In Wt mice, gamma was largest on the falling phase, between the peak and trough (i.e., $0-\pi$ rad), of the theta cycle, with fast gamma occurring slightly closer to the peak (i.e., 0 rad). 3xTg slow and fast gamma both had similar theta phase distributions as in Wt, with both perhaps shifted slightly closer to the trough compared to Wt. However, both slow and fast gamma amplitude were significantly less modulated by theta phase overall compared to Wt. A possible

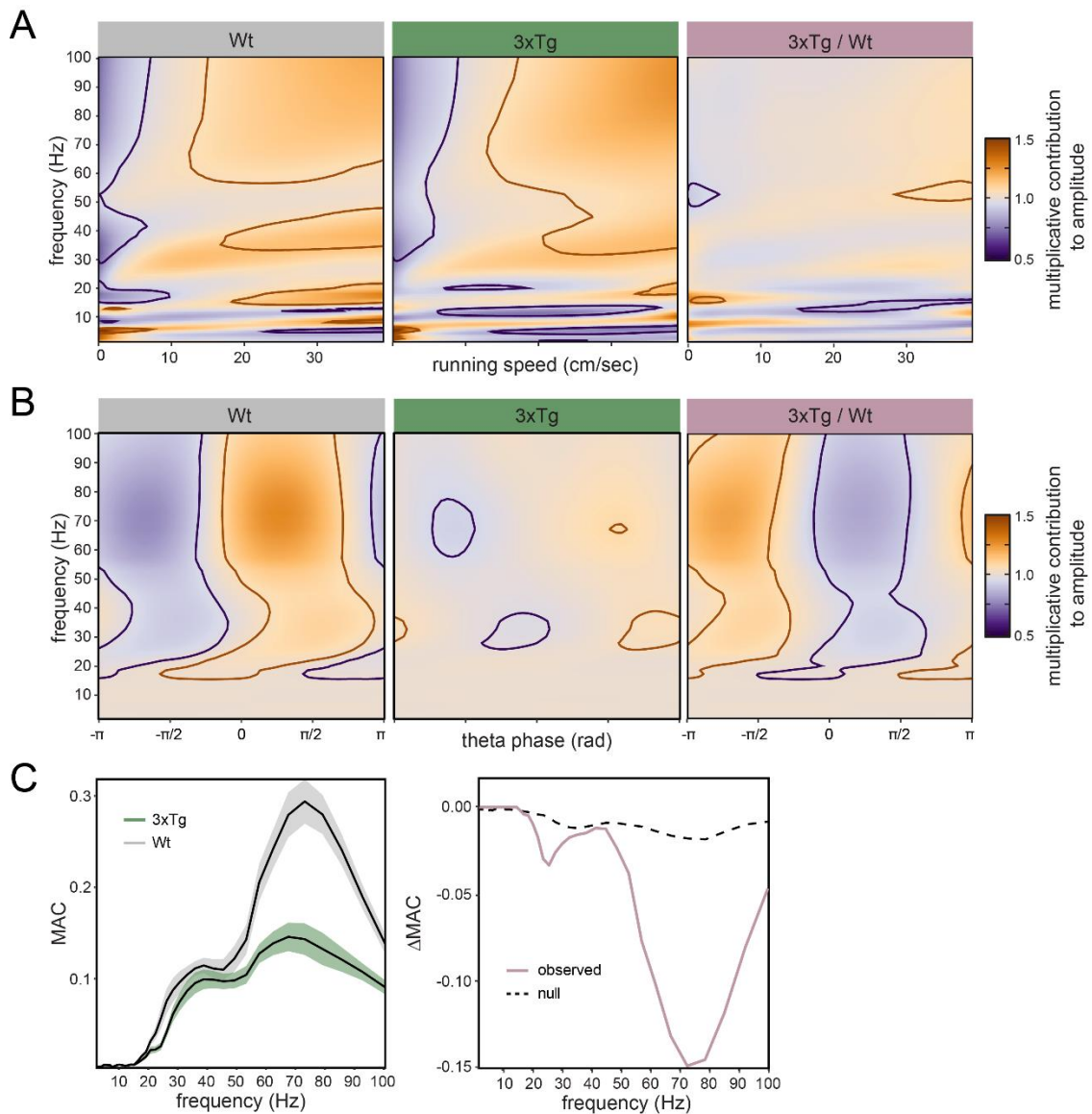


Figure 3.6. Dependence of theta and gamma amplitude on running speed and theta phase. **A)** Multiplicative contributions of running speed to amplitude at each frequency for Wt (left; gray) and 3xTg (middle; green) mice. The right panel shows the ratio of the 3xTg-to-Wt surfaces. **B)** Multiplicative contributions of theta phase to amplitude at each frequency. Orange and purple lines denote one level contours of the lower and upper 95% simultaneous confidence bands (corresponding pointwise $\alpha \approx 10^{-5}$), respectively. **C)** Left panel shows the maximum absolute contribution (MAC) of theta phase for Wt (gray) and 3xTg (green) mice. Shaded areas are 95% simultaneous intervals estimated by a hierarchical normal bootstrap (corresponding pointwise $\alpha \approx 10^{-2}$). Right panel shows the difference between the observed MAC estimates (purple) on the left and the 95% lower bound on null differences (dashed) formed by permuting genotype id's.

explanation for this result is that the preferred theta phase of 3xTg gamma is less consistent across different mice, or days, causing genuine phase-amplitude correlations to cancel out with averaging. To account for this possibility, the maximum absolute contribution (MAC; see section 3.27) of theta phase was estimated separately for each day. Figure 3.6C shows the MAC spectra for both genotypes (left), as well as the between-genotype differences (right). Similar to the analysis in Figure 3B, the contributions of theta phase were significantly smaller in 3xTg mice than in Wt mice for both slow and fast gamma, although differences between genotypes were larger for fast gamma than for slow gamma.

On average, 3xTg place cells displayed normal temporal trends in firing location (Figure 3.3). Therefore, given the results from Chapter 2 (Figure 2.4), 3xTg mice might also be expected to display nominal trends in theta and slow gamma amplitude. Figure 3.7 shows the multiplicative contribution of *time-by-session* for both genotypes, as well as between-genotype comparisons in the form of 3xTg-to-Wt ratio surfaces. Both Wt and 3xTg mice displayed session-specific trends in theta and gamma amplitude that were similar to those described in Chapter 2. These consisted of larger amplitudes of fast theta (~10 Hz) and its associated harmonic (~20 Hz), and smaller amplitude of slow gamma in the early part of session one compared to sessions two and three. However, some differences were observed between genotypes. Compared to Wt mice, the increased amplitude of theta, and its harmonic, early in session one was significantly smaller in 3xTg mice. Similarly, there was less of a reduction in 3xTg slow gamma amplitude early in session one compared to Wt. Conversely, the negative trend in fast gamma amplitude

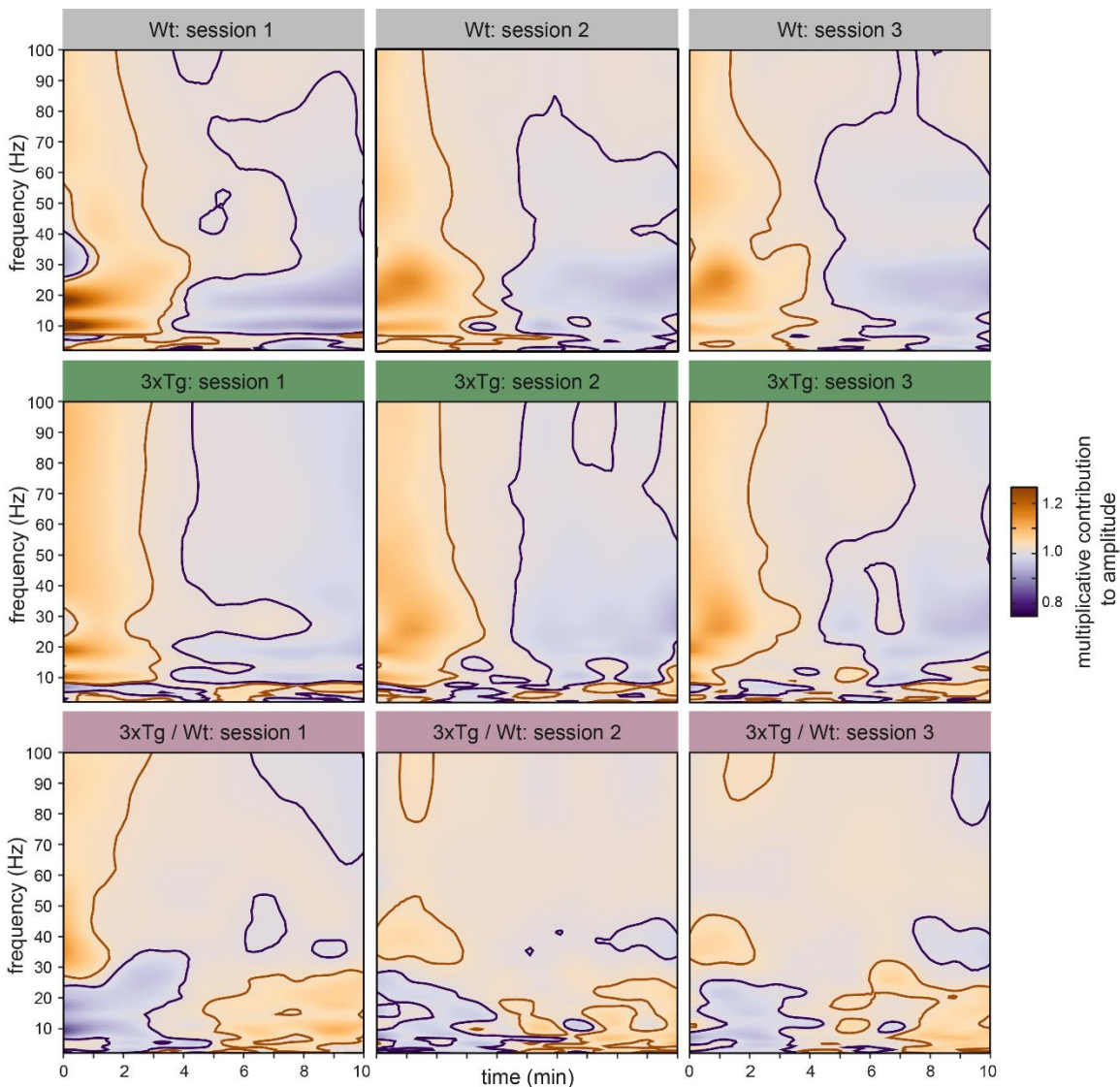


Figure 3.7. 3xTg mice display weaker temporal trends in theta and slow gamma amplitude. **Top row)** Multiplicative contribution of time during sessions 1-3 (left-to-right) for Wt mice. **Middle row)** Same for 3xTg mice. **Bottom row)** Ratio of 3xTg-to-Wt contributions for each session. Orange and purple lines denote one level contours of the lower and upper 95% simultaneous confidence bands (corresponding pointwise $\alpha \approx 10^{-5}$), respectively.

across time in session one was stronger in 3xTg mice compared to Wt. Frequency-specific genotype differences in sessions two and three were similar to those observed in session one. In all three sessions, potential false positives occurred at low frequencies (< ~8Hz). These are likely due to the greater difficulty in incorporating AR1 corrections for serial measurement correlation with non-Normal response distributions such as the Gamma distribution employed here (see discussion in Chapter 4). Serial correlation is strongest at low frequencies, and makes the estimation of temporal trends at these frequencies more challenging. Similar to the place cell analysis (Figure 3.3), this issue would be mitigated by a larger data sample.

3.4 Discussion

Hippocampal network dysfunction is considered a likely mediator of progressive AD-related memory impairments. Mably et al. 2017 investigated hippocampal network dysfunction in the 3xTg mouse model by characterizing its properties at the levels of place cell spiking and coordination of place cell spikes by theta and gamma rhythms. They demonstrated that 3xTg place cells were abnormal using a number of standard measures including: firing rate, spatial information, as well as session-to-session and lap-to-lap stability of firing rate and place field location. These results are broadly consistent with other studies that have found deficits in the expression and stability of place cell firing in both tau and APP mouse models of AD (Cheng and Ji 2013; Zhao Rong et al. 2014; Ciupek et al. 2015; Booth et al. 2016).

Additionally, 3xTg place cell spiking was found to show abnormally low phase-locking to both theta and slow gamma rhythms. Hippocampal slow gamma is thought to

facilitate memory retrieval (Bieri 2015; Colgin 2015), and 3xTg mice typically perform poorly on tasks requiring some form of spatial or contextual recall (Billings et al. 2005; Giménez-Llort et al. 2007; Sterniczuk et al. 2010). Thus, it was proposed that the weaker coordination of place cell spiking by theta and slow gamma rhythms may contribute to the instability of spatial memory representations at pre-symptomatic stages in these mice (Mably et al. 2017).

The analyses presented here supplement Mably et al. 2017 by characterizing the experience-dependent and behavioral correlates of place cells, theta, and gamma rhythms in 3xTg mice. These analyses were motivated by evidence that early memory deficits in 3xTg mice reflect errors in long term memory retrieval, as opposed to storage, processes (Billings et al. 2005; Roy et al. 2016). We found that 3xTg place cells displayed normal trends in firing location. Their place field COM's shifted backward, becoming forward anticipatory during the first session of each day. Final COM locations were retained across rest periods and throughout the two subsequent sessions. Thus, both acquisition and retrieval were seemingly unaffected at the within-day time scale (~10 min) tested here. As expected from a deficit in long term memory retrieval, 3xTg place cells also tended to fire later in their place fields during the early part of the first session of each day; however, this effect was not statistically significant. The behavioral retention deficits observed in 3xTg mice have been shown to depend on the presence of intracellular A β (Billings et al. 2005). A retention deficit at the level of place cell firing may, therefore, be more readily detected in mice at a later stage of progression than the pre-A β mice studied here.

The trends in place cell firing were accompanied by simultaneous trends in theta and gamma rhythms. These largely resembled those characterized in Chapter 2; however, 3xTg theta and slow gamma trends were smaller in magnitude compared to those observed in Wt. Conversely, fast gamma trends were larger. As discussed above, theta-nested slow gamma dynamics are thought to facilitate memory retrieval processes. On the other hand, fast gamma is thought to reflect high-level processing of sensory information arriving to the hippocampus through the medial entorhinal cortex (Colgin et al. 2009; Bieri 2015; Colgin 2015). Thus, the stronger fast gamma trends observed in 3xTg mice could reflect a greater dependence on sensory, as opposed to previously stored, information during the expression of place fields.

Other basic properties and behavioral correlates were considered in conjunction with the effects above. First, we found that theta amplitude was reduced in 3xTg mice. Similarly, theta phase-gamma amplitude correlations were reduced for both slow and fast gamma subtypes. Lastly, while running speed correlations were similar between genotypes, the largest differences were observed at frequencies corresponding to the theta harmonic. These results are consistent with other reports of either reduced theta, theta phase-gamma amplitude correlations, or running speed correlations in tau or APP mouse models (Scott et al. 2012; Cheng and Ji 2013; Ciupek et al. 2015; Booth et al. 2016). While most available evidence suggests these effects are likely exacerbated by the appearance of A β (Villette et al. 2010; Scott et al. 2012), at least one other study has reported aberrant theta/gamma patterns preceding the appearance of A β (Goutagny et al.

2013). Thus, aberrant theta/gamma patterns may represent an early biomarker for disease progression.

Chapter 4: Time-frequency analysis of brain rhythms using generalized additive models

4.1 – Introduction

Understanding what drives the coordination of large populations of neurons is crucial for deciphering the rules of multiscale organization and computation in the brain. Indicators of coordination are readily observed in the extracellular field potential as oscillatory patterns occurring at different frequencies. It is, therefore, important to understand the variables that govern the spatio- and spectro-temporal evolution of these patterns.

The spectral properties of field potentials are nonstationary, consisting of transient events which persist over a range of time scales. Because of this multiscale non-stationarity, time-frequency analysis has become one of the predominant tools for studying oscillatory dynamics in neuroscience. In this context, time series signals of neural activity are recorded from one or more locations in the brain. Each signal is then converted to a time-frequency representation (TFR) which estimates the amplitude and phase of a signal's frequency components at each point in time. Thus, the TFR represents the time-varying spectral content of a signal.

The value of a particular frequency component at a point in time is influenced by a large number of factors, including: extrinsic covariates such as stimuli or behavioral variables, the past activity of the frequency component, the activities of other frequency

components, as well as the activities of frequency components from signals occurring at other locations in the brain. As such, a large number of cross-frequency correlation and functional connectivity measures have been developed to study these different factors.

This situation is analogous to the problem encountered with neural spiking data in that a neuron's spiking must often be simultaneously related to extrinsic covariates, the neuron's past spiking, and the spiking of other neurons. A popular tool for tackling this problem in that arena has been the point process generalized linear model (GLM) (Truccolo et al. 2005; Pillow et al. 2008). GLMs represent a phenomenological class of statistical models that provide tractable descriptions of stimulus-response/input-output transformations that have proven to be valuable for experimental neuroscience.

Despite their utility for spiking data, GLMs have seen comparatively sparse application to the time-frequency analysis of field potentials. In this chapter, I discuss the utility of a semiparametric extension to the GLM called the generalized additive model (GAM). I will begin with an introduction to time frequency analysis with a focus on the continuous wavelet transform and some of its properties. I will then cover some of the relevant background on GAM theory. The goal of the chapter is to serve as a practical resource for non-experts in time-frequency analysis and GAM methodologies. Thus, the chapter will be less concerned with implementation-related ideas and will instead focus on topics such as model specification, checking, and comparison. I conclude by presenting a novel point process model and discuss some areas for future development.

4.2 – Time-frequency analysis

The goal of time-frequency analysis is to transform a one-dimensional signal, measured in time, into a two-dimensional signal in both time and frequency. An often used analogy is the musical score. We would like to know the notes (i.e., frequencies) in the signal, as well as their times of occurrence. A large variety of methods have been developed to achieve this goal. The most popular in neuroscience have been the short-time fourier transform (Gabor 1946; Schaefer and Oppenheim 1989), the continuous Morlet wavelet transform (CMWT) (Morlet et al. 1982; Grossmann and Morlet 1984), the Hilbert transform of filtered signals (Freeman 2007), the Hilbert-Huang transform (Huang et al. 1998), multitapered estimates (Mitra and Pesaran 1999), reassignment methods (Auger and Flandrin 1995; Flandrin et al. 2003; Gardner and Magnasco 2006), matching pursuits (Mallat and Zhang 1993), and autoregressive models (Florian and Pfurtscheller 1995; Ding et al. 2000). The list goes on, and a comprehensive review of these different transforms and methods is well beyond the scope of this chapter. Many reviews at various levels of formalism have been made available (Sejdić et al. 2009; Imran et al. 2009; Wacker and Witte 2013). Instead, I focus on the CMWT because it is among the most popular, simple, and efficient, and has near-optimal performance according to many classical time-frequency resolution measures. Furthermore, many of the methods are nearly equivalent to the CMWT (Chassande-Mottin et al. 1997; Le Van Quyen et al. 2001; Bruns 2004; Kiebel et al. 2005; Iatsenko et al. 2015a).

The CMWT is formed by convolving a discretely sampled length-N signal $y(t)$, for $t = 0: dt: dt(N - 1)$, with the family of Morlet wavelet functions defined at each

frequency f . The Morlet wavelet function is a complex-valued sinusoidal wave modulated by a Gaussian window and is defined by the following equation:

$$\psi_f(t) = A_f(e^{i2\pi ft} - e^{-(2\pi f)^2/2})e^{-t^2/2\sigma_f^2} \quad (4.1)$$

where A_f is a normalizing constant, and the second term in the parentheses is an admissibility term which ensures the wavelet has zero mean. σ_f^2 controls the variance of the Gaussian window and is defined as:

$$\sigma_f^2 = \frac{w_0}{2\pi f} \quad (4.2)$$

where w_0 is a width parameter and can be interpreted as the number of oscillatory periods fitting inside the support of the Gaussian window. It controls the tradeoff between time and frequency resolution such that higher values of w_0 provide better frequency resolution while lower values provide better temporal resolution. In practice, values of $w_0 \approx 5-7$ are used, and for $w_0 > 5$, the second term inside the parenthesis becomes numerically negligible, reducing eq. 4.1 to:

$$\psi_f(t) = A_f e^{i2\pi ft} e^{-t^2/2\sigma_f^2} \quad (4.3)$$

In the frequency domain, the Morlet wavelet can be expressed by taking its Fourier transform:

$$\hat{\psi}_f(\xi) = \mathcal{F}[\psi_f(t)] = B_f e^{-\frac{[2\pi\sigma_f(f-\xi)]^2}{2}} \quad (4.4)$$

where $\mathcal{F}[\cdot]$ denotes the Fourier transform, and B_f is a normalizing constant that depends on the specific choice for A_f in eq. 4.1 (see discussion below). Since the Morlet has a

Gaussian response in both time and frequency (eq. 4.2-4), various definitions for its time-frequency resolution may be devised based on σ_f (Iatsenko et al. 2015a).

With the wavelet definitions in place, the CMWT may be written as:

$$WT(t_i, f) = \int_{-\infty}^{\infty} y(t)\psi_f^*(t - t_i)dt = \mathcal{F}^{-1}\{\mathcal{F}[y(t)] \cdot \mathcal{F}(\psi_f[(t)]\} \quad (4.5)$$

where $\mathcal{F}^{-1}\{\cdot\}$ in the far right expression denotes the inverse Fourier transform, and the product inside the brackets is pointwise. The amplitude, power, and phase at each time and frequency are then defined as $|WT(t_i, f)|$, $|WT(t_i, f)|^2$, and $Arg[WT(t_i, f)]$, respectively. Note, however, that proper interpretation of the first two quantities depends on the choice for the normalizing constant A_f .

Many choices for the normalizing constant appear throughout the literature, but the most conventional is:

$$A_f = \sigma_f^{-1/2} \pi^{-1/4} \quad (4.6)$$

which ensures all wavelets have unit energy (i.e., sum-of-squares equal to one; Torrence and Compo 1998). The original signal can then be reconstructed using the inverse continuous wavelet transform (CWT⁻¹):

$$y(t_i) = \frac{1}{C_{Mor}} \int_{-\infty}^{\infty} \int_0^{\infty} WT(t, f)\psi_{t,f}(t_i) \frac{d\sigma_f dt}{\sigma_f^2} \quad (4.7)$$

where C_{Mor} is called the wavelet admissibility constant and, for the Morlet wavelet, is defined by the equation:

$$C_{Mor} = \int_0^{\infty} \frac{|\hat{\psi}_f(\xi)|^2}{\xi} d\xi \quad (4.8)$$

The energy normalization ensures this quantity is equal for wavelets centered at different frequencies and so the subscript f in eq. 4.8 can be dropped.

The energy normalization discussed above suffers from a number of drawbacks that have created sources of confusion with non-experts. First, it sets the wavelet coefficients to a scale that is not directly interpretable in terms of signal amplitude. Typically with this scaling, $|WT(t_i, f)|$ has units $\frac{\mu V}{\sqrt{Hz}}$ which, when squared, gives $|WT(t_i, f)|^2$ in $\frac{\mu V^2}{Hz}$ (i.e., power spectral density). This de-emphasizes magnitudes at higher frequencies, creating a “1/f” appearance. The attenuation of higher frequencies is inconvenient in terms of visualization, and makes comparison of magnitudes at different frequencies less straightforward, an effect which commonly goes unappreciated. An additional side-effect is that the time-varying peaks in the magnitude spectra, often called ridges, do not coincide with the instantaneous frequency content of the signal (see example below). All of these drawbacks are addressed by replacing the energy-normalization constant with one that, instead, normalizes wavelet area:

$$A_f = \frac{2}{\sigma_f \sqrt{2\pi}} \quad (4.9)$$

In this case, the units for $|WT(t_i, f)|$ are simply μV , which is easier to interpret correctly in most commonly encountered scenarios. The Morlet wavelet with this scaling is sometimes called the normal Morlet in reference to the normal distribution (Liu Lintao et al. 2007), and can be viewed as an instance of the Nadaraya-Watson kernel (Nadaraya 1964; Watson 1964).

Lastly, continuous wavelet transforms, in general, are redundant. In other words, the elements of $WT(t_i, f)$ cannot take on arbitrary values and must satisfy certain

correlation constraints. For the Morlet wavelet, and assuming white noise, the correlation function is (Maraun and Kurths 2004):

$$Cor(t_i, t_j, s_i, s_j) = \sqrt{\frac{2s_i s_j}{s_i^2 + s_j^2}} e^{iw_0 \frac{s_i + s_j}{s_i^2 + s_j^2} (t_j - t_i)} e^{-\frac{(t_j - t_i)^2 + w_0^2 (s_j - s_i)^2}{2(s_i^2 + s_j^2)}} \quad (4.10)$$

where s denotes the scale parameter used in the more general continuous wavelet transform parameterization, and the scale-to-frequency conversion is:

$$f = \frac{w_0 + \sqrt{2+w_0^2}}{4\pi s} \quad (4.11)$$

Figure 4.1 illustrates the above ideas. In the time domain, the area/energy scalings are defined by their unit L1/L2-norms, respectively. This makes the higher frequency wavelets taller and narrower, an effect which is more extreme with the area scaling (Figure 4.1A). In the frequency domain, the energy/area scalings preserve spectral density/amplitude, respectively. Thus, for the energy scaling, wavelets of all frequencies have the same area under their Fourier transforms (i.e., equivalent to constant C_{Mor}); whereas, for the area scaling, the Fourier transforms all share the same peak amplitude (Figure 4.1A). To illustrate the consequences for the CMWT, a four second long synthetic test signal $y(t)$ (Figure 4.1C top) was created by summing two harmonic components:

$$y(t) = y_1(t) + y_2(t) = \left(1 + \frac{9}{4}t\right) \cos(2\pi 5t) + 10 \cos(2\pi 15t + 10\pi t^2) \quad (4.12)$$

The first component, $y_1(t)$ (Figure 4.1C middle), had a constant frequency of 5 Hz, and a variable amplitude which increased linearly from 1-10 (arbitrary units). Conversely, the

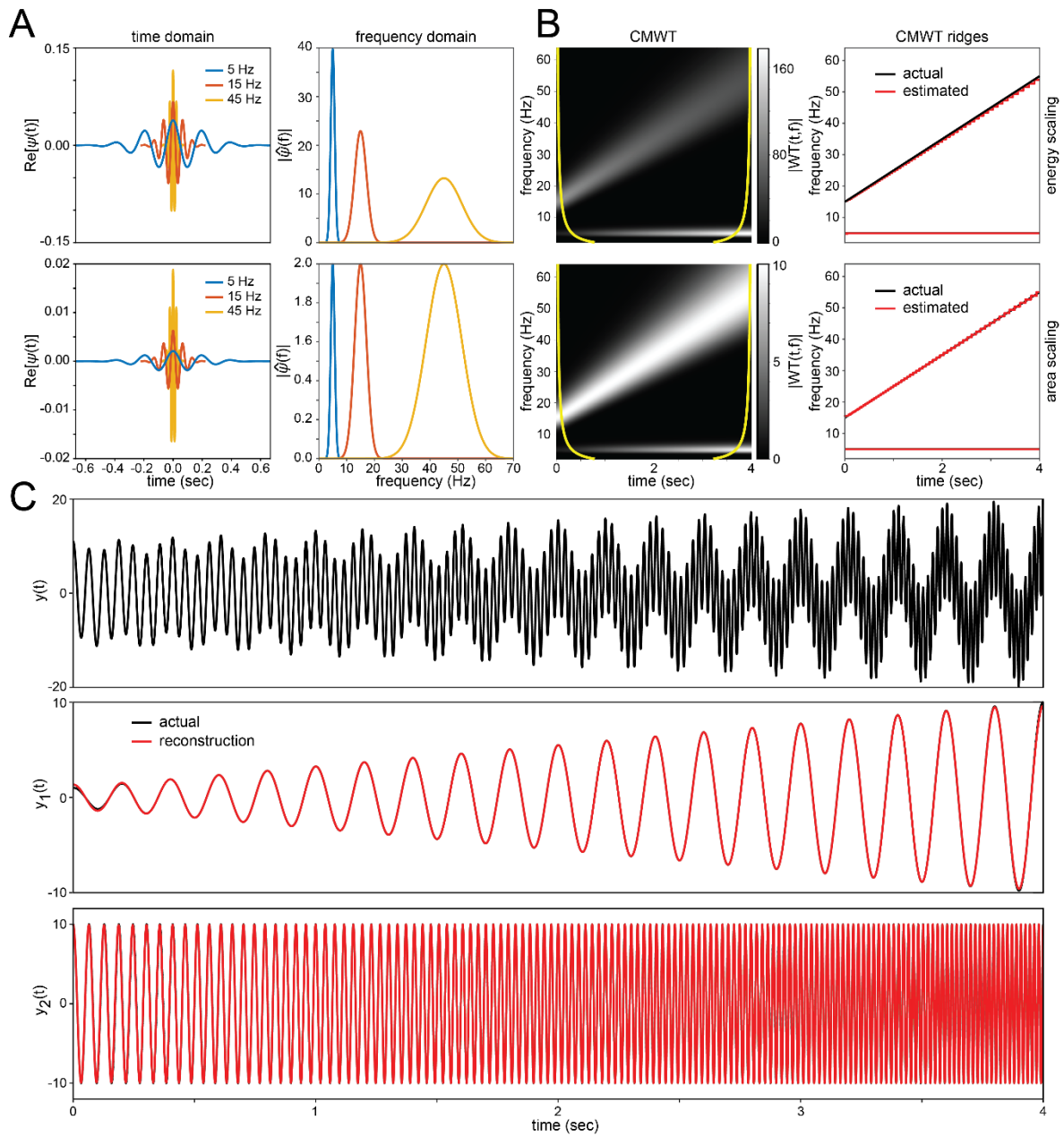


Figure 4.1. Illustration of the continuous Morlet wavelet transform. **A)** Morlet wavelets centered at three different frequencies (5, 15, and 45 Hz; $w_0 = 6$) with energy (top) and area (bottom) scalings, visualized in both the time (left) and frequency (right) domains. Note, only the real part is displayed. **B)** The CMWT magnitude (left), and its associated ridges (right), estimated using the energy (top) and area (bottom) scalings. The yellow lines denote the cone-of-influence (i.e., area with potential edge effects; Liu Lintao et al. 2007), the black lines correspond to the actual instantaneous frequencies of $y_1(t)$ and $y_2(t)$, and the red lines are the ridges estimated from the CMWT's on the left. The aliasing effect (i.e., step-like appearance) of the estimated ridges are due to evaluating the CMWT at a discrete set of frequencies. **C)** The original test signal $y(t)$ (top), and its component signals $y_1(t)$ (middle) and $y_2(t)$ (bottom). The actual signals are shown in black and the reconstructions from the CMWT ridges are in red. The original $y_1(t)$ and $y_2(t)$ are occluded by the reconstructions, which are very good despite the aliasing noticeable in B.

second component, $y_2(t)$ (Figure 4C bottom), had a constant amplitude of 10 (arbitrary units), and a variable frequency which increased linearly from 15-55 Hz. With both the energy and area scalings, two components corresponding to $y_1(t)$ and $y_2(t)$ are clearly distinguished in the CMWT (Figure 4.1B left). However, with the energy scaling, the $y_2(t)$ -associated component appears to decrease in magnitude at higher frequencies even though the amplitude of $y_2(t)$ is constant. Similarly, the magnitude of the lower frequency component appears larger than that of the higher frequency component towards the end of the signal even though $y_1(t)$ and $y_2(t)$ were equal in amplitude at the end of the signal. In contrast, the magnitude of the CMWT, with the area scaling, visually appears as would be expected given knowledge of the test functions. The $y_1(t)$ -associated component has constant frequency with increasing magnitude, and the $y_2(t)$ -associated component has constant magnitude with increasing frequency.

The ridges of the CMWT (Figure 4.1B right) can be determined by detecting the local frequency maxima at each point in time. For the area scaling, the ridges coincide with the instantaneous frequencies of the test signals (Figure 4.1B right). In contrast, for the energy scaling, the ridges are biased to lower frequencies. The magnitudes of the CMWT components, with area scaling, are equal to the amplitudes of the test functions. Thus, the area scaling enables signal reconstruction to be performed without resort to the CWT⁻¹. Figure 4C shows the reconstructions of $y_1(t)$ and $y_2(t)$ which were constructed by plotting the real part of the CMWT, $Re[WT(t,f)]$, evaluated along each of the two ridges. Aside from small errors which occur near the edges of the signal, the reconstructions are nearly perfect.

The demonstration above shows that the CMWT is a useful tool for measuring the instantaneous amplitude and frequency dynamics of multicomponent signals. However, some limitations are important to keep in mind which are most easily communicated by additional examples (Figure 4.2). Consider a signal made up of two harmonic components which intersect in frequency at some point:

$$a(t) = a_1(t) + a_2(t) = 10\cos(2\pi 15t + 10\pi t^2) + 10\cos(2\pi 55t - 10\pi t^2) \quad (4.13)$$

The first component, $a_1(t)$, is the same frequency sweep, $y_2(t)$, from the previous example. The second component, $a_2(t)$, is a sweep in the opposite direction from 55-15 Hz such that the two signals intersect at 2 sec, 35 Hz. Figure 4.2A shows the

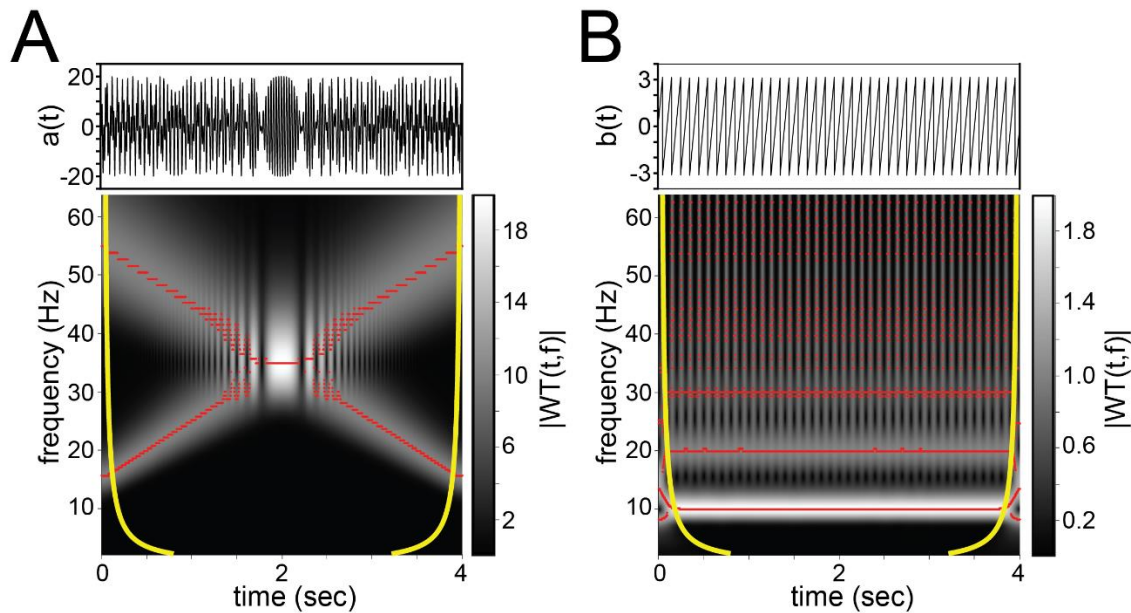


Figure 4.2. Artifacts of the continuous Morlet wavelet transform. **A)** CMWT (bottom) of the two-component signal $a(t)$ (top; see text). **B)** Same as A but for the non-harmonic signal $b(t)$ (see text). Yellow lines denote the cone of influence. Red points are the estimated ridge points. In both plots, ridge point estimation becomes unreliable in areas affected by artifacts (i.e., the interference in A, and the harmonics/vertical stripes in B).

corresponding CMWT with its estimated ridges overlaid. An alternating constructive/destructive interference pattern emerges in the area where the frequencies of $a_1(t)$ and $a_2(t)$ are close (~ 0.75 - 3.25 sec). Oscillatory artifacts also emerge in the ridges which are no longer able to distinguish the two components near their intersection point. Such artifacts can be limited, somewhat, by increasing the wavelet width parameter, w_0 , and thereby the frequency resolution. However, fundamental limits on time-frequency resolution makes these types of artifacts unavoidable.

Consider another signal made up of a single non-harmonic component:

$$b(t) = \text{Arg}[e^{i2\pi 10t}] \quad (4.14)$$

The signal is a saw tooth pattern with an amplitude of π and a fundamental frequency of 10 Hz (Figure 4.2B). Two striking effects are evident from the corresponding CMWT (Figure 4.2B). First, vertical stripes appear at times corresponding to the vertical phase of the saw tooth, $b(t)$. Second, horizontal components concentrate around integer multiples of the fundamental frequency (i.e., around ~ 20 , 30 Hz, etc.). Furthermore, the amplitude of the fundamental frequency component is less than that of the original signal. Thus, the presence of non-sinusoidal waveforms makes the interpretation of instantaneous amplitude less straightforward, and sharp transients in the signal can be seen to induce amplitude across a large range of frequencies. As in the previous example, these issues make accurate component separation, and signal reconstruction based on ridges, more challenging. Creating new algorithms to deal with these types of issues is a major topic in the field of modern signal processing and time-frequency analysis (Mallat 2008; Iatsenko

et al. 2015b, 2016; Meignen et al. 2016; Harmouche et al. 2018; Lin et al. 2018; Xu et al. 2018).

4.3 – The generalized additive model framework

It should be clear from the previous section that separating signals into interpretable time-frequency components is an extremely active area of research. Correspondingly, the number of available methods continues to increase at a rapid pace. However, acquiring time-frequency representations is often only the first step in an analysis, and many challenging issues are encountered in the steps that remain. In neuroscience, one of the biggest challenges is the size of the data. For example, a field potential sampled at 2000 Hz for 30 min has 3.6 million time points. Data is then usually combined across experiments (i.e., days, subjects, etc.), and in the case of the CWMT, the signal is transformed into a number of frequency components. Thus, the size of the data grows by at least an order of magnitude. However, it is important to recognize that transformation into the time-frequency domain does not create new information. Rather, it *re-organizes* existing information into a format which is hoped to be more interpretable. The price paid for interpretability is redundancy. The TFRs are smooth. Thus, points nearby in the time-frequency plane are correlated in a way that depends on both the signal, as well as the transform (eq. 4.10). Moreover, quantities such as amplitude and power are strictly positive, non-normally distributed, heteroskedastic, and exhibit nonlinear relationships with covariates of interest. Thus, a statistical framework that can simultaneously handle these many challenges is highly desirable.

One such framework is the generalized additive model (GAM) discussed here. Assume we are given a vector of observations of a dependent variable/response y_i (e.g., amplitude estimates), and some independent variables/covariates x_{ji} for $i = 1, 2, \dots, N$ and $j = 1, 2, \dots, J$. The goal is to create a model which approximates:

$$y_i = f(x_{1i}, x_{2i}, \dots, x_{Ji}) + \varepsilon_i \quad (4.15)$$

where $f(\cdot)$ could be any function of the combined covariates, and ε_i is some residual noise process centered on $f(\cdot)$. Ideally, the data should determine, as much as possible, the functional form of $f(\cdot)$. However, the space of such functions is, in principle, infinite; and so, some simplifying assumptions must be made to make the problem tractable. In the GAM context, there are typically three main assumptions. First, $f(\cdot)$ is assumed to be smooth. In other words, observations with similar covariate values are assumed to have correspondingly similar mean response values. Second, the amount of data N is always finite and may sparsely fill the covariate space due to the well-known *curse of dimensionality*. Thus, the general function $f(\cdot)$ is approximated by a sum over simpler functions such that eq. 4.15 is replaced by:

$$y_i = \alpha + \sum_j s_j(x_{ji}) + \sum_k \sum_l s_{lki}(x_{li}, x_{ki}) + \dots + \varepsilon_i \quad (4.16)$$

where α is a constant, $s_j(\cdot)$ denotes a smooth 1D function over covariate x_j (i.e., nonlinear main effects), and the $s_{jk}(\cdot, \cdot)$ are smooth 2D functions to account for possible higher order interactions. This additive decomposition requires the additional identifiability constraint that each function must sum to zero:

$$\sum_i s_j(x_{ji}) = 0, \forall j \quad (4.17)$$

Without this constraint, a constant could be added to any one of the functions, and subtracted from another, without changing the output of the model. In other words, there would be an infinite number of equivalent models. Third, as with the generalized linear model (GLM; Nelder and Wedderburn 1972), responses are assumed to be independently drawn from a known parameterizable distribution. Most commonly, these are the exponential family (EF) distributions. Thus, the GAM may be written:

$$g(\mu_i) = \eta_i = \sum_j s_j(x_{ji}) + \sum_k \sum_l s_{lki}(x_{li}, x_{ki}), Y_i \sim EF(\mu_i, \phi) \quad (4.18)$$

Some additional notation has been introduced for convenience. Let Y_i denote the exponential family random variable of which the observed y_i are a realization. The exponential family $EF(\mu_i, \phi)$ has two parameters for the conditional mean $\mu_i = \mathbb{E}(Y_i|\eta_i)$ and variance $var(Y_i) = \phi V(\mu_i)$, where ϕ is a constant scale/dispersion parameter that is either fixed, or estimated from the data. Thus, the variance is assumed to change as a function of the mean, and the variance function $V(\cdot)$ depends on both the EF distribution, and the *link* function $g(\cdot)$. When the functions $s(\cdot)$ are estimated using linear methods, the term η is called the linear predictor. Thus, the link function controls the relationship between the mean and the linear predictor as well as between the mean and the variance. It can be used to model “non-additive” relationships on the response scale. For example, letting $g(\cdot) = \log(\cdot)$ converts an additive model, on the linear predictor scale, to a multiplicative model on the response scale. The form of the link function can either be estimated from the data or, as is more typically done, set to a known smooth (i.e., differentiable) monotonic function (e.g., log). In summary, the GAM is a GLM extended by the incorporation of smooth functions.

Given the above definition, one must select a response distribution, a link function, a way of representing the smooth functions, as well as a way of controlling their degrees of smoothness (i.e., to prevent overfitting). The latter two points are the most crucial, and a number of approaches are available. In the original GAM formulation (Hastie and Tibshirani 1990), the backfitting algorithm was introduced which allows the smooth functions to be estimated using any type of scatterplot smoother. This is an important and flexible class of models that is still under active development. However, many of the methods based around this approach do not scale well to the size of data considered in this dissertation. Therefore, this class of methods will not be considered further.

The approach explored here is based on penalized regression splines. One of the main reasons for taking this approach is the existence of a very general, stable, and user friendly software package, included in the R programming environment, called mgcv (Wood 2006, 2017). Features of the package include: automated smoothness selection, a large variety of regression splines in any number of dimensions, mixed model extensions, response distributions outside the exponential family, autoregressive terms, and a large suite of model checking and diagnostic tools. Perhaps most importantly, however, additional options for memory and speed optimizations make the methods scalable to data sizes commonly encountered in field potential experiments. These features greatly expand the range of models that can be specified and allow users to iterate rapidly during the model building process. Thus, experimentalists are free to focus on building models appropriate for the question at hand rather than recreating in-house implementations

which are often less stable and fail to promote reproducible science. In what follows, I describe the penalized regression approach employed by mgcv in more detail, before presenting an application to field potential data.

The mgcv-style GAM has the general form:

$$g(\mu_i) = \mathbf{A}_i \boldsymbol{\alpha} + \sum_j L_{ji} s_j(x_{ji}) + \sum_k \sum_l s_{lki}(x_{li}, x_{ki}) + \mathbf{Z}_i \mathbf{b}, \quad Y_i \sim EF(\mu_i, \phi \boldsymbol{\Lambda}) \quad (4.19)$$

This is similar to eq. 4.17 with some additions. \mathbf{A} is a design matrix, with associated coefficient vector $\boldsymbol{\alpha}$, for parametric terms that would be included in any typical LM or GLM. The L_{ji} terms represent known linear operators which take the smooth functions $s_j(\cdot)$ as their arguments. A simple example would be letting $L_{ji} s_j(x_{ji}) = x_{ki} s_j(x_{ji})$ which is sometimes called a *varying coefficient* model because the smooth function can be viewed as a coefficient, for the covariate x_k , that varies with respect to another covariate x_j . When x_k is a factor variable, these terms can be used to specify separate smooth functions for each level of the factor. Likewise, when x_k is coded as an ordered factor, they can be used to specify differences between smooth functions at each level of the factor with respect to a specified reference level. Another example is formed by letting $L_{ji} s_j(x_{ji}) = \int s_j(x_j) k_i(x_j) dx_j$ which is sometimes called functional/signal regression because the covariate $k_i(x_j)$ is a vector-valued function at each observation. The smooth function $s_j(x_j)$ then acts as a coefficient function similar to the varying coefficient case. The inclusion of linear operators is a feature that greatly enhances the range of models that may be specified.

The third addition in eq. 4.19 is the random effect matrix \mathbf{Z} with its associated coefficient vector \mathbf{b} . This allows for terms like random intercepts, random slopes, and even random smooth functions to be incorporated. Such random effects can be used to account for unknown factor-specific sources of variation in the data that are not assumed to be fixed properties in the population of interest. For example, in neurophysiology experiments, data are often obtained from multiple subjects, and each subject might participate in the experiment multiple times. Random effects can be used to account for aspects of the data which might be unique to a particular subject.

The last addition in eq. 4.19 is the error covariance matrix Λ which can be modified to incorporate known correlation structure between the observations. For example, with time series data, measurements taken at fixed intervals often display serial autocorrelation. The simplest structure to account for such correlation is the autoregressive $AR_\rho(1)$ error process. With such a structure, residuals at neighboring time points are assumed to have a correlation ρ such that $\varepsilon_i = \rho\varepsilon_{i-1}$. This helps relax the assumption that the data are sampled independently. Another use for Λ is the incorporation of prior weights on the observations which helps relax the assumption of a strictly fixed variance relationship. An example application in neurophysiology would be to down weight data points with known artifacts (e.g., due to animal's movement or chewing) by assuming the residuals at these points have higher variance. Such an approach has been advocated as a useful advantage of the general linear model (Litvak et al. 2013). Observation weighting is also important for certain approaches to fitting point process models (Baddeley and Turner 2000).

As noted above, the smooth functions are represented using spline bases with associated penalties that control the degree of smoothness. Thus, each of the smooth terms in eq. 4.19 can be re-expressed as:

$$s_j(x_j) = \sum_k^K \beta_{kj} b_{kj}(x_j) \quad (4.20)$$

where $b_{kj}(\cdot)$ denotes the kth-of-K basis function for covariate j , and the β coefficients are what must be learned. A large variety of splines exist, and some may be better suited to representing certain types of functions than others. In this respect, it may be worth considering whether bases exist that are particularly suited to representing the types of functions discoverable from time-frequency data. However, in this dissertation I have chosen the family of natural cubic splines since they can be set up with low computational cost, and are a natural choice for the types of penalties used in GAM's (see below).

Each of the basis functions are parameterized to enforce the identifiability constraints (discussed above), and stored in the columns a design matrix. If we let \mathbf{X}^j denote the design matrix for the jth smooth function, eq. 4.19 can be re-written in matrix notation by concatenating all of the \mathbf{X}^j , column-wise, into a single matrix \mathbf{X} :

$$g(\mu_i) = \mathbf{A}_i \boldsymbol{\alpha} + \mathbf{X}_i \boldsymbol{\beta} + \mathbf{Z}_i \mathbf{b}, \quad Y_i \sim EF(\mu_i, \phi \boldsymbol{\Lambda}) \quad (4.21)$$

In this notation, it is easier to see that the model is a large, over-parameterized GLM. All that remains is to define a way to control the complexity of the smooth functions.

The general strategy here is to choose the number of basis functions K, representing each function, to be higher than necessary. In principal, this number could be set arbitrarily high, however, there is a trade-off between flexibility and computational

efficiency. With field potential data, K in the range of 10-20 often achieves an acceptable balance. The model is then estimated according to a penalized maximum likelihood criteria:

$$\hat{\boldsymbol{\theta}} = \max_{\boldsymbol{\theta}} l(\boldsymbol{\theta}) - \sum_j \lambda_j P(\boldsymbol{\theta}_j) \quad (4.22)$$

where $\boldsymbol{\theta} = [\boldsymbol{\alpha}^T \boldsymbol{\beta}^T \mathbf{b}^T]^T$ incorporates all the coefficients in the model, $l(\boldsymbol{\theta})$ is the log-likelihood evaluated at $\boldsymbol{\theta}$, and the smooth basis-associated coefficients are penalized according to the following roughness penalty:

$$P(\boldsymbol{\theta}_j) = \int s_j''(x_j)^2 dx_j \quad (4.23)$$

where $s_j''(x_j)^2$ is the squared second derivative of the j^{th} smooth function. The second derivative is taken as a measure of the function's curvature, and so the penalty is on the total amount of curvature integrated across the function. As the linear part of $s_j(x_j)$ does not contribute to the second derivative, it is left un-penalized. Thus, $P(\boldsymbol{\theta}_j)$ can also be thought of as a penalty on the deviations away from linearity. In fact, it is possible to rewrite the basis functions in an equivalent representation that is orthogonal to x_j . In this case, x_j is included as an un-penalized column in the design matrix. The remaining transformed basis functions can then be viewed as random effects with coefficients that are assumed to be normally distributed with zero-mean and a variance controlled by λ_j .

In the Bayesian view, this is equivalent to assuming an improper Gaussian prior on the coefficients. Similarly, as the penalty is quadratic in the coefficients, it can also be viewed as a form of ridge regression. In this view, the above penalty can be seen to

achieve a better bias-variance tradeoff compared to the typical ridge regression in which the penalty is on $\sum_k \Theta_{kj}^2$.

The strengths of each of the penalties are determined by the λ_j , which are called smoothing parameters. Lower values of λ_j result in more complicated functions, while higher values result in smoother functions. Choosing appropriate values for the smoothing parameters is the major computational challenge with GAMs. The package mgcv offers a number of solutions which are implemented by a variety of penalized iteratively re-weighted least squares (PIRLS) algorithms. Some of the methods utilize cross-validation-based criteria, however, the default is based on a restricted maximum likelihood (REML) score. The idea behind REML is related to the Bayesian view of the penalty discussed above (sec. 6.2.6 Wood 2017). Briefly, one can imagine simulating random functions by randomly sampling coefficients from the prior implied by the penalty. For too small values of λ_j , these random functions will have high variance and venture out far from the data, thereby decreasing their mean likelihood score. Conversely, too high values of λ_j result in random functions with small variance that are unable to reach the data. With appropriate values of λ_j , a portion of the random functions will, by chance, fall close to the data and result in a higher mean likelihood score. This approach to smoothing parameter selection provides an effective, data-driven solution that reduces experimenter bias and guards against overfitting.

4.4 – Application to brain rhythms

With the essential concepts of time-frequency analysis and the GAM framework in place, a selection of the ideas from the previous sections will now be demonstrated on field potential data recorded from area CA1 str. pyramidale of the mouse hippocampus (see sec. 2.3 for Methods). The purpose of these demonstrations will be to give a sense of the range of model types available, and to highlight the strengths and limitations of the GAM framework for modeling time-frequency data. To keep the examples relatively simple, I will focus on a reduced dataset, consisting of a single recording from a single mouse. The recording corresponds to one day from the experiment in Chapter 2, which consisted of three ten minute sessions in which the mouse ran unidirectionally around a circular track for food reward.

Figure 4.3A shows a representative two seconds of the recording along with its corresponding CMWT with ridges overlaid to visualize the instantaneous frequency content. The CMWT surface appears complicated, but some distinctive features are evident. There is a prominent ~8-9 Hz theta oscillation visible in the recording which has an associated ridge in the CMWT that is stable across the entire two seconds. There is also a higher frequency ridge (~16-18 Hz) that tracks theta and likely corresponds to a harmonic induced by the non-sinusoidal shape of the theta waveform. The shape of the theta waveform appears to change from cycle-to-cycle and is characterized by varying degrees of asymmetry and skewness. In other words, the rising phase is steeper, and the troughs sharper, compared to a pure sinusoid, respectively. Other features evident in the recording are the high frequency gamma oscillations (>20 Hz) which are nested within, and tend to concentrate around, the peaks and falling phases of the theta cycles.

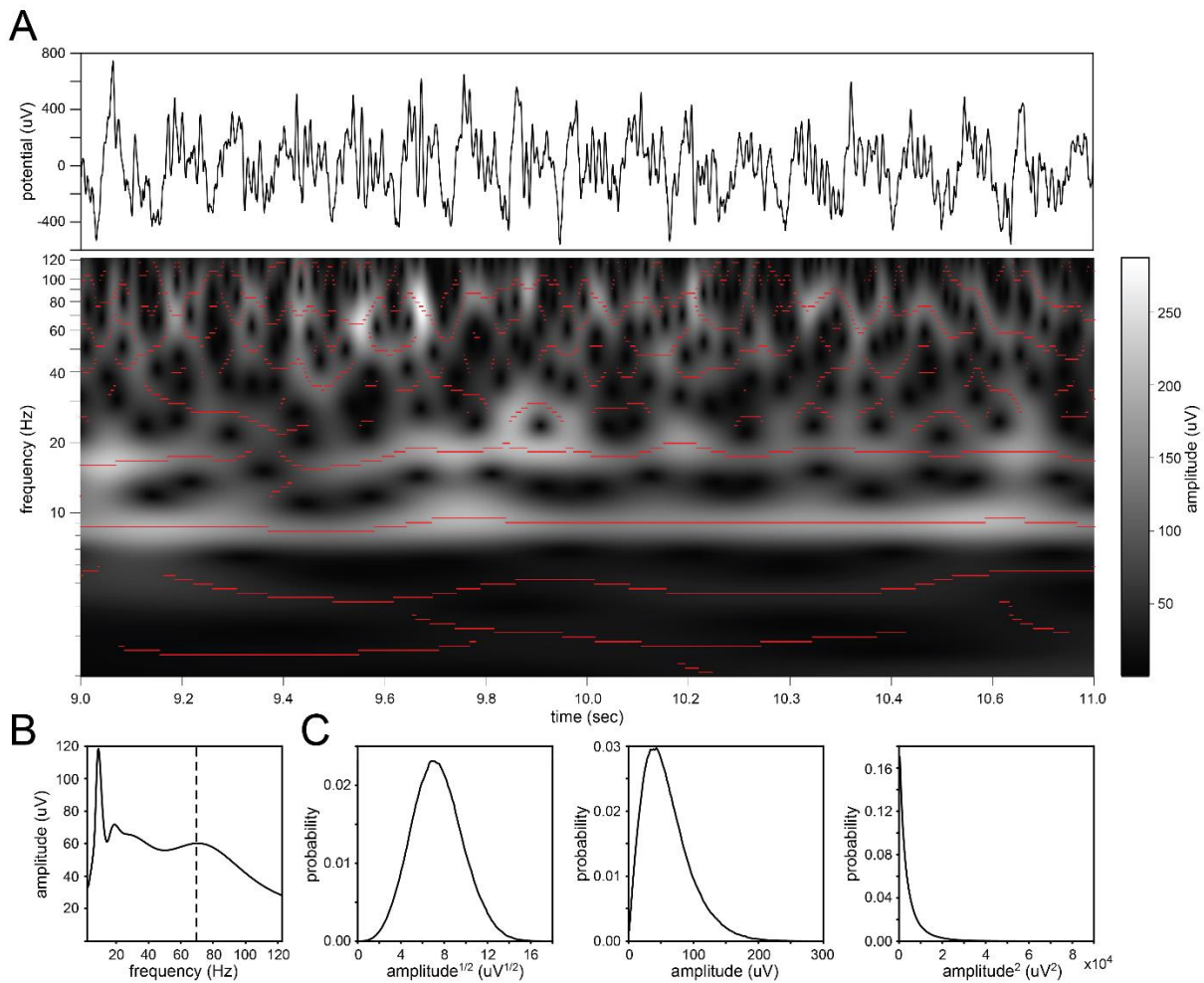


Figure 4.3. CMWT of mouse CA1 field potential. A) An example two seconds of LFP (top) recorded from the CA1 pyramidal layer of mouse hippocampus, and its corresponding CMWT (bottom) with ridges overlaid in red. The CWMT was computed using the area scaling with width parameter $w_0 = 6$. Note, the frequency axis is on a logarithmic scale to aid visualization. **B)** The mean amplitude spectrum taken over the entire 30 minutes of recording (left). **C)** Distribution of the square root amplitude (left), amplitude (middle), and amplitude squared (right) of the component centered at 70 Hz denoted by the dotted line in B.

Compared to the theta-related ridges, the gamma-frequency ridges in the CWMT are more transient and variable in frequency.

Now consider the goal of constructing a predictive model for the CMWT surface. One of the simplest models would be the intercept-only model which is estimated by averaging the CMWT across all time points for each frequency. This produces the marginal amplitude spectrum which provides information about which frequencies are most prominent on average. In the example here, separate peaks are evident at frequencies corresponding to theta (~9 Hz), its putative harmonic (~18 Hz), slow gamma (~25-30 Hz) and fast gamma (~70 Hz) (Figure 4.3B). A more complicated model might predict how the amplitude spectrum varies based on predictor variables of interest. As many such models are fit on a frequency-by-frequency basis, I will proceed by focusing on a single frequency component, centered at 70 Hz, in the following examples.

An important aspect of any parametric modeling approach is selecting the appropriate response distribution which depends strongly on the type of response variable (e.g., continuous, discrete, etc.), and any transformations applied to it (e.g., logarithm, square root, etc.). Figure 4.3C shows the distributions of the amplitude, power (i.e., amplitude²), as well as the square root amplitude of the 70 Hz component. All amplitude quantities are strictly positive, and squaring/square rooting can exaggerate/alleviate rightward skew, respectively. Transformations may, thus, be used to make the data more-or-less consistent with a particular distributional assumption. For example, it has been recommended to take the square root or log of power in order to make it more normally distributed (Kiebel et al. 2005). From Figure 4.3C, however, the square root of

amplitude (i.e., not power) appears most normally distributed. Others have proposed the use of nonparametric transformations which attempt to map any arbitrary distribution into the Normal distribution (van Albada and Robinson 2007). A similar such approach was used in Chapter 2. Not all transformations, however, are equally interpretable in physical terms. Furthermore, the inverse transform of the mean of the transformed data is not equal to the mean of the original data (e.g., $e^{\mathbb{E}[\log(Y)]} \neq \mathbb{E}[Y]$), and this inequality may introduce bias into effect estimates. Thus, it may be desirable to assume a non-Normal response in order to model amplitude or power on their natural scales. The Gamma distribution, with a log link function, was recently proposed as a viable candidate for this purpose (Kramer and Eden 2013). The Gamma distribution is an exponential family distribution that is commonly used to model strictly positive, continuous-valued data with a variance that increases with the square of the mean (i.e., $\text{var}(Y_i) = \phi\mu_i^2$). Thus, by assuming a constant coefficient of variation, rather than a constant variance, it is able to model a form of heteroscedasticity. It can be further motivated by noting that, assuming the original field potential values are approximately normally distributed, power estimates are expected to follow a χ^2 distribution with two degrees of freedom (Torrence and Compo 1998; Kiebel et al. 2005), which is a specific instance of the Gamma distribution. It can also be used to handle normally and exponentially distributed data.

All of these response distribution options are available, and can be compared, within the GAM framework. To demonstrate this, I fit a series of five simple models including running speed and theta phase as predictors, and assuming different response distributions/transformations:

$$\mu_i = s(speed_i) + s(phase_i), \quad y_i \sim Normal(\mu_i, \sigma^2) \quad (4.24)$$

$$\mu_i = s(speed_i) + s(phase_i), \quad \log(y_i) \sim Normal(\mu_i, \sigma^2) \quad (4.25)$$

$$\mu_i = s(speed_i) + s(phase_i), \quad y_i^{1/2} \sim Normal(\mu_i, \sigma^2) \quad (4.26)$$

$$\log(\mu_i) = s(speed_i) + s(phase_i), \quad y_i \sim Gamma(\mu_i, \phi) \quad (4.27)$$

$$\log(\mu_i) = s(speed_i) + s(phase_i), \quad y_i^2 \sim Gamma(\mu_i, \phi) \quad (4.28)$$

where y_i is amplitude, and the $s(\cdot)$ specify smooth functions as described in the previous section. The consistency of the distributional assumptions of each of the models was compared using QQ-plots (Figure 4.4A). QQ-plots test distributional assumptions by comparing the quantiles of the observed residuals to the quantiles of their distribution expected under the assumptions of the model. There are many types of QQ-plots which differ in the ways they define the residuals and/or their expected distribution. Here, I used a simulation-based approach (Hartig 2017) which repeatedly samples pseudo-data from the fitted models to estimate the assumed distribution at each of the observations. The residual, for a particular observation, was then defined as the proportion of the simulated data smaller than the observed data value. Such residuals have values between zero and one, and an expected uniform distribution. The deviations from the diagonal of the plot describe how the data fail to meet the distributional assumptions of the model. For the Normal::amplitude model (eq. 4.24), there is evidence that the data was more skewed to the right than assumed (Figure 4.4A). The log transform is often used to correct for the rightward skew; however, the Normal::log(amplitude) model (eq. 4.25) displayed evidence of overcorrection. In other words, the data was more skewed to the left than assumed by the model. The less extreme square root transform, Normal::amplitude^{1/2} (eq.

4.26), provided a compromise, and its QQ-plot fell very close to the diagonal. Compared to the Normal::amplitude model, the Gamma::amplitude model (eq. 4.27) was more consistent with the data, but expected more rightward skew than was observed. As excess rightward skew is corrected by the square root transform, excess leftward skew can be corrected by squaring the data. Thus, the Gamma::amplitude² model (eq. 4.28) also fell very close to the diagonal. Overall, these results demonstrate that assuming a Gamma distribution is likely better for modeling the data on the original response scale (i.e., amplitude or power), while the Normal distribution is most consistent with the square root of amplitude.

As the Normal::amplitude^{1/2} and Gamma:amplitude² models performed best in terms of QQ-plots (Figure 4.4A), their estimated effects for running speed and theta phase were selected for visualization in Figure 4.4B. The Normal::amplitude^{1/2} model corresponds to an additive model on the square root amplitude scale, while the Gamma:amplitude², with log link function, corresponds to a multiplicative model on the power scale. The units of the square root scale are less intuitive, which can be compounded by differences in baseline mean/dispersion between different datasets (i.e., subjects, days, experimental conditions, etc.). For this reason, it is common to perform an additional baseline correction/normalization step to control for possible confounds. In this example, the square root amplitudes were z-scored. Thus, the additive contributions of running speed and theta phase are reported in units of standard deviations, and are centered on zero. With the Gamma distribution, the choice of normalization is less of a concern, as the multiplicative contributions of each of terms are reported in units of

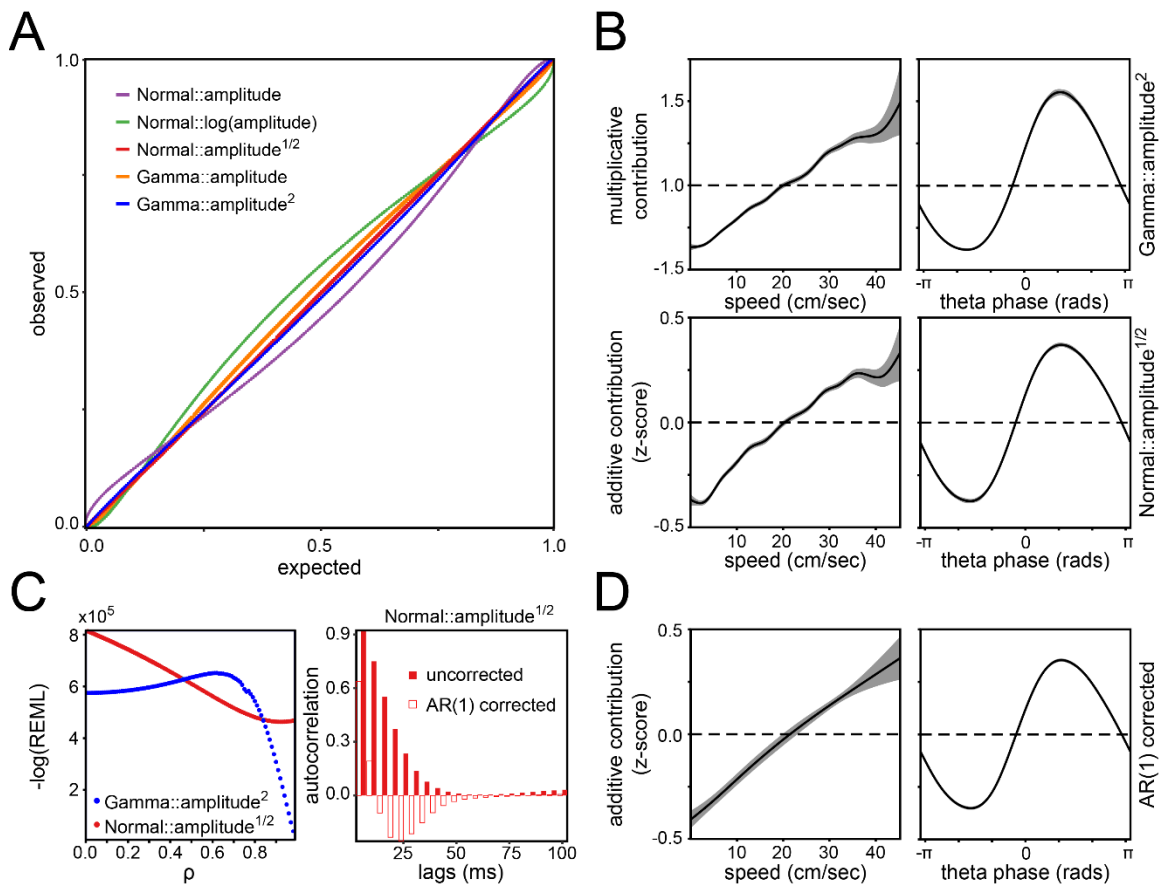


Figure 4.4. Comparison of response distributions and handling of autocorrelation.

A) QQ plots for each of the five models (eqs. 4.24-28). **B)** Contributions of running speed (left) and theta phase (right) for the Gamma::amplitude² model (top) and the Normal::amplitude^{1/2} model (bottom). **C)** Left panel shows the negative log(REML) scores for the Gamma::amplitude² model (blue), and the Normal::amplitude^{1/2} model (red), evaluated over 100 values of AR(1) parameter ρ . Right panel shows the uncorrected residual autocorrelation function for the Normal::amplitude^{1/2} model fit without an AR(1) term (filled bars), and for the same model with AR(1) correction using the optimal value of ρ (empty bars). **D)** Same as B, but for the AR(1)-corrected Normal::amplitude^{1/2} model.

multiplicative gain centered on one. In spite of these differences, the effects estimated by the two models appear very similar (Figure 4.4B), and it is unlikely that different conclusions would be drawn between them. Both demonstrate that the amplitude of the 70 Hz component is largest at high running speeds and on the descending phase of theta (i.e., $0\text{-}\pi$ rad).

A point of concern, however, is that the confidence intervals appear narrow, and the running speed contributions contain some wiggles which could be indicative of undersmoothing/overfitting. A common cause for these issues in time series data is autocorrelation, which violates the assumption that the data were sampled independently. Indeed, the CMWT displays a very stereotyped form of autocorrelation (eq. 4.10) that depends on the time-frequency resolution parameter settings (eq. 4.2). In principle, the GAM framework implemented by mgcv is able to incorporate a large variety of error correlation structures by estimating the model as a large, overparameterized, generalized linear mixed model using the R package lme for estimation. In practice, however, this option does not scale to the size of data considered here, and we are limited to the simpler $\text{AR}_\rho(1)$ structure described in the previous section. The $\text{AR}_\rho(1)$ has a parameter ρ which determines the strength of the correlation between neighboring residuals. The value of this parameter can be determined by fitting a sequence of models with different values of ρ , and choosing the value that minimizes the negative log(REML) score (Wood et al. 2015). Figure 4.4C shows the result of performing such a search across 100 values of ρ for the `Normal::amplitude1/2` and `Gamma::amplitude2` models. For the `Normal::amplitude1/2` model, a minimum negative log(REML) score was found at $\rho =$

0.92. Typically, this value turns out to be very close to the lag-1 correlation between the residuals of the corresponding model fit without an $AR_p(1)$ term. In contrast, the situation for the Gamma::amplitude² model is more troublesome as no minima were discovered. Figure 4.4C (left) shows that incorporating the $AR_p(1)$ term increases the negative log(REML) score at values of ρ approaching $\sim 0.6\text{-}0.7$, beyond which the score drops steeply, not reaching a minimum until ρ approaches one. Setting ρ to too high a value can result in highly biased coefficient estimates for the remaining terms in the model, and can even cause the PIRLS algorithm to fail. Thus, selecting ρ with the Gamma distribution, and other non-Normal response distributions, is more challenging. Methods to handle these cases have been discussed elsewhere (Grunwald et al. 1995).

I proceed with the Normal::amplitude^{1/2} model in Figure 4.4C (right) which shows residual autocorrelation functions of the model fit with, and without, the $AR_p(1)$ correction. Even in the Normal response case, the $AR_p(1)$ correction does not fully remove the lag-1 autocorrelation, and negative correlations are induced at larger lags (>10 ms). This is clearly not perfect, which would not be expected given that the CMWT is not an $AR_p(1)$ process. Still, the $AR_p(1)$ assumption is likely more reasonable than the independence assumption, and incorporating the $AR_p(1)$ term can help to prevent overfitting. Figure 4.4D shows the estimated contributions of running speed and theta phase with the $AR_p(1)$ correction. The running speed effect was made more linear, and the confidence intervals expanded slightly. Both models explain the data equally well ($R^2_{adj}=0.108$ for both), so the $AR_p(1)$ model would be preferred since it used fewer degrees of freedom (17.86 df vs. 25.82 df).

Up to this point, we have considered a relatively simple model consisting of two terms: running speed and theta phase. However, the model can easily be extended to incorporate higher order interactions and to perform additional controls. In recent years, the topic of cross-frequency phase-amplitude coupling (CFC) has received considerable interest, and a number of reviews have been written discussing some of the common pitfalls in these analyses (Aru et al. 2015; Hyafil et al. 2015). One possible pitfall is that changes in CFC observed across conditions might often be explained by changes in power across conditions which affect the signal-to-noise ratio of the phase estimates. For example, the increase in theta phase-gamma power coupling at higher running speeds may be due to mere increases in theta power, as opposed to “genuine” cross-frequency correlations per se. Thus, matching data across conditions using proper stratification-based techniques has been advocated (Schoffelen et al. 2005; Tort et al. 2009; Aru et al. 2015). The GAM framework offers another approach.

Consider the following extension to the Normal:amplitude^{1/2} model (eq. 4.26):

$$\mu_i = s(speed_i) + s(theta\ phase_i) + s(theta\ amplitude_i) + ti(theta\ phase_i, speed_i) + \\ ti(theta\ phase_i, theta\ amplitude_i), \quad y_i^{1/2} \sim Normal[\mu_i, \sigma^2 AR_\rho(1)] \quad (4.29)$$

This can be considered a functional ANOVA-type model with the 1D smooth functions $s(\cdot)$ representing main effects, and the 2D smooth functions $ti(\cdot, \cdot)$ representing tensor interactions. In general, smooth 2D functions are represented using 2D basis functions which can be created by taking tensor products of between the 1D marginal bases. For example, the term $ti(theta\ phase_i, speed_i)$ is constructed by taking the product of the cyclic cubic spline bases for theta phase with the regular cubic spline bases for running

speed. Separate smoothing parameters (i.e., λ from eq. 4.22) can be estimated for each dimension, allowing for anisotropic effects. Additional identifiability constraints can also be enforced to orthogonalize the interactions with respect to the main effects (Wood 2017 sec. 5.6.3).

Figure 4.5 shows the additive contributions for each of the terms in the functional ANOVA model (eq. 4.29). The running speed and theta phase contributions are similar to those in the previous examples, and the main effect of theta amplitude is relatively weak by comparison. The tensor interaction terms must be interpreted with respect to their combined influence with the main effects. Because the theta phase contribution is most positive on the descending phase of theta ($\sim 0-\pi$ rad), and the speed-phase interaction contribution is positive in this phase range at higher running speeds, its effect can be interpreted as an increase in CFC with running speed. The theta amplitude-theta phase interaction displays a similar effect and can be interpreted similarly. One noticeable difference, however, is that the positive contribution of the running speed interaction appears to be shifted closer to the peak (0 rad) at higher running speeds. This could correspond to a shift, or increased asymmetry, of the phase amplitude distribution at

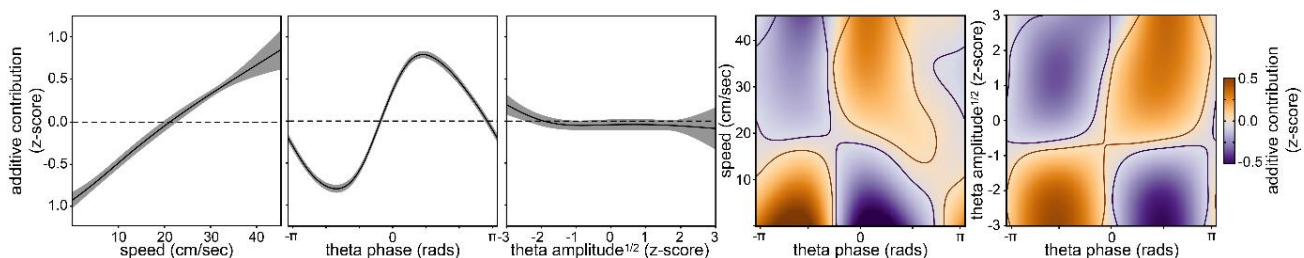


Figure 4.5. Additive contributions of running speed, theta phase, theta amplitude, the running speed-theta phase interaction, and the theta amplitude-theta phase interaction (left-to-right, respectively).

higher running speeds. Such an effect may be explained by the increased asymmetry of the theta waveform at higher running speeds (Sheremet et al. 2016). The model can be used to further investigate these hypotheses by generating predictions about the expected phase-amplitude distribution at any point in the covariate space. If one is not interested in the full shape of the distribution, lower dimensional summary statistics, such as the MAC index used in Chapter 3, may be computed from the predictions to further simplify interpretation. Lastly, if there is reason to suspect the additive decomposition into main effects and interactions is unrealistic, and sufficient data is available, one could specify a model consisting of a single 3D smooth function. Thus, the GAM framework affords the possibility to rapidly transition between models without the need to implement a new framework at each transition.

4.5 – Towards spectro-temporal point processes

One of the potential drawbacks of the GAM framework, as introduced by the previous section, is the difficulty of incorporating autoregressive elements in a scalable manner. While incorporating an $AR_p(1)$ term can increase robustness against overfitting and produce more conservative confidence estimates, integration with non-normal response distributions is less straightforward. Furthermore, the CMWT is not well described as $AR_p(1)$. Thus, while the $AR_p(1)$ may be a convenient corrective tool, it provides an overly simplistic description of the history-dependence of the data-generating process. Moreover, much of the autocorrelation can be attributed to the redundant nature of the CMWT and may not be directly related to the signal itself.

A strategy for dealing with this redundancy might be to choose sparse, less redundant, features from the CMWT for response variables instead of the continuous amplitude envelope. Especially for frequency components in the gamma range and higher, continuous amplitude envelope models are not particularly in line with the way researchers describe brain rhythm dynamics. Gamma, for example, is usually described in terms of transient events which occur stochastically at certain times and with varying intensities. For this reason, it has been suggested that transient field potential patterns be modeled as event-based processes (Dvorak and Fenton 2014; Brockmeier and Príncipe 2016).

Such event-based processes could take advantage of the existing point process theory developed for spike trains. One of the most popular point process-based frameworks for modeling spike train data is the conditional Poisson GLM. As the GAM is a type of GLM, a variant of the conditional Poisson GLM can be expressed within this framework as:

$$\log(\mu_i) = \mathbf{A}_i\boldsymbol{\alpha} + \int h(t_{lag}) y_{hist,i}(t_{lag}) dt_{lag} + \sum_j s_j(x_j), Y_i \sim \text{Poisson}(\Delta\mu_i) \quad (4.30)$$

The only new element here is the integral term in the middle which takes advantage of the functional regression form of the linear operator notation introduced in eq. 4.19. The $y_{hist,i}(t_{lag})$ term is a vector-valued covariate representing the spike history at each time. Thus, t_{lag} defines the temporal lag domain of the spike history window, and $h(t_{lag})$ is a smooth coefficient function which controls the contributions of past spikes, depending on their lags, to the current conditional intensity (i.e., spike rate) μ_i , with expected spike count $\Delta\mu_i$ for bin size Δ . In this model, spikes are assumed to be sampled from an

inhomogeneous Poisson distribution, and the log link is often chosen to make the contributions multiplicative on the conditional intensity response scale.

Now consider what features of the CMWT can be modeled by the above point process. One candidate might be the ridges. A difficulty with this option is that ridges have a temporal duration which depends, in potentially complicated ways, on their frequency variance. In other words, while ridges are sparse in frequency, they are not sparse in time. This motivates consideration of an orthogonal concept to ridges: wavelet transform modulus maxima lines (WTMMs). As ridges are defined as the local frequency maxima at each time, the WTMMs are defined as the local time maxima at each frequency. The WTMMs extend from high-to-low frequencies, and some lines terminate at lower frequencies than others. In the time-frequency analysis literature, WTMMs have been used to reconstruct nonharmonic signals, to separate harmonic from nonharmonic components, to detect signal singularities (i.e., discontinuities), and to quantify temporal self-similarity (Mallat 2008; Addison 2017). To my knowledge, however, these concepts have been sparsely applied in neuroscience.

Figure 4.6A shows the same recording and CMWT as Figure 4.3A, but with the WTMMs overlaid, and Figure 4.6B shows a frequency slice corresponding to the frequency band centered at 70 Hz. Within a frequency band, the WTMMs are a series of spikes of varying amplitudes. It is therefore somewhat unnatural to directly apply the conditional Poisson model. One might ignore the amplitude information, and choose to only model the event times; however, this seems unsatisfying. A Gamma process is also not an option as the WTMM trains contain mostly zeros.

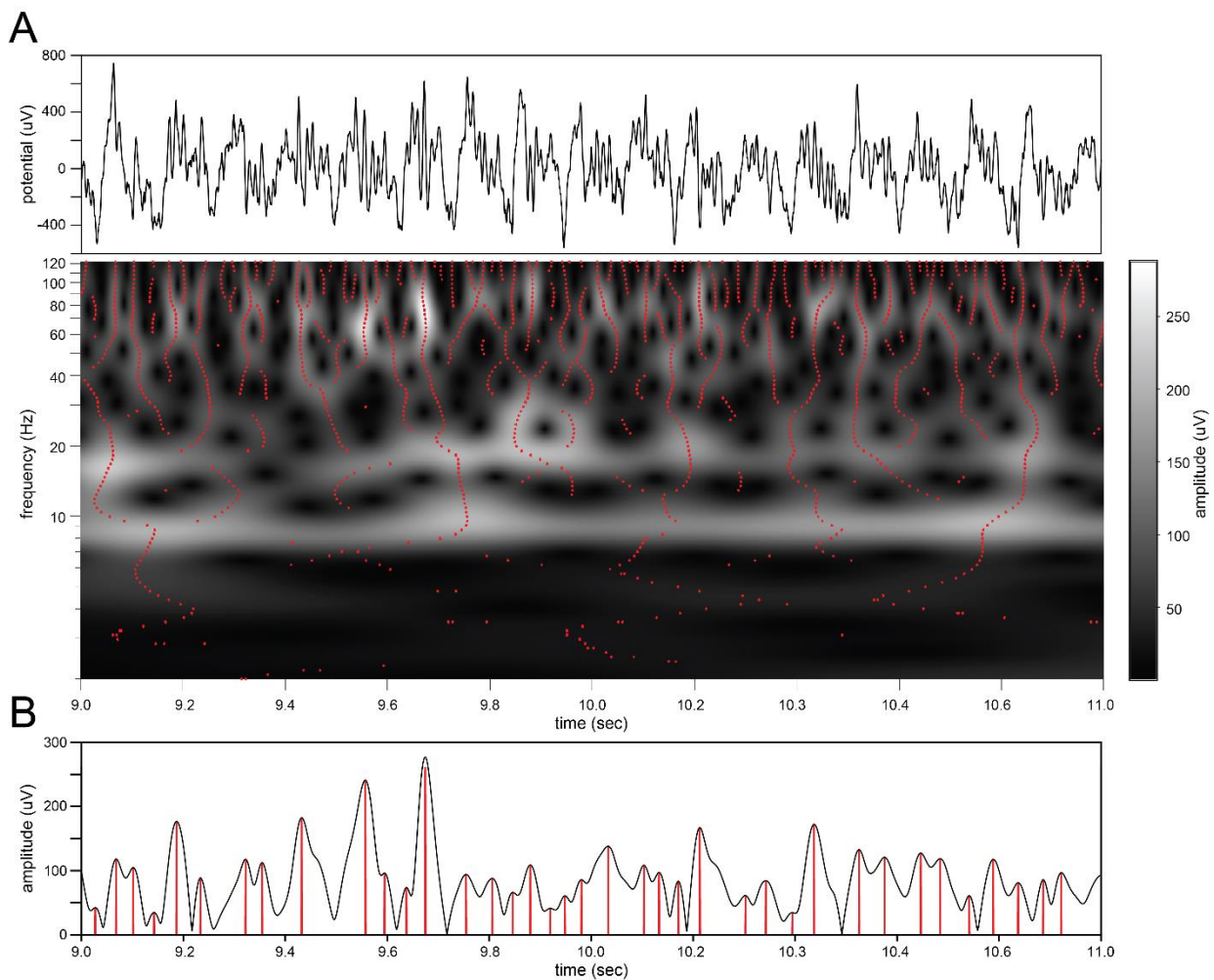


Figure 4.6. Wavelet transform modulus maxima lines. **A)** Same example LFP recording (top), and CMWT (bottom) from figure 4.3, but with WTMM lines overlaid in red. **B)** Amplitude envelope (black), and WTMM spike train (red) for the component centered at 70 Hz.

A somewhat simple alternative is to assume a Tweedie distribution. The Tweedie distribution is a three parameter distribution which is conditionally in the exponential family depending on the value of a parameter, p (Tweedie 1984; Jorgensen 1987). It is characterized by its variance function:

$$\text{var}(Y) = V(\mu) = \phi\mu^p \quad (4.31)$$

The interesting feature is that, as the value of p changes, the Tweedie distribution transitions continuously between common exponential family distributions. The relevant range for the current setting is p between one and two. For p equal to one, the Tweedie distribution is Poisson, while for p equal to two, it is a Gamma distribution. Figure 4.7A shows the effect of varying p from one to two for a fixed mean μ and dispersion ϕ . For p close to one, the distribution is both continuous and multimodal. As p approaches two, it resembles a Gamma distribution with a point mass located at zero. A Tweedie distributed random variable can be interpreted as a sum of N independent Gamma random variables, where N is sampled from a Poisson distribution. Thus, the point mass at zero corresponds to observations with N equal to zero. Tweedie models can be used to predict the following quantities (Yunus et al. 2017):

$$\lambda_i = \frac{\mu_i^{2-p}}{\phi(2-p)} \quad (4.32)$$

$$\gamma_i = \phi(p-2)\mu_i^{p-1} \quad (4.33)$$

$$P(Y_i = 0) = e^{-\lambda_i} \quad (4.34)$$

where μ_i is the mean amplitude, λ_i is the mean number of events (i.e., the mean of the Poisson distribution for N), γ_i is the mean amplitude per event, and $P(Y_i = 0)$ is the probability of not observing an event.

I now consider conditional Tweedie GAMs of the following form:

$$\log(\mu_i) = \mathbf{A}_i\boldsymbol{\alpha} + \int h(t_{lag}) I[y_{hist,i}(t_{lag})] dt_{lag} + \sum_j s_j(x_j), Y_i \sim \text{Tweedie}_p(\mu_i, \phi) \quad (4.35)$$

The model is similar to eq. 4.30, except the response distribution is Tweedie instead of Poisson, and the $I[\cdot]$ in the integral is an indicator function which is equal to one wherever a WTMM spike is observed. This allows the history function to be interpreted as it would be in the conditional Poisson model (eq. 4.30). For all models, the WTMM spike trains of the 70 Hz component of the CMWT were binned into 5 ms bins, the largest lag in the history term was set to 500 ms, and the history function was represented using 30 natural cubic spline basis functions.

To gain a preliminary understanding of the expected form of the history function for an arbitrary signal, a Gaussian white noise signal was generated with the same length and variance as the field potential recording. A history-only conditional Tweedie GAM was then fit to its 70 Hz component WTMM train. Figure 4.7B shows the multiplicative contribution of the history function for the white noise model. A refractory period is evident for lags up to ~50-60 ms. This is, perhaps, unsurprising as the correlation structure of the CMWT (eq. 4.10) limits the rate at which WTMM spikes can occur in a given frequency band. Somewhat more surprising, however, is the excitable region observed at intermediate lags (~60-120 ms). This result goes against a recent suggestion that spectrogram extrema are distributed according to a determinantal point process,

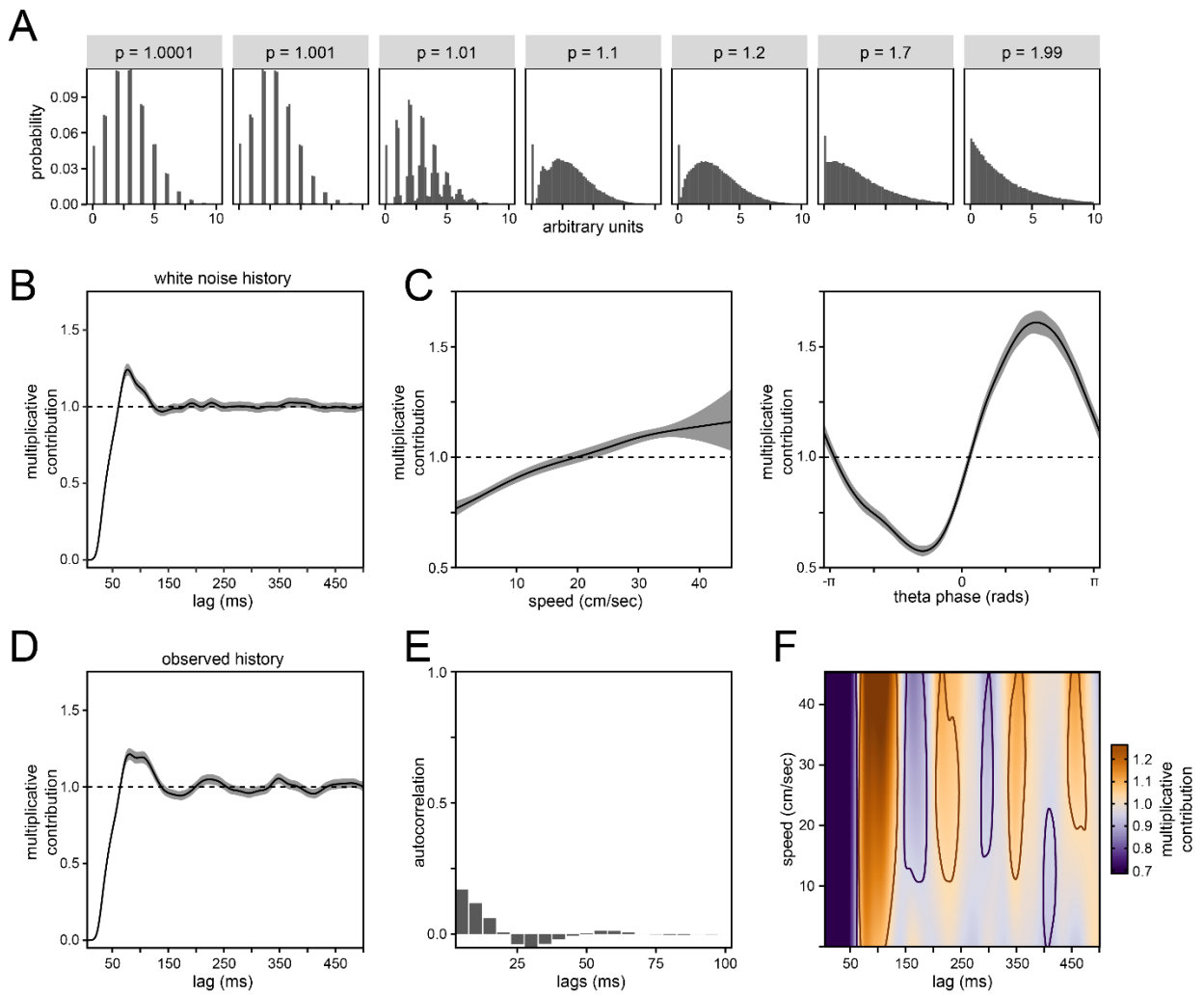


Figure 4.7. The conditional Tweedie GAM. **A)** Simulated Tweedie distribution with fixed mean $\mu = 3$, dispersion $\phi = 1$, and varying p between one and two. **B)** History function for the conditional Tweedie GAM fit to the 70 Hz WTMM train of the white noise signal. **C)** Multiplicative contributions of running speed (left) and theta phase (right) for the conditional Tweedie GAM fit to the 70 Hz WTMM train of the LFP signal. **D)** History function for the same model in C. **E)** Residual autocorrelation function corresponding to the model in C and D. **F)** Running speed-history interaction function for the model corresponding to eq. 4.36 (see text).

which would predict repulsive (i.e., inhibitory) interactions at all lags (Flandrin 2017). It is consistent, however, with another recent theoretical work which demonstrated that the spectrogram zeros (i.e., 2D local minima) are approximately distributed according to the zeros of a Gaussian analytic function, which predicts an excitable region at intermediate lags (Bardenet et al. 2017). Such an excitable region, therefore, appears to be a basic property of the CMWT, and other equivalent classes of time-frequency representations.

I then fit a similar model to the 70 Hz component of the field potential data from the previous section, including smooth functions for WTMM spike history, running speed, and theta phase. Figure 4.7C shows the multiplicative contributions of running speed and theta phase, while Figure 4.7D shows the estimated history function. The effects of running speed and theta phase were similar to those presented in the previous section with the Gamma response model (Figure 4.4B). However, the confidence intervals for the Tweedie model were more conservative in comparison. At short lags (<60 ms), the refractory period with real data was similar to that observed in the white noise model. However, at longer lags (>100 ms), a clear theta rhythmicity was observed in the real data. The Tweedie model for the WTMM train also displayed less residual autocorrelation compared to the Normal::amplitude^{1/2} model (Figure 4.7E vs Figure 4.4C). It should be noted that the residual autocorrelation evident in Figure 4.7E may be further reduced by selecting the maximal lag in the history term more carefully, or by representing the history term with adaptive bases which smooth more at longer lags. A more specialized point process residual analysis, based on the time rescaling theorem (Brown et al. 2002; Truccolo et al. 2005), may also provide further insight.

The functional ANOVA model, presented in Figure 4.5, showed that theta phase-gamma amplitude correlations increase with running speed. We might expect the form of the history function to vary with running speed as well. Such interactions with vector-values covariates can be handled. As a final demonstration, I fit a model of the form:

$$\log(\mu_i) = \int h(speed_i, t_{lag}) I[y_{hist,i}(t_{lag})] dt_{lag}, \quad Y_i \sim Tweedie_p(\mu_i, \phi) \quad (4.36)$$

where the history function $h(speed_i, t_{lag})$ is now a 2D function of the lags and of running speed. Figure 4.7F displays the estimated surface which demonstrates that the theta rhythmicity of the history function becomes stronger at higher running speeds. This provides a complimentary view of cross-frequency phase-amplitude correlations which does not require estimating the phase of the lower frequency oscillation.

4.6 – Discussion

The goal of this chapter was to provide an overview of the time-frequency analysis and statistical modeling frameworks used in this dissertation. These topics are rarely presented side-by-side. The hope is that, by presenting them alongside one another, readers will recognize connections between the topics, and be inspired to create novel analyses that might be handled within the GAM framework.

The GAM framework was presented at a qualitative level, and focused instead on providing practical examples of its application to modeling gamma amplitude dynamics. In doing so, many relevant details may have been overlooked. For example, topics like random effects, model comparison, and hypothesis testing were only briefly mentioned, or not covered at all. I, therefore, direct readers to a number of excellent GAM/mgcv

tutorials that have been published in recent years, and which cover these topics in detail (van Rij et al. 2016; Winter and Wieling 2016; Baayen et al. 2017, 2018; Sóskuthy 2017). In addition, Simon Wood’s book is an invaluable resource, both as a reference for mgcv and as an overview of the GAM framework in general (Wood 2006, 2017).

While much emphasis was placed on estimating amplitude and phase-amplitude dynamics in a single channel, I would like to stress that the methods discussed are also relevant for modeling other time-frequency variables as well. Time-frequency ridges, in particular, deserve further attention as they are indicators of the instantaneous frequency content of the signal. Thus, they are thought to be important for controlling spike timing and for coordinating large-scale network patterns (Varela et al. 2001; Cohen 2014), and represent an elegant means for studying large scale phase synchronization between multiple brain areas (Rudrauf et al. 2006; Le Van Quyen and Bragin 2007). While statistical models for ridges are mostly lacking, a recent proposal based on dynamical Bayesian inference of phase coupling functions represents a step in this direction (Stankovski et al. 2017). A similar approach is feasible under the GAM framework.

In another recent work, a non-linear time-varying autoregressive model was used to detect and quantify cross-frequency phase-amplitude correlations (Dupré la Tour et al. 2017). An advantage of the autoregressive approach, compared to wavelet methods, is it allows the entire spectrum to be modeled simultaneously, as opposed to on a frequency-by-frequency basis. In this study, they also proposed a way to estimate the optimal time delay between the slow frequency phase signal, and the fast frequency amplitude signal. This creates a directed measure which can be used to study the extent to which

phase/amplitude signals in different brain areas precede/follow one another. Such a measure can also be estimated under the GAM framework by utilizing the same linear operator functionality used to estimate the history functions in section 4.4. For example, in the same way that the history function was modeled as an interaction between running speed and temporal lag (eq. 4.36; Figure 4.7F), phase correlation delays could be estimated as an interaction between the lagged phases and their respective lags. For a more in depth discussion of the application of GAM's to distributed lag-type models, see (Gasparrini et al. 2017).

Another goal of the chapter was to briefly introduce the concept of a time-frequency point process, and a simple example was implemented to further demonstrate the convenience and flexibility of the GAM framework. Other approaches could have been taken. For example, the WTMM trains could be modeled as a marked point process (Daley and Vere-Jones 2003), or alternatively, using a Gamma hurdle model. In the Gamma hurdle approach, two separate models are estimated to separately model the probability of event occurrence, and the amplitude given that an event has occurred. I direct readers to a relevant discussion of the tradeoffs between the Tweedie and Gamma hurdle approaches (Xacur and Garrido 2015).

An apparent limitation of the conditional Tweedie and GAM models, as presented here, is that the frequencies are modeled one-by-one rather than jointly as a single unit. This is not a true “time-frequency” approach. Extensions to the GAM, such as vector generalized additive models (Yee 2015), enable modeling vector-valued responses. Even within the GAM framework presented here, however, a large class of vector-valued

response models can be implemented. An R package, called refund, has recently been developed to facilitate application of these, and many other, functional data analysis-type models using mgcv as an engine (Greven and Scheipl 2017).

Yet another way to get around the frequency-by-frequency limitation, might be to choose a response feature more amenable to point process interpretation than the ridges or WTMM lines. Much of the trouble with modeling either of these features, in the 2D plane, stems from the fact that they are lines and not points. The CMWT spectrogram contains features that *are* points: the zeros. The zeros are the local minima in the time-frequency plane, and their locations in the plane determine, to a large extent, the values of the spectrogram at all other locations (Gardner and Magnasco 2006; Gröchenig 2013; Flandrin 2015, 2016; Bardenet et al. 2017). Thus, and perhaps counter to intuition, it may be useful to model the silent parts of the signal rather than the loud parts. Such a model might treat the zeros as a special type of spatial point process which could be fit using conditional Poisson approaches amenable to the GAM framework (Baddeley and Turner 2000; Baddeley et al. 2015).

Clearly, there is a long road ahead to develop more solid theoretical foundations for the types of spectro-temporal point processes alluded to here. However, advancing in this direction will enable field potential researchers to benefit from the large body of work that has developed around similar models for neural spiking data (Truccolo 2016; Meyer et al. 2017). It may be important to frame multiple types of neural data into a common statistical framework. Doing so may enable the possibility to model neural data

across multiple scales, and will likely encourage cross-pollination between different areas of neuroscience.

Chapter 5: Conclusion

5.1 – Summary

In this dissertation, I tested the prediction that hippocampal theta and gamma rhythm dynamics display consistent reproducible trends that depend on an animal's experience with its environment. This prediction was most directly tested in Chapter 2 where it was found that both theta and slow gamma rhythms vary in ways that parallel the acquisition of anticipatory coding in CA1 place cells. More specifically, theta amplitude was highest prior to, and during, the acquisition of anticipatory firing, while slow gamma emerged alongside anticipatory firing. In agreement with these basic results, running speed was found to correlate with theta amplitude most strongly during the early period of exposure to an environment each day, while correlations with slow gamma emerged alongside experience. Likewise, theta phase-slow gamma amplitude correlations became stronger with experience. Interestingly, no such experience-dependent effects were observed at fast gamma frequencies. It was suggested that changes observed at fast theta frequencies may be important for supporting synaptic plasticity, or for gating highly processed sensory information entering the hippocampus, during initial exposure to an environment. The effects observed at slow gamma frequencies were suggested to depend on synaptic plasticity in the Schaffer collaterals, and to signal an increase in the effective influence of CA3 over CA1 as a result of experience. A number of novel predictions and hypotheses were presented.

In Chapter 3, a triple-transgenic (3xTg) mouse model of Alzheimer's disease was used to investigate whether the above-described effects are abnormal in a mouse model of a memory disorder. The analyses built off recent results from our lab which demonstrated that place fields in these animals are less stable and less modulated by theta and slow gamma rhythms (Mably et al. 2017), and were additionally motivated by evidence of long term memory retrieval deficits in 3xTg mice (Billings et al. 2005; Roy et al. 2016). Surprisingly, experience-dependent trends in 3xTg place cell firing locations were at least as strong as those observed in control mice, and firing locations were retained across behavioral sessions within a day, suggesting normal acquisition and retrieval of spatial information across timescales on the order of minutes. These place field trends were accompanied by trends in theta and slow gamma amplitude that were consistent with those described characterized in Chapter 2. However, theta amplitude, theta phase-gamma amplitude correlations, and theta amplitude-running speed correlations were found to be abnormal in 3xTg mice. It was therefore suggested that abnormal theta/gamma rhythms may represent a potential biomarker for the early stages of Alzheimer's disease progression.

A second goal of the dissertation was to identify useful data analysis methods for handling the growing complexities of field potential data. To this end, Chapter 4 provided a practical introduction to the generalized additive model framework and its application to time-frequency analysis. While the chapter partially served as a tutorial for the statistical models used in Chapters 2-3, an effort was made to highlight the ways in which the framework is able to flexibly transition between different types of models, and could

thus be adapted to handle a broader range of problems. I discussed the functional ANOVA model as a useful tool for studying cross-frequency phase-amplitude correlations, and presented a novel point process model based on the wavelet modulus maxima lines and the Tweedie distribution. A number of alternative approaches and directions for future development were also identified.

5.2 – Discussion

Even though brain rhythms have been intensely studied for the past 150 years, progress toward understanding their origin, functional, and behavioral significance, has been relatively slow. Much of what prevents faster progress may be attributed to a lack of methods that are sufficiently able to measure, identify, and model the complicated dynamical properties of these patterns. Gamma rhythms are a case in point. The hardware to effectively record these signals did not become available until the early 1980s (Bressler and Freeman 1980; Buzsáki et al. 1983). Furthermore, proposals for their functional significance were not widely considered until even later when it was first suggested that synchronization of oscillatory patterns, at gamma frequency, might provide a mechanism to link spatially/anatomically distributed features into coherent neural representations that depend on external stimuli (Gray et al. 1989; Singer 1993). Even now, such proposals remain controversial.

Many of these early studies relied on analytical methods which inherently assumed stationarity. The popularization of the wavelet, and time-frequency methods in general, provided a means to characterize predictive input-output relationships between

external variables and time-frequency-limited processes (Tallon-Baudry et al. 1997; Mitra and Pesaran 1999). These methods have inspired new theories of temporal and spatial coordination of neural activity (Engel et al. 2001; Varela et al. 2001; Fries 2005; Jensen and Colgin 2007; Lisman and Jensen 2013; Hyafil et al. 2015), which have been supplemented by a variety of cross-frequency correlation measures (Tort et al. 2009, 2010; Kramer and Eden 2013; Dvorak and Fenton 2014; van Wijk et al. 2015; Stankovski et al. 2017; Dupré la Tour et al. 2017). These methods have, in turn, promoted the discovery of new physiological patterns, such as hippocampal slow and fast gamma rhythms (Colgin et al. 2009; Belluscio et al. 2012).

The results of this dissertation can be viewed as an effort to build from these recent discoveries by identifying factors which reliably, and reproducibly, predict when slow and fast gamma rhythms are likely to occur. Many reports have been published in recent years which have identified a potentially large number of such factors. For example, a number of studies have now shown that slow and fast gamma, and their respective theta phase correlations, depend reliably on running speed (Chen et al. 2011; Ahmed and Mehta 2012; Zheng et al. 2015; Gereke et al. 2018). Other studies have shown that slow gamma-related activity is enhanced during times when the hippocampus may be performing predictive, or memory retrieval, operations (Tort et al. 2009; Igarashi et al. 2014; Takahashi et al. 2014; Bieri 2015; Lasztóczki and Klausberger 2016b; Zheng et al. 2016a). Similarly, fast gamma-related activity has been shown to be enhanced during potential memory encoding operations (Cabral et al. 2014b; Takahashi et al. 2014; Bieri 2015; Zheng et al. 2016b). Still, others have found that slow gamma activity is

enhanced during novel object exploration (Trimper et al. 2014), that both slow and fast gamma activity are enhanced during novel environment exploration (Kemere et al. 2013), or that broad frequencies of gamma may variously be enhanced along the central arm, or at choice points, of a figure eight mazes during alternating choice tasks (Johnson and Redish 2007; Montgomery and Buzsáki 2007; Schomburg et al. 2014). The results of this dissertation suggest that the magnitudes of many of these types of effects are nonstationary, and may drift over time in subtle, but reliable and experience-dependent ways.

As we learn more about the many factors that influence brain rhythms, new methods are needed to handle these factors simultaneously, and to quantify their relative importance. The problem that needs to be solved is simple. Given the current state of the animal, and some prior knowledge, what types of patterns might we expect to see, and what is the likelihood of the observed pattern? Methods that effectively solve this problem will enable more precise hypothesis testing, and will provide more detailed descriptive models of the signals which may provide more physiological insight.

Up to this point, the majority of such methods have been developed for spiking data, and there has been more progress in that domain. For example, the point process generalized linear model constitutes a suite of tools that can be used to specify many types of encoding/decoding models, quantify goodness of fit, perform model comparison, as well as simulate new data (Truccolo et al. 2005; Pillow et al. 2008). The descriptions these models provide are able to capture a rich variety of variability that is observed in spiking data (Weber and Pillow 2017), and can be extended to promote biophysical

interpretations (Latimer et al. 2018). The study of brain rhythms will benefit from these advances, and efforts to frame different types of neural data into a common framework will be mutually beneficial on all fronts. The generalized additive model framework, and point process variants, discussed in this dissertation can be viewed as an initial step in this direction.

Developing interpretable dynamical models of field potentials will likely require us to move beyond the Fourier-based time-frequency methods, such as the wavelet transforms, used in this dissertation. While such methods are able to efficiently represent many types of multi-harmonic signals, they are prone to producing artifacts when signals contain nonharmonic components, or when components are spaced too closely in the time-frequency plane. Some simple examples of such artifacts were provided in Chapter 4. These types of artifacts make measures based on harmonic representations, such as most cross-frequency coupling measures, much harder to interpret (Kramer et al. 2008; Gerber et al. 2016; Lozano-Soldevilla et al. 2016; Scheffer-Teixeira and Tort 2016). It has, therefore, been suggested that while these measures may serve as convenient markers of biophysical processes, they may not contain any direct physical meaning (Aru et al. 2015).

It is recognized that nonlinear oscillatory features, such as waveform shape, vary predictably with behavior and may provide more information about physical processes (Sheremet et al. 2016; Cole and Voytek 2017). This has motivated the development of new time-domain methods which seek to parameterize waveform shape on a cycle-by-cycle basis (Belluscio et al. 2012; Cole and Voytek 2018). Others have introduced novel

unsupervised learning algorithms which discover recurring non-sinusoidal waveforms from field potential data (Brockmeier and Príncipe 2016; Loza et al. 2017). A number of relevant time-frequency domain methods have also been introduced outside neuroscience which directly model signals made up of multiple time-varying non-sinusoidal components (Iatsenko et al. 2015b; Lin et al. 2018; Xu et al. 2018). The related problem of unsupervised time series clustering also continues to receive a lot of attention (Bagnall et al. 2017).

New challenges and progress will also emerge in the spatial domain. Recent years have seen the rapid advancement of high channel-count recording technology (Steinmetz et al. 2018). These advancements will enable the discovery of new types data structures and patterns that are inaccessible with smaller channel counts. Furthermore, these structures may be more interpretable in terms of physical processes. Applications of dimensionality reduction and compressed sensing methods, such as independent components analysis and sparse coding, have already provided the first proofs of concept in this regard (Agarwal et al. 2014; Bouchard et al. 2017). For example, Agarwal et al. 2014 derived field potential components across multiple theta-filtered channels which resembled place cell activity. Thus, such methods may provide a new way to relate brain rhythms to underlying neuronal dynamics. Considering that spatial dimensionality reduction methods typically ignore spectro-temporal structure in the data, progress in this domain will likely benefit from novel dimensionality reduction algorithms that take both spatial and spectro-temporal structure into account. Thus, algorithms like spatio-spectral decomposition, dynamic mode decomposition, and delay differential analysis will

become increasingly important (Lainscsek and Sejnowski 2015; Brunton et al. 2016; Cohen 2017a, 2017b).

5.3 – Final Thoughts

The study of brain rhythms is evolving on many fronts simultaneously. The popularization of time-frequency analysis has allowed researchers to study the many ways in which spectral components, observed in local field potentials, are correlated with behavior and how they evolve over time and with experience. New statistical modeling frameworks are being developed which greatly expand the range, and dimensionality, of problems that can be handled. The biases inherent to sinusoidal signal representations are being addressed by novel signal processing algorithms aimed at discovering non-harmonic, physiologically relevant, waveforms. Lastly, new high density, high channel-count, recording hardware promises to enable the estimation of spatio-temporal waveform trajectories. Meaningful interpretation of field potential patterns in terms of biophysical processes will require careful collaboration on all of these fronts. The reward will be a better understanding of coordinated neural activity at multiple temporal, and spatial, scales.

References

- Addison PS.** The Illustrated Wavelet Transform Handbook: Introductory Theory and Applications in Science, Engineering, Medicine and Finance, Second Edition. CRC Press, 2017.
- Agarwal G, Stevenson IH, Berenyi A, Mizuseki K, Buzsaki G, Sommer FT.** Spatially Distributed Local Fields in the Hippocampus Encode Rat Position. *Science* 344: 626–630, 2014.
- Ahmed OJ, Mehta MR.** Running Speed Alters the Frequency of Hippocampal Gamma Oscillations. *J Neurosci* 32: 7373–7383, 2012.
- van Albada SJ, Robinson PA.** Transformation of arbitrary distributions to the normal distribution with application to EEG test-retest reliability. *J Neurosci Methods* 161: 205–211, 2007.
- Andersen P,** editor. The hippocampus book. Oxford ; New York: Oxford University Press, 2007.
- Aru J, Aru J, Priesemann V, Wibral M, Lana L, Pipa G, Singer W, Vicente R.** Untangling cross-frequency coupling in neuroscience. *Curr Opin Neurobiol* 31: 51–61, 2015.
- Ashe KH, Zahs KR.** Probing the Biology of Alzheimer’s Disease in Mice. *Neuron* 66: 631–645, 2010.
- Auger F, Flandrin P.** Improving the readability of time-frequency and time-scale representations by the reassignment method. *IEEE Trans Signal Process* 43: 1068–1089, 1995.
- Baayen H, Vasishth S, Kliegl R, Bates D.** The cave of shadows: Addressing the human factor with generalized additive mixed models. *J Mem Lang* 94: 206–234, 2017.
- Baayen RH, Rij J van, Cat C de, Wood S.** Autocorrelated Errors in Experimental Data in the Language Sciences: Some Solutions Offered by Generalized Additive Mixed Models. In: Mixed-Effects Regression Models in Linguistics. Springer, Cham, p. 49–69, 2018.
- Baddeley A, Rubak E, Turner R.** Spatial point patterns: methodology and applications with R. CRC Press, 2015.
- Baddeley A, Turner R.** Practical Maximum Pseudolikelihood for Spatial Point Patterns. *Aust N Z J Stat* 42: 283–322, 2000.

Bagnall A, Lines J, Bostrom A, Large J, Keogh E. The great time series classification bake off: a review and experimental evaluation of recent algorithmic advances. *Data Min Knowl Discov* 31: 606–660, 2017.

Bardenet R, Flamant J, Chainais P. On the zeros of the spectrogram of white noise. arXiv:1708.00082v1 [stat.ME], 2017.

Bateman RJ, Xiong C, Benzinger TLS, Fagan AM, Goate A, Fox NC, Marcus DS, Cairns NJ, Xie X, Blazey TM, Holtzman DM, Santacruz A, Buckles V, Oliver A, Moulder K, Aisen PS, Ghetti B, Klunk WE, McDade E, Martins RN, Masters CL, Mayeux R, Ringman JM, Rossor MN, Schofield PR, Sperling RA, Salloway S, Morris JC. Clinical and Biomarker Changes in Dominantly Inherited Alzheimer's Disease. *N Engl J Med* 367: 795–804, 2012.

Battaglia FP, Sutherland GR, McNaughton BL. Local Sensory Cues and Place Cell Directionality: Additional Evidence of Prospective Coding in the Hippocampus. *J Neurosci* 24: 4541–4550, 2004.

Belluscio MA, Mizuseki K, Schmidt R, Kempter R, Buzsáki G. Cross-Frequency Phase–Phase Coupling between Theta and Gamma Oscillations in the Hippocampus. *J Neurosci* 32: 423–435, 2012.

Bender F, Gorbaty M, Cadavieco MC, Denisova N, Gao X, Holman C, Korotkova T, Ponomarenko A. Theta oscillations regulate the speed of locomotion via a hippocampus to lateral septum pathway. *Nat Commun* 6: 8521, 2015.

Berger H. Über das Elektrenkephalogramm des Menschen. *Arch Für Psychiatr Nervenkrankh* 87: 527–570, 1929.

Bieri KW. Slow and fast gamma rhythms represent distinct memory processing states in the hippocampus. 2015. <http://hdl.handle.net/2152/39202>

Bieri KW, Bobbitt KN, Colgin LL. Slow and Fast Gamma Rhythms Coordinate Different Spatial Coding Modes in Hippocampal Place Cells. *Neuron* 82: 670–681, 2014.

Billings LM, Oddo S, Green KN, McGaugh JL, LaFerla FM. Intraneuronal A β Causes the Onset of Early Alzheimer's Disease-Related Cognitive Deficits in Transgenic Mice. *Neuron* 45: 675–688, 2005.

Bliss TVP, Lømo T. Long-lasting potentiation of synaptic transmission in the dentate area of the anaesthetized rabbit following stimulation of the perforant path. *J Physiol* 232: 331–356, 1973.

Blum KI, Abbott LF. A Model of Spatial Map Formation in the Hippocampus of the Rat. *Neural Comput* 8: 85–93, 1996.

Booth CA, Witton J, Nowacki J, Tsaneva-Atanasova K, Jones MW, Randall AD, Brown JT. Altered Intrinsic Pyramidal Neuron Properties and Pathway-Specific Synaptic Dysfunction Underlie Aberrant Hippocampal Network Function in a Mouse Model of Tauopathy. *J Neurosci* 36: 350–363, 2016.

Bouchard KE, Bujan AF, Chang EF, Sommer FT. Sparse coding of ECoG signals identifies interpretable components for speech control in human sensorimotor cortex. 39th Annual International Conference of the IEEE Engineering in Medicine and Biology Society (EMBC), Seogwipo, pp. 3636-3639, 2017.

Braak H, Braak E. Staging of alzheimer's disease-related neurofibrillary changes. *Neurobiol Aging* 16: 271–278, 1995.

Bragin A, Jando G, Nadasdy Z, Hetke J, Wise K, Buzsaki G. Gamma (40-100 Hz) oscillation in the hippocampus of the behaving rat. *J Neurosci* 15: 47, 1995.

Bressler SL, Freeman WJ. Frequency analysis of olfactory system EEG in cat, rabbit, and rat. *Electroencephalogr Clin Neurophysiol* 50: 19–24, 1980.

Brockmeier AJ, Príncipe JC. Learning Recurrent Waveforms Within EEGs. *IEEE Trans Biomed Eng* 63: 43–54, 2016.

Brown EN, Barbieri R, Ventura V, Kass RE, Frank LM. The Time-Rescaling Theorem and Its Application to Neural Spike Train Data Analysis. *Neural Comput* 14: 325–346, 2002.

Brunns A. Fourier-, Hilbert- and wavelet-based signal analysis: are they really different approaches? *J Neurosci Methods* 137: 321–332, 2004.

Brunton BW, Johnson LA, Ojemann JG, Kutz JN. Extracting spatial–temporal coherent patterns in large-scale neural recordings using dynamic mode decomposition. *J Neurosci Methods* 258: 1–15, 2016.

Buzsáki G. Hippocampal sharp waves: Their origin and significance. *Brain Res* 398: 242–252, 1986.

Buzsáki G. Theta Oscillations in the Hippocampus. *Neuron* 33: 325–340, 2002.

Buzsáki G, Anastassiou CA, Koch C. The origin of extracellular fields and currents — EEG, ECoG, LFP and spikes. *Nat Rev Neurosci* 13: 407–420, 2012.

Buzsáki G, Buhl DL, Harris KD, Csicsvari J, Czéh B, Morozov A. Hippocampal network patterns of activity in the mouse. *Neuroscience* 116: 201–211, 2003.

Buzsáki G, Lai-Wo S. L, Vanderwolf CH. Cellular bases of hippocampal EEG in the behaving rat. *Brain Res Rev* 6: 139–171, 1983.

Buzsaki G, Penttonen M, Nadasdy Z, Bragin A. Pattern and inhibition-dependent invasion of pyramidal cell dendrites by fast spikes in the hippocampus in vivo. *Proc Natl Acad Sci* 93: 9921–9925, 1996.

Buzsáki G, Wang X-J. Mechanisms of Gamma Oscillations. *Annu Rev Neurosci* 35: 203–225, 2012.

Cabral HO, Fouquet C, Rondi-Reig L, Pennartz CMA, Battaglia FP. Single-Trial Properties of Place Cells in Control and CA1 NMDA Receptor Subunit 1-KO Mice. *J Neurosci* 34: 15861–15869, 2014a.

Cabral HO, Vinck M, Fouquet C, Pennartz CMA, Rondi-Reig L, Battaglia FP. Oscillatory Dynamics and Place Field Maps Reflect Hippocampal Ensemble Processing of Sequence and Place Memory under NMDA Receptor Control. *Neuron* 81: 402–415, 2014b.

Cacucci F, Yi M, Wills TJ, Chapman P, O’Keefe J. Place cell firing correlates with memory deficits and amyloid plaque burden in Tg2576 Alzheimer mouse model. *Proc Natl Acad Sci* 105: 7863–7868, 2008.

Cajal SR y. The Croonian lecture.—La fine structure des centres nerveux. *Proc R Soc Lond* 55: 444–468, 1894.

Cappaert NLM, Van Strien NM, Witter MP. Chapter 20 - Hippocampal Formation. In: *The Rat Nervous System* (Fourth Edition), edited by Paxinos G. Academic Press, p. 511–573, 2015.

Cayzac S, Mons N, Ginguay A, Allinquant B, Jeantet Y, Cho YH. Altered hippocampal information coding and network synchrony in APP-PS1 mice. *Neurobiol Aging* 36: 3200–3213, 2015.

Chassande-Mottin E, Daubechies I, Auger F, Flandrin P. Differential reassignment. *IEEE Signal Process Lett* 4: 293–294, 1997.

Chen Z, Resnik E, McFarland JM, Sakmann B, Mehta MR. Speed Controls the Amplitude and Timing of the Hippocampal Gamma Rhythm. *PLOS ONE* 6: e21408, 2011.

Cheng J, Ji D. Rigid firing sequences undermine spatial memory codes in a neurodegenerative mouse model. *eLife* 2, 2013.

Cheng S, Frank LM. New Experiences Enhance Coordinated Neural Activity in the Hippocampus. *Neuron* 57: 303–313, 2008.

Chrobak JJ, Stackman RW, Walsh TJ. Intraseptal administration of muscimol produces dose-dependent memory impairments in the rat. *Behav Neural Biol* 52: 357–369, 1989.

Ciupek SM, Cheng J, Ali YO, Lu H-C, Ji D. Progressive Functional Impairments of Hippocampal Neurons in a Tauopathy Mouse Model. *J Neurosci* 35: 8118–8131, 2015.

Cohen MX. Fluctuations in Oscillation Frequency Control Spike Timing and Coordinate Neural Networks. *J Neurosci* 34: 8988–8998, 2014.

Cohen MX. Using spatiotemporal source separation to identify prominent features in multichannel data without sinusoidal filters. *Eur. J. Neurosci.*, 2017.
doi:10.1111/ejn.13727

Cohen MX. Multivariate cross-frequency coupling via generalized eigendecomposition. *eLife* 6: e21792, 2017b.

Cole SR, Voytek B. Brain Oscillations and the Importance of Waveform Shape. *Trends Cogn Sci* 21: 137–149, 2017.

Cole SR, Voytek B. Cycle-by-cycle analysis of neural oscillations. *bioRxiv* (April 16, 2018). doi: 10.1101/302000.

Colgin LL. Mechanisms and Functions of Theta Rhythms. *Annu Rev Neurosci* 36: 295–312, 2013.

Colgin LL. Do slow and fast gamma rhythms correspond to distinct functional states in the hippocampal network? *Brain Res* 1621: 309–315, 2015.

Colgin LL, Denninger T, Fyhn M, Hafting T, Bonnevie T, Jensen O, Moser M-B, Moser EI. Frequency of gamma oscillations routes flow of information in the hippocampus. *Nature* 462: 353–357, 2009.

Corkin S, Amaral DG, González RG, Johnson KA, Hyman BT. HM's medial temporal lobe lesion: findings from magnetic resonance imaging. *J Neurosci* 17: 3964–3979, 1997.

Csicsvari J, Jamieson B, Wise KD, Buzsáki G. Mechanisms of Gamma Oscillations in the Hippocampus of the Behaving Rat. *Neuron* 37: 311–322, 2003.

Cutsuridis V, Graham B, Cobb S, Vida I, editors. *Hippocampal Microcircuits*. Springer New York. 2010.

Daley DJ, Vere-Jones D. An introduction to the theory of point processes. 2nd ed. New York: Springer, 2003.

De Almeida L, Idiart M, Villavicencio A, Lisman J. Alternating predictive and short-term memory modes of entorhinal grid cells. *Hippocampus* 22: 1647–1651, 2012.

Ding M, Bressler SL, Yang W, Liang H. Short-window spectral analysis of cortical event-related potentials by adaptive multivariate autoregressive modeling: data preprocessing, model validation, and variability assessment. *Biol Cybern* 83: 35–45, 2000.

Duong T. ks: Kernel density estimation and kernel discriminant analysis for multivariate data in R. *J Stat Softw* 21: 1–16, 2007.

Duong T. Non-parametric smoothed estimation of multivariate cumulative distribution and survival functions, and receiver operating characteristic curves. *J Korean Stat Soc* 45: 33–50, 2016.

Dupré la Tour T, Tallot L, Grabot L, Doyère V, van Wassenhove V, Grenier Y, Gramfort A. Non-linear auto-regressive models for cross-frequency coupling in neural time series. *PLOS Comput Biol* 13(12): e1005893, 2017.

Dupret D, O'Neill J, Pleydell-Bouverie B, Csicsvari J. The reorganization and reactivation of hippocampal maps predict spatial memory performance. *Nat Neurosci* 13: 995–1002, 2010.

Dvorak D, Fenton AA. Toward a proper estimation of phase–amplitude coupling in neural oscillations. *J Neurosci Methods* 225: 42–56, 2014.

Ekstrom AD, Meltzer J, McNaughton BL, Barnes CA. NMDA Receptor Antagonism Blocks Experience-Dependent Expansion of Hippocampal “Place Fields.” *Neuron* 31: 631–638, 2001.

Engel AK, Fries P, Singer W. Dynamic predictions: Oscillations and synchrony in top–down processing. *Nat Rev Neurosci* 2: 704–716, 2001.

Feng T, Silva D, Foster DJ. Dissociation between the Experience-Dependent Development of Hippocampal Theta Sequences and Single-Trial Phase Precession. *J Neurosci* 35: 4890–4902, 2015.

Fernández-Ruiz A, Oliva A, Nagy GA, Maurer AP, Berényi A, Buzsáki G. Entorhinal-CA3 Dual-Input Control of Spike Timing in the Hippocampus by Theta-Gamma Coupling. *Neuron* 93: 1213–1226.e5, 2017.

Ferri CP, Prince M, Brayne C, Brodaty H, Fratiglioni L, Ganguli M, Hall K, Hasegawa K, Hendrie H, Huang Y, Jorm A, Mathers C, Menezes PR, Rimmer E, Scazufca M. Global prevalence of dementia: a Delphi consensus study. *366*: 6, 2005.

Filippini N, MacIntosh BJ, Hough MG, Goodwin GM, Frisoni GB, Smith SM, Matthews PM, Beckmann CF, Mackay CE. Distinct patterns of brain activity in young carriers of the APOE-ε4 allele. *Proc Natl Acad Sci* *106*: 7209–7214, 2009.

Finger S. *Origins of Neuroscience: A History of Explorations Into Brain Function.* Oxford University Press, 2001.

Flandrin P. Time-frequency filtering based on spectrogram zeros. *IEEE Signal Process Lett* *22*: 2137–2141, 2015.

Flandrin P. The sound of silence: Recovering signals from time-frequency zeros. *50th Asilomar Conference on Signals, Systems and Computers*, p. 544–548, 2016.

Flandrin P. On spectrogram local maxima. *IEEE International Conference on Acoustics, Speech and Signal Processing*, p. 3979–3983, 2017.

Flandrin P, Auger F, Chassande-Mottin E. Time-frequency reassignment: from principles to algorithms. *Appl Time-Freq Signal Process* *5*: 102, 2003.

Florian G, Pfurtscheller G. Dynamic spectral analysis of event-related EEG data. *Electroencephalogr Clin Neurophysiol* *95*: 393–396, 1995.

Foster DJ, Wilson MA. Reverse replay of behavioural sequences in hippocampal place cells during the awake state. *Nature* *440*: 680–683, 2006.

Fox SE, Ranck JB. Electrophysiological characteristics of hippocampal complex-spike cells and theta cells. *Exp Brain Res* *41*: 399–410, 1981.

Freeman WJ. Hilbert transform for brain waves. *Scholarpedia* *2*: 1338, 2007.

Fries P. A mechanism for cognitive dynamics: neuronal communication through neuronal coherence. *Trends Cogn Sci* *9*: 474–480, 2005.

Fuhrmann F, Justus D, Sosulina L, Kaneko H, Beutel T, Friedrichs D, Schoch S, Schwarz MK, Fuhrmann M, Remy S. Locomotion, Theta Oscillations, and the Speed-Correlated Firing of Hippocampal Neurons Are Controlled by a Medial Septal Glutamatergic Circuit. *Neuron* *86*: 1253–1264, 2015.

Gabor D. Theory of communication. Part 1: The analysis of information. *J Inst Electr Eng - Part III Radio Commun Eng* *93*: 429-441(12), 1946.

Gardner TJ, Magnasco MO. Sparse time-frequency representations. *Proc Natl Acad Sci* 103: 6094–6099, 2006.

Gasparrini A, Scheipl F, Armstrong B, Kenward MG. A penalized framework for distributed lag non-linear models. *Biometrics* 73: 938–948, 2017.

Gerber EM, Sadeh B, Ward A, Knight RT, Deouell LY. Non-Sinusoidal Activity Can Produce Cross-Frequency Coupling in Cortical Signals in the Absence of Functional Interaction between Neural Sources. *PLOS ONE* 11: e0167351, 2016.

Gereke BJ, Mably AJ, Colgin LL. Experience-dependent trends in CA1 theta and slow gamma rhythms in freely behaving mice. *J Neurophysiol* 119: 476–489, 2018.

Giménez-Llort L, Blázquez G, Cañete T, Johansson B, Oddo S, Tobeña A, LaFerla FM, Fernández-Teruel A. Modeling behavioral and neuronal symptoms of Alzheimer's disease in mice: A role for intraneuronal amyloid. *Neurosci Biobehav Rev* 31: 125–147, 2007.

Goutagny R, Gu N, Cavanagh C, Jackson J, Chabot J-G, Quirion R, Krantic S, Williams S. Alterations in hippocampal network oscillations and theta–gamma coupling arise before A β overproduction in a mouse model of Alzheimer's disease. *Eur J Neurosci* 37: 1896–1902, 2013.

Grastyán E, Karmos G, Vereczkey L, Kellényi L. The hippocampal electrical correlates of the homeostatic regulation of motivation. *Electroencephalogr Clin Neurophysiol* 21: 34–53, 1966.

Grastyán E, Lissák K, Madarász I, Donhoffer H. Hippocampal electrical activity during the development of conditioned reflexes. *Electroencephalogr Clin Neurophysiol* 11: 409–430, 1959.

Gray CM, König P, Engel AK, Singer W. Oscillatory responses in cat visual cortex exhibit inter-columnar synchronization which reflects global stimulus properties. *Nature* 338: 334–337, 1989.

Green JD, Arduini AA. Hippocampal electrical activity in arousal. *J Neurophysiol* 17: 531–557, 1954.

Greenstein YJ, Pavlides C, Winson J. Long-term potentiation in the dentate gyrus is preferentially induced at theta rhythm periodicity. *Brain Res* 438: 331–334, 1988.

Greven S, Scheipl F. A general framework for functional regression modelling. *Stat Model* 17: 1–35, 2017.

Gröchenig K. Foundations of time-frequency analysis. Springer Science & Business Media, 2013.

Grossmann A, Morlet J. Decomposition of Hardy Functions into Square Integrable Wavelets of Constant Shape. SIAM J Math Anal Phila 15: 14, 1984.

Grunwald GK, Hyndman RJ, Tedesco LM, Tweedie RL. A unified view of linear AR(1) models. Unpublished manuscript Monash University, 1995.

Harmouche J, Fourer D, Auger F, Borgnat P, Flandrin P. The Sliding Singular Spectrum Analysis: A Data-Driven Nonstationary Signal Decomposition Tool. IEEE Trans Signal Process 66: 251–263, 2018.

Harris KD, Henze DA, Csicsvari J, Hirase H, Buzsáki G. Accuracy of Tetrode Spike Separation as Determined by Simultaneous Intracellular and Extracellular Measurements. J Neurophysiol 84: 401–414, 2000.

Hartig F. DHARMA: residual diagnostics for hierarchical (multi-level/mixed) regression models. R package version 0.1. 5. 2017.

Hastie TJ, Tibshirani RJ. Generalised additive models. Chapman and Hall. CRC Monogr. Stat. Appl. Probab. 1990.

Hebb DO. The organization of behavior: A neuropsychological theory. Psychology Press, 1949.

Henze DA, Borhegyi Z, Csicsvari J, Mamiya A, Harris KD, Buzsáki G. Intracellular features predicted by extracellular recordings in the hippocampus in vivo. J Neurophysiol 84: 390–400, 2000.

Hollup SA, Molden S, Donnett JG, Moser M-B, Moser EI. Accumulation of hippocampal place fields at the goal location in an annular watermaze task. J Neurosci 21: 1635–1644, 2001.

Hölscher C, Anwyl R, Rowan MJ. Stimulation on the positive phase of hippocampal theta rhythm induces long-term potentiation that can be depotentiated by stimulation on the negative phase in area CA1 in vivo. J Neurosci 17: 6470–6477, 1997.

Huang NE, Shen Z, Long SR, Wu MC, Shih HH, Zheng Q, Yen N-C, Tung CC, Liu HH. The empirical mode decomposition and the Hilbert spectrum for nonlinear and non-stationary time series analysis. Proc R Soc Lond Math Phys Eng Sci 454: 903–995, 1998.

Hyafil A, Giraud A-L, Fontolan L, Gutkin B. Neural Cross-Frequency Coupling: Connecting Architectures, Mechanisms, and Functions. Trends Neurosci 38: 725–740, 2015.

- Hyman JM, Wyble BP, Goyal V, Rossi CA, Hasselmo ME.** Stimulation in Hippocampal Region CA1 in Behaving Rats Yields Long-Term Potentiation when Delivered to the Peak of Theta and Long-Term Depression when Delivered to the Trough. *J Neurosci* 23: 11725–11731, 2003.
- Iaccarino HF, Singer AC, Martorell AJ, Rudenko A, Gao F, Gillingham TZ, Mathys H, Seo J, Kritskiy O, Abdurrob F, Adaikkan C, Canter RG, Rueda R, Brown EN, Boyden ES, Tsai L-H.** Gamma frequency entrainment attenuates amyloid load and modifies microglia. *Nature* 540: 230–235, 2016.
- Iatsenko D, McClintock PVE, Stefanovska A.** Linear and synchrosqueezed time-frequency representations revisited: Overview, standards of use, resolution, reconstruction, concentration, and algorithms. *Digit Signal Process* 42: 1–26, 2015a.
- Iatsenko D, McClintock PVE, Stefanovska A.** Nonlinear mode decomposition: A noise-robust, adaptive decomposition method. *Phys Rev E* 92, 2015b.
- Iatsenko D, McClintock PVE, Stefanovska A.** Extraction of instantaneous frequencies from ridges in time-frequency representations of signals. *Signal Process* 125: 290–303, 2016.
- Igarashi KM, Lu L, Colgin LL, Moser M-B, Moser EI.** Coordination of entorhinal–hippocampal ensemble activity during associative learning. *Nature* 510: 143–147, 2014.
- Imran S, Jamil A, Ismail SS, Kashif FM.** Techniques to obtain good resolution and concentrated time-frequency distributions: a review. *EURASIP J Adv Signal Process* 2009: 1–43, 2009.
- Ittner AA, Gladbach A, Bertz J, Suh LS, Ittner LM.** p38 MAP kinase-mediated NMDA receptor-dependent suppression of hippocampal hypersynchronicity in a mouse model of Alzheimer’s disease. *Acta Neuropathol Commun* 2: 149, 2014.
- Jensen O, Colgin LL.** Cross-frequency coupling between neuronal oscillations. *Trends Cogn Sci* 11: 267–269, 2007.
- Jensen O, Lisman JE.** Hippocampal CA3 region predicts memory sequences: accounting for the phase precession of place cells. *Learn Mem* 3: 279–287, 1996a.
- Jensen O, Lisman JE.** Theta/gamma networks with slow NMDA channels learn sequences and encode episodic memory: role of NMDA channels in recall. *Learn Mem* 3: 264–278, 1996b.
- Johnson A, Redish AD.** Neural Ensembles in CA3 Transiently Encode Paths Forward of the Animal at a Decision Point. *J Neurosci* 27: 12176–12189, 2007.

Jorgensen B. Exponential Dispersion Models. *J R Stat Soc Ser B Methodol* 49: 127–162, 1987.

Jung R, Kornmüller AE. Eine Methodik der Ableitung lokalisierter Potentialschwankungen aus subcorticalen Hirngebieten. *Arch Für Psychiatr Nervenkrankh* 109: 1–30, 1938.

Karran E, Mercken M, Strooper BD. The amyloid cascade hypothesis for Alzheimer's disease: an appraisal for the development of therapeutics. *Nat Rev Drug Discov* 10: 698–712, 2011.

Kemere C, Carr MF, Karlsson MP, Frank LM. Rapid and Continuous Modulation of Hippocampal Network State during Exploration of New Places. *PLoS ONE* 8: e73114, 2013.

Kiebel SJ, Tallon-Baudry C, Friston KJ. Parametric analysis of oscillatory activity as measured with EEG/MEG. *Hum Brain Mapp* 26: 170–177, 2005.

Kiss J, Buzsaki G, Morrow JS, Glantz SB, Leranth C. Entorhinal cortical innervation of parvalbumin-containing neurons (basket and chandelier cells) in the rat ammon's horn. *Hippocampus* 6: 239–246, 1996.

Korotkova T, Ponomarenko A, Monaghan CK, Poulter SL, Cacucci F, Wills T, Hasselmo ME, Lever C. Reconciling the different faces of hippocampal theta: The role of theta oscillations in cognitive, emotional and innate behaviors. *Neurosci Biobehav Rev* 85: 65–80, 2018.

Kramer MA, Eden UT. Assessment of cross-frequency coupling with confidence using generalized linear models. *J Neurosci Methods* 220: 64–74, 2013.

Kramer MA, Tort ABL, Kopell NJ. Sharp edge artifacts and spurious coupling in EEG frequency comodulation measures. *J Neurosci Methods* 170: 352–357, 2008.

Kramis R, Vanderwolf CH, Bland BH. Two types of hippocampal rhythmical slow activity in both the rabbit and the rat: Relations to behavior and effects of atropine, diethyl ether, urethane, and pentobarbital. *Exp Neurol* 49: 58–85, 1975.

Krivobokova T, Kauermann G. A Note on Penalized Spline Smoothing With Correlated Errors. *J Am Stat Assoc* 102: 1328–1337, 2007.

Lainscsek C, Sejnowski TJ. Delay Differential Analysis of Time Series. *Neural Comput* 27: 594–614, 2015.

Larson J, Lynch G. Theta pattern stimulation and the induction of LTP: the sequence in which synapses are stimulated determines the degree to which they potentiate. *Brain Res* 489: 49–58, 1989.

Larson J, Wong D, Lynch G. Patterned stimulation at the theta frequency is optimal for the induction of hippocampal long-term potentiation. *Brain Res* 368: 347–350, 1986.

Lasztóczki B, Klausberger T. Layer-Specific GABAergic Control of Distinct Gamma Oscillations in the CA1 Hippocampus. *Neuron* 81: 1126–1139, 2014.

Lasztóczki B, Klausberger T. Hippocampal Place Cells Couple to Three Different Gamma Oscillations during Place Field Traversal. *Neuron* 91: 34–40, 2016a.

Lasztóczki B, Klausberger T. Hippocampal Place Cells Couple to Three Different Gamma Oscillations during Place Field Traversal. *Neuron* 91: 34–40, 2016b.

Latimer K, Rieke F, Pillow JW. Inferring synaptic inputs from spikes with a conductance-based neural encoding model. *bioRxiv* (March 13, 2018). doi: 10.1101/281089.

Le Van Quyen M, Bragin A. Analysis of dynamic brain oscillations: methodological advances. *Trends Neurosci* 30: 365–373, 2007.

Le Van Quyen M, Foucher J, Lachaux J-P, Rodriguez E, Lutz A, Martinerie J, Varela FJ. Comparison of Hilbert transform and wavelet methods for the analysis of neuronal synchrony. *J Neurosci Methods* 111: 83–98, 2001.

Lee I, Rao G, Knierim JJ. A Double Dissociation between Hippocampal Subfields: Differential Time Course of CA3 and CA1 Place Cells for Processing Changed Environments. *Neuron* 42: 803–815, 2004.

Levy WB, Steward O. Temporal contiguity requirements for long-term associative potentiation/depression in the hippocampus. *Neuroscience* 8: 791–797, 1983.

Lin C-Y, Su L, Wu H-T. Wave-Shape Function Analysis: When Cepstrum Meets Time-Frequency Analysis. *J Fourier Anal Appl* 24: 451–505, 2018.

Lisman J, Idiart M. Storage of 7 +/- 2 short-term memories in oscillatory subcycles. *Science* 267: 1512–1515, 1995.

Lisman JE, Jensen O. The Theta-Gamma Neural Code. *Neuron* 77: 1002–1016, 2013.

Litvak V, Jha A, Flandin G, Friston K. Convolution models for induced electromagnetic responses. *NeuroImage* 64: 388–398, 2013.

Liu Lintao, Hsu Houtse, Grafarend Erik W. Normal Morlet wavelet transform and its application to the Earth's polar motion. *J Geophys Res Solid Earth* 112, 2007.

Lømo T. The discovery of long-term potentiation. *Philos Trans R Soc B Biol Sci* 358: 617–620, 2003.

Loza CA, Okun MS, Príncipe JC. A Marked Point Process Framework for Extracellular Electrical Potentials. *Front Syst Neurosci* 11:95, 2017.

Lozano-Soldevilla D, ter Huurne N, Oostenveld R. Neuronal Oscillations with Non-sinusoidal Morphology Produce Spurious Phase-to-Amplitude Coupling and Directionality. *Front Comput Neurosci* 10:87, 2016.

Mably AJ, Gereke BJ, Jones DT, Colgin LL. Impairments in spatial representations and rhythmic coordination of place cells in the 3xTg mouse model of Alzheimer's disease. *Hippocampus* 27: 378–392, 2017.

Magee JC, Johnston D. A Synaptically Controlled, Associative Signal for Hebbian Plasticity in Hippocampal Neurons. *Science* 275: 209–213, 1997.

Mallat S. *A Wavelet Tour of Signal Processing: The Sparse Way*. Academic Press, 2008.

Mallat SG, Zhang Z. Matching pursuits with time-frequency dictionaries. *IEEE Trans Signal Process* 41: 3397–3415, 1993.

Mann EO, Paulsen O. Mechanisms underlying gamma ('40Hz') network oscillations in the hippocampus—a mini-review. *Prog Biophys Mol Biol* 87: 67–76, 2005.

Maraun D, Kurths J. Cross wavelet analysis: significance testing and pitfalls. *Nonlinear Process Geophys* 11: 505–514, 2004.

McFarland WL, Teitelbaum H, Hedges EK. Relationship between hippocampal theta activity and running speed in the rat. *J Comp Physiol Psychol* 88: 324–328, 1975.

Mehta MR. From synaptic plasticity to spatial maps and sequence learning. *Hippocampus* 25: 756–762, 2015.

Mehta MR, Barnes CA, McNaughton BL. Experience-dependent, asymmetric expansion of hippocampal place fields. *Proc Natl Acad Sci* 94: 8918–8921, 1997.

Mehta MR, Lee AK, Wilson MA. Role of experience and oscillations in transforming a rate code into a temporal code. *Nature* 417: 741–746, 2002.

Mehta MR, Quirk MC, Wilson MA. Experience-Dependent Asymmetric Shape of Hippocampal Receptive Fields. *Neuron* 25: 707–715, 2000.

Meignen S, Oberlin T, Depalle P, Flandrin P, McLaughlin S. Adaptive multimode signal reconstruction from time–frequency representations. *Philos Trans R Soc Math Phys Eng Sci* 374: 20150205, 2016.

Melzer S, Michael M, Caputi A, Eliava M, Fuchs EC, Whittington MA, Monyer H. Long-Range–Projecting GABAergic Neurons Modulate Inhibition in Hippocampus and Entorhinal Cortex. *Science* 335: 1506–1510, 2012.

Meyer AF, Williamson RS, Linden JF, Sahani M. Models of Neuronal Stimulus-Response Functions: Elaboration, Estimation, and Evaluation. *Front. Syst. Neurosci.* 10:109, 2017.

Milner B, Corkin S, Teuber H-L. Further analysis of the hippocampal amnesia syndrome: 14-year follow-up study of H.M. *Neuropsychologia* 6: 215–234, 1968.

Mitchell SJ, Rawlins JN, Steward O, Olton DS. Medial septal area lesions disrupt theta rhythm and cholinergic staining in medial entorhinal cortex and produce impaired radial arm maze behavior in rats. *J Neurosci* 2: 292–302, 1982.

Mitra PP, Pesaran B. Analysis of Dynamic Brain Imaging Data. *Biophys J* 76: 691–708, 1999.

Mizumori SJY, Perez GM, Alvarado MC, Barnes CA, McNaughton BL. Reversible inactivation of the medial septum differentially affects two forms of learning in rats. *Brain Res* 528: 12–20, 1990.

Mondadori CRA, Buchmann A, Mustovic H, Schmidt CF, Boesiger P, Nitsch RM, Hock C, Streffer J, Henke K. Enhanced brain activity may precede the diagnosis of Alzheimer’s disease by 30 years. *Brain* 129: 2908–2922, 2006.

Montgomery SM, Buzsáki G. Gamma oscillations dynamically couple hippocampal CA3 and CA1 regions during memory task performance. *Proc Natl Acad Sci* 104: 14495–14500, 2007.

Morlet J, Arens G, Fourgeau E, Glard D. Wave propagation and sampling theory—Part I: Complex signal and scattering in multilayered media. *GEOPHYSICS* 47: 203–221, 1982.

Muller RU, Kubie JL. The firing of hippocampal place cells predicts the future position of freely moving rats. *J Neurosci* 9: 4101–4110, 1989.

Nadaraya E. On Estimating Regression. *Theory Probab Its Appl* 9: 141–142, 1964.

Nelder JA, Wedderburn RWM. Generalized Linear Models. *J R Stat Soc Ser Gen* 135: 370–384, 1972.

Oddo S, Caccamo A, Kitazawa M, Tseng BP, LaFerla FM. Amyloid deposition precedes tangle formation in a triple transgenic model of Alzheimer's disease. *Neurobiol Aging* 24: 1063–1070, 2003a.

Oddo S, Caccamo A, Shepherd JD, Murphy MP, Golde TE, Kayed R, Metherate R, Mattson MP, Akbari Y, LaFerla FM. Triple-Transgenic Model of Alzheimer's Disease with Plaques and Tangles: Intracellular A β and Synaptic Dysfunction. *Neuron* 39: 409–421, 2003b.

O'Keefe J. Place units in the hippocampus of the freely moving rat. *Exp Neurol* 51: 78–109, 1976.

O'Keefe J, Dostrovsky J. The hippocampus as a spatial map. Preliminary evidence from unit activity in the freely-moving rat. *Brain Res* 34: 171–175, 1971.

O'Keefe J, Nadel L. The hippocampus as a cognitive map. Oxford : New York: Clarendon Press ; Oxford University Press, 1978.

O'Keefe J, Recce ML. Phase relationship between hippocampal place units and the EEG theta rhythm. *Hippocampus* 3: 317–330, 1993.

Pavlides C, Greenstein YJ, Grudman M, Winson J. Long-term potentiation in the dentate gyrus is induced preferentially on the positive phase of θ -rhythm. *Brain Res* 439: 383–387, 1988.

Petsche H, Stumpf CH, Gogolak G. The significance of the rabbit's septum as a relay station between the midbrain and the hippocampus I. The control of hippocampus arousal activity by the septum cells. *Clin Neurophysiol* 14: 202–211, 1962.

Pfeiffer BE, Foster DJ. Hippocampal place-cell sequences depict future paths to remembered goals. *Nature* 497: 74–79, 2013.

Pillow JW, Shlens J, Paninski L, Sher A, Litke AM, Chichilnisky EJ, Simoncelli EP. Spatio-temporal correlations and visual signalling in a complete neuronal population. *Nature* 454: 995–999, 2008.

Quirk MC, Blum KI, Wilson MA. Experience-dependent changes in extracellular spike amplitude may reflect regulation of dendritic action potential back-propagation in rat hippocampal pyramidal cells. *J Neurosci* 21: 240–248, 2001.

Quirk MC, Wilson MA. Interaction between spike waveform classification and temporal sequence detection. *J Neurosci Methods* 94: 41–52, 1999.

Ranck JB. Studies on single neurons in dorsal hippocampal formation and septum in unrestrained rats: Part I. Behavioral correlates and firing repertoires. *Exp Neurol* 41: 462–531, 1973.

Reiman EM, Quiroz YT, Fleisher AS, Chen K, Velez-Pardo C, Jimenez-Del-Rio M, Fagan AM, Shah AR, Alvarez S, Arbelaez A, Giraldo M, Acosta-Baena N, Sperling RA, Dickerson B, Stern CE, Tirado V, Munoz C, Reiman RA, Huentelman MJ, Alexander GE, Langbaum JB, Kosik KS, Tariot PN, Lopera F. Brain imaging and fluid biomarker analysis in young adults at genetic risk for autosomal dominant Alzheimer's disease in the presenilin 1 E280A kindred: a case-control study. *Lancet Neurol* 11: 1048–1056, 2012.

van Rij J, Wieling M, Baayen RH, van Rijn H. itsadug: Interpreting time series and autocorrelated data using gamms. R Package Version 2, 2016.

Roth ED, Yu X, Rao G, Knierim JJ. Functional Differences in the Backward Shifts of CA1 and CA3 Place Fields in Novel and Familiar Environments. *PLoS ONE* 7: e36035, 2012.

Roy DS, Arons A, Mitchell TI, Pignatelli M, Ryan TJ, Tonegawa S. Memory retrieval by activating engram cells in mouse models of early Alzheimer's disease. *Nature* 531: 508–512, 2016.

Rubio SE, Vega-Flores G, Martínez A, Bosch C, Pérez-Mediavilla A, del Río J, Gruart A, Delgado-García JM, Soriano E, Pascual M. Accelerated aging of the GABAergic septohippocampal pathway and decreased hippocampal rhythms in a mouse model of Alzheimer's disease. *FASEB J* 26: 4458–4467, 2012.

Rudrauf D, Douiri A, Kovach C, Lachaux J-P, Cosmelli D, Chavez M, Adam C, Renault B, Martinerie J, Le Van Quyen M. Frequency flows and the time-frequency dynamics of multivariate phase synchronization in brain signals. *NeuroImage* 31: 209–227, 2006.

Ruppert D, Wand MP, Carroll RJ. Semiparametric Regression. Camb. Core 2003.

Schaefer RW, Oppenheim AV. Discrete-time signal processing. Prentice-Hall. 1989.

Scheffer-Teixeira R, Tort AB. On cross-frequency phase-phase coupling between theta and gamma oscillations in the hippocampus. *eLife* 5: e20515, 2016.

Schneider F, Baldauf K, Wetzel W, Reymann KG. Behavioral and EEG changes in male 5xFAD mice. *Physiol Behav* 135: 25–33, 2014.

Schoffelen J-M, Oostenveld R, Fries P. Neuronal Coherence as a Mechanism of Effective Corticospinal Interaction. *Science* 308: 111–113, 2005.

Schomburg EW, Fernández-Ruiz A, Mizuseki K, Berényi A, Anastassiou CA, Koch C, Buzsáki G. Theta Phase Segregation of Input-Specific Gamma Patterns in Entorhinal-Hippocampal Networks. *Neuron* 84: 470–485, 2014.

Scott L, Feng J, Kiss T, Needle E, Atchison K, Kawabe TT, Milici AJ, Hajós-Korcsok É, Riddell D, Hajós M. Age-dependent disruption in hippocampal theta oscillation in amyloid- β overproducing transgenic mice. *Neurobiol Aging* 33: 1481.e13–1481.e23, 2012.

Scoville WB, Milner B. Loss of recent memory after bilateral hippocampal lesions. *J Neurol Neurosurg Psychiatry* 20: 11–21, 1957.

Sejdić E, Djurović I, Jiang J. Time-frequency feature representation using energy concentration: An overview of recent advances. *Digit Signal Process* 19: 153–183, 2009.

Shadlen MN, Movshon JA. Synchrony Unbound: A Critical Evaluation of the Temporal Binding Hypothesis. *Neuron* 24: 67–77, 1999.

Shen J, Barnes CA, McNaughton BL, Skaggs WE, Weaver KL. The Effect of Aging on Experience-Dependent Plasticity of Hippocampal Place Cells. *J Neurosci* 17: 6769–6782, 1997.

Sheremet A, Burke SN, Maurer AP. Movement Enhances the Nonlinearity of Hippocampal Theta. *J Neurosci* 36: 4218–4230, 2016.

Singer W. Synchronization of Cortical Activity and Its Putative Role in Information Processing and Learning. *Annu Rev Physiol* 55: 349–374, 1993.

Skaggs WE, McNaughton BL, Wilson MA, Barnes CA. Theta phase precession in hippocampal neuronal populations and the compression of temporal sequences. *Hippocampus* 6: 149–172, 1996.

Soltesz I, Deschenes M. Low- and high-frequency membrane potential oscillations during theta activity in CA1 and CA3 pyramidal neurons of the rat hippocampus under ketamine-xylazine anesthesia. *J Neurophysiol* 70: 97–116, 1993.

Sóskuthy M. Generalised additive mixed models for dynamic analysis in linguistics: a practical introduction. arXiv:1703.05339v1 [stat.AP], 2017.
<http://arxiv.org/abs/1703.05339>

Squire LR, Stark CEL, Clark RE. The Medial Temporal Lobe. *Annu Rev Neurosci* 27: 279–306, 2004.

Srivastava A, Wu W, Kurtek S, Klassen E, Marron JS. Registration of Functional Data Using Fisher-Rao Metric. arXiv1103.3817v2 [math.ST], 2011.
<https://arxiv.org/abs/1103.3817>

Stankovski T, Ticcinelli V, McClintock PVE, Stefanovska A. Neural Cross-Frequency Coupling Functions. *Front Syst Neurosci* 11, 2017.

Stanton PK, Sejnowski TJ. Associative long-term depression in the hippocampus induced by hebbian covariance. *Nature* 339: 215–218, 1989.

Staubli U, Lynch G. Stable hippocampal long-term potentiation elicited by ‘theta’ pattern stimulation. *Brain Res* 435: 227–234, 1987.

Steinmetz NA, Koch C, Harris KD, Carandini M. Challenges and opportunities for large-scale electrophysiology with Neuropixels probes. *Curr Opin Neurobiol* 50: 92–100, 2018.

Sterniczuk R, Antle MC, LaFerla FM, Dyck RH. Characterization of the 3xTg-AD mouse model of Alzheimer’s disease: Part 2. Behavioral and cognitive changes. *Brain Res* 1348: 149–155, 2010.

Takahashi M, Nishida H, David Redish A, Lauwereyns J. Theta phase shift in spike timing and modulation of gamma oscillation: a dynamic code for spatial alternation during fixation in rat hippocampal area CA1. *J Neurophysiol* 111: 1601–1614, 2014.

Tallon-Baudry C, Bertrand O, Delpuech C, Pernier J. Oscillatory γ -Band (30–70 Hz) Activity Induced by a Visual Search Task in Humans. *J Neurosci* 17: 722–734, 1997.

Torrence C, Compo GP. A Practical Guide to Wavelet Analysis. *Bull Am Meteorol Soc* 79: 61–78, 1998.

Tort ABL, Komorowski R, Eichenbaum H, Kopell N. Measuring Phase-Amplitude Coupling Between Neuronal Oscillations of Different Frequencies. *J Neurophysiol* 104: 1195–1210, 2010.

Tort ABL, Komorowski RW, Manns JR, Kopell NJ, Eichenbaum H. Theta-gamma coupling increases during the learning of item-context associations. *Proc Natl Acad Sci* 106: 20942–20947, 2009.

Traub RD, Spruston N, Soltesz I, Konnerth A, Whittington MA, Jefferys JGR. Gamma-frequency oscillations: a neuronal population phenomenon, regulated by synaptic and intrinsic cellular processes, and inducing synaptic plasticity. *Prog Neurobiol* 55: 563–575, 1998.

- Trimper JB, Stefanescu RA, Manns JR.** Recognition memory and theta–gamma interactions in the hippocampus. *Hippocampus* 24: 341–353, 2014.
- Truccolo W.** From point process observations to collective neural dynamics: Nonlinear Hawkes process GLMs, low-dimensional dynamics and coarse graining. *J Physiol-Paris* 110: 336–347, 2016.
- Truccolo W, Eden UT, Fellows MR, Donoghue JP, Brown EN.** A Point Process Framework for Relating Neural Spiking Activity to Spiking History, Neural Ensemble, and Extrinsic Covariate Effects. *J Neurophysiol* 93: 1074–1089, 2005.
- Tsodyks MV, Skaggs WE, Sejnowski TJ, McNaughton BL.** Population dynamics and theta rhythm phase precession of hippocampal place cell firing: A spiking neuron model. *Hippocampus* 6: 271–280, 1996.
- Tsubokawa H, Ross WN.** IPSPs modulate spike backpropagation and associated $[Ca^{2+}]_i$ changes in the dendrites of hippocampal CA1 pyramidal neurons. *J Neurophysiol* 76: 2896–2906, 1996.
- Tucker JD, Wu W, Srivastava A.** Generative models for functional data using phase and amplitude separation. *Comput Stat Data Anal* 61: 50–66, 2013.
- Tweedie MCK.** An index which distinguishes between some important exponential families. *Statistics: Applications and new directions: Proc. Indian statistical institute golden Jubilee International conference.* p. 604, 1984.
- Vanderwolf CH.** Hippocampal electrical activity and voluntary movement in the rat. *Electroencephalogr Clin Neurophysiol* 26: 407–418, 1969.
- Varela F, Lachaux J-P, Rodriguez E, Martinerie J.** The brainweb: Phase synchronization and large-scale integration. *Nat Rev Neurosci* 2: 229–239, 2001.
- Vertes RP, Hoover WB, Di Prisco GV.** Theta Rhythm of the Hippocampus: Subcortical Control and Functional Significance. *Behav Cogn Neurosci Rev* 3: 173–200, 2004.
- Vertes RP, Kocsis B.** Brainstem-diencephalo-septohippocampal systems controlling the theta rhythm of the hippocampus. *Neuroscience* 81: 893–926, 1997.
- Villette V, Poindessous-Jazat F, Simon A, Léna C, Roullot E, Bellessort B, Epelbaum J, Dutar P, Stéphan A.** Decreased Rhythmic GABAergic Septal Activity and Memory-Associated θ Oscillations after Hippocampal Amyloid-β Pathology in the Rat. *J Neurosci* 30: 10991–11003, 2010.

Vinogradova O s. Hippocampus as comparator: Role of the two input and two output systems of the hippocampus in selection and registration of information. *Hippocampus* 11: 578–598, 2001.

Voigts J, Siegle JH, Pritchett DL, Moore CI. The flexDrive: an ultra-light implant for optical control and highly parallel chronic recording of neuronal ensembles in freely moving mice. *Front Syst Neurosci* 7: 8, 2013.

Von Der Malsburg C. Nervous Structures with Dynamical Links. *Berichte Bunsenges Für Phys Chem* 89: 703–710, 1985.

Wacker M, Witte H. Time-frequency Techniques in Biomedical Signal Analysis: A Tutorial Review of Similarities and Differences. *Methods Inf Med* 52: 279–296, 2013.

Watson GS. Smooth Regression Analysis. *Sankhyā Indian J Stat Ser* 26: 359–372, 1964.

Weber AI, Pillow JW. Capturing the Dynamical Repertoire of Single Neurons with Generalized Linear Models. *Neural Comput* 29: 3260–3289, 2017.

Whittington MA, Cunningham MO, LeBeau FEN, Racca C, Traub RD. Multiple origins of the cortical gamma rhythm. *Dev Neurobiol* 71: 92–106, 2011.

van Wijk BCM, Jha A, Penny W, Litvak V. Parametric estimation of cross-frequency coupling. *J Neurosci Methods* 243: 94–102, 2015.

Wikenheiser AM, Redish AD. Hippocampal theta sequences reflect current goals. *Nat Neurosci* 18: 289–294, 2015.

Winson J. Interspecies differences in the occurrence of theta. *Behav Biol* 7: 479–487, 1972.

Winson J. Loss of hippocampal theta rhythm results in spatial memory deficit in the rat. *Science* 201: 160–163, 1978.

Winter B, Wieling M. How to analyze linguistic change using mixed models, Growth Curve Analysis and Generalized Additive Modeling. *J Lang Evol* 1: 7–18, 2016.

Wood S. Generalized Additive Models: An Introduction with R. CRC Press, 2006.

Wood SN. Stable and Efficient Multiple Smoothing Parameter Estimation for Generalized Additive Models. *J Am Stat Assoc* 99: 673–686, 2004.

Wood SN. Fast stable restricted maximum likelihood and marginal likelihood estimation of semiparametric generalized linear models. *J R Stat Soc Ser B Stat Methodol* 73: 3–36, 2011.

Wood SN. Generalized Additive Models: An Introduction with R, Second Edition. CRC Press, 2017.

Wood SN, Goude Y, Shaw S. Generalized additive models for large data sets. *J R Stat Soc Ser C Appl Stat* 64: 139–155, 2015.

Wood SN, Li Z, Shaddick G, Augustin NH. Generalized Additive Models for Gigadata: Modeling the U.K. Black Smoke Network Daily Data. *J Am Stat Assoc* 112: 1199–1210, 2017.

Xacur OAQ, Garrido J. Generalised linear models for aggregate claims: to Tweedie or not? *Eur Actuar J* 5: 181–202, 2015.

Xu J, Yang H, Daubechies I. Recursive Diffeomorphism-Based Regression for Shape Functions. *SIAM J Math Anal* 50: 5–32, 2018.

Yamamoto J, Suh J, Takeuchi D, Tonegawa S. Successful Execution of Working Memory Linked to Synchronized High-Frequency Gamma Oscillations. *Cell* 157: 845–857, 2014.

Yee TW. Vector generalized linear and additive models: with an implementation in R. Springer, 2015.

Yu X, Yoganarasimha D, Knierim JJ. Backward Shift of Head Direction Tuning Curves of the Anterior Thalamus: Comparison with CA1 Place Fields. *Neuron* 52: 717–729, 2006.

Yunus RM, Hasan MM, Razak NA, Zubairi YZ, Dunn PK. Modelling daily rainfall with climatological predictors: Poisson-gamma generalized linear modelling approach. *Int J Climatol* 37: 1391–1399, 2017.

Zaremba JD, Diamantopoulou A, Danielson NB, Grosmark AD, Kaifosh PW, Bowler JC, Liao Z, Sparks FT, Gogos JA, Losonczy A. Impaired hippocampal place cell dynamics in a mouse model of the 22q11.2 deletion. *Nat Neurosci advance online publication*, 2017.

Zhao Rong, Fowler Stephanie W., Chiang Angie C.A., Ji Daoyun, Jankowsky Joanna L. Impairments in experience-dependent scaling and stability of hippocampal place fields limit spatial learning in a mouse model of Alzheimer's disease. *Hippocampus* 24: 963–978, 2014.

Zheng C, Bieri KW, Hsiao Y-T, Colgin LL. Spatial Sequence Coding Differs during Slow and Fast Gamma Rhythms in the Hippocampus. *Neuron* 89: 398–408, 2016a.

Zheng C, Bieri KW, Hwaun E, Colgin LL. Fast gamma rhythms in the hippocampus promote encoding of novel object-place pairings. *eNeuro* 3: 2016b.

Zheng C, Bieri KW, Trettel SG, Colgin LL. The relationship between gamma frequency and running speed differs for slow and fast gamma rhythms in freely behaving rats. *Hippocampus* 25: 924–938, 2015.